Study of structure and electrical transport property in composite and doped systems of $YBa_2Cu_3O_{7-\delta}$ superconductor

Thesis Submitted

For award of the degree

Doctor of Philosophy

In
Physics

By

Mousumibala Sahoo

Under the guidance of

Prof. D. Behera

Department of Physics and Astronomy
National Institute of Technology, Rourkela
Odisha (India)-769008
January-2015

Dedicated to

My

....Parents....

DECLARATION

I hereby declare that the work presented here is original and reproducible. The experimental work is performed by me under the supervision of Prof. D. Behera. The work content has not been submitted to any Institute / University for award of any degree. Any source material (theory, models, analysis, text etc.) used in my thesis work has been given due credit by citing it in reference section. I abide by the norms of ethical code of conduct of the Institute.

Date :

(Mousumibala Sahoo)

Signature of the Student

NATIONAL INSTITUE OF TECHNOLOGY
ROURKELA -769008, ODISHA, INDIA

Certificate

This is to certify that the thesis entitled, **"Study of structure and electrical transport property in composite and doped systems of $YBa_2Cu_3O_{7-\delta}$ superconductor"** being submitted by Mousumibala Sahoo to the Department of Physics and Astronomy, National Institute of Technology, Rourkela, is a record of bonafide research work carried out by her under my supervision and guidance for the partial fulfillment of award of the degree in Doctor of Philosophy. The contents embodied in this thesis have not been submitted to any other University or Institute for the award of any degree.

Date:

(Prof. D. Behera)
Associate Professor
Department of Physics & Astronomy
National Institute of Technology
Rourkela, Odisha, India-769 008

Supervisor

ACKNOWLEDGEMENT

..... The completion of the thesis work is an outcome of my efforts as a research scholar towards my Ph. D at the Low Temperature physics Laboratory of Department of Physics & Astronomy, National Institute of Technology, Rourkela. During this time, I have been supported by various people to whom I wish to express my gratitude.

First of all I would like to express my sincere gratitude to Prof. D. Behera (Dept. of Physics and Astronomy, NIT Rourkela) my esteemed Ph.D supervisor for being a constant source of inspiration and guidance.

I sincerely thank all my DSC members Prof. P.N Vishwakarma, Prof. B. Ganguly, Prof. S.K. Sahoo and Prof. D.K. Bisoyi for constructive suggestions to improve the quality of this research work and making my work place conducive for research. Thanks to all the faculty and staff of Department of Physics and Astronomy.

I would like to thanks Prof. T. Som of IOP, Bhubaneswar for providing the facility of PLD for sample preparation and the pelletron group of Inter University Accelerator Centre (IUAC), New Delhi for providing useful discussion and ion beam facility. I would like to extend my heartfelt thanks to Dr. S. Swain of BIT, Mesra for his help in Raman analysis.

I would like to express a deep sense of gratitude towards my fellow mates Arpna, Ranjit, Satya, Krutika, Beauty and all the research scholars of Dept. of Physics & Astronomy for their continuous encouragement, co-operation and creating a wonderful atmosphere to work with. Without their support it would have been impossible for me to work continuously.

I am especially grateful to my father (Mr. Madan Mohan Sahoo), mother (Mrs. Susila Sahoo) and brothers (Dr. S.S Sahu & Dr. H.B Sahoo) who stood by me through testing times and provided me great moral and emotional courage. It would have been almost impossible to pursue my research work without their encouragement and support.

My special loving thanks goes to my husband (Er. Rajesh Ku. Sahoo) who has always been the driving and inspiring force behind me. I am also thankful to my in-laws family for their constant support during my Ph. D programme.

I am extremely thankful to Department of Science and Technology, Govt. of India for providing me fellowship to carry out this research work and International travel support to present my research paper at International conference on superconductivity & Magnetism (ICSM-2014) which was held at Antalya, Turkey.

I extend profound appreciation and gratitude to Prof. S.K. Sarangi, Director, NIT Rourkela and all the faculty members of the Dept. of Physics & Astronomy, NIT Rourkela as well as Non-Teaching staffs for their kind cooperation during the progress of my research work and providing other relevant facilities available in the Institute.

Mousumibala Sahoo

Curriculum Vitae

Mousumibala Sahoo

Research Scholar

Department of Physics and Astronomy,

NIT, Rourkela, Odisha, India

Email: sahoomousumi0@gmail.com

Education	***Year of Passing***
10^{th}, B.B High School, Dhenkanal BSE, Odisha; 77.06 % 1^{st} class	2001
12^{th} (Science), Dhenkanal Mahila Jr. College, Dhenkanal CHSE; Odisha 60.00 % ; 1^{st} class	2003
Bachelor of Science (Physics Hons.), Utkal University, Odisha 1^{st} class Honors with Distinction (75.25 %)	2006
Master of Science (Physics), Ravenshaw University, Odisha 70.20 %; 1^{st} class	2008
Bachelor of Education (B.Ed), Utkal University, Odisha 63.66 %; 1^{st} class	2009
Pursuing Ph. D in Physics, NIT Rourkela, Odisha, India Under the Supervision of Prof. D. Behera, Dept. of Physics and Astronomy	2011-Present

List of Publications in International Journals

1. **M. Sahoo,** D. Behera, Structural and microstructural modification due to 100 KeV Ar^{+1} ion irradiation on YBCO/ BSO composite thin film, **J. Supercon. & Novel Magn.** 28 (2015) 371-377.

2. **M. Sahoo,** D. Giri, D. Behera, Study of structural modification and fluctuation induced electrical conductivity in $YBa_2Cu_3O_{7-y}$ + x $BaSnO_3$ superconductor composite, **J. Low Tem. Phys.** 177 (2014) 257-273.

3. **M. Sahoo**, D. Behera, Effect of Ti Doping on Structural and Superconducting Property of $YBa_2Cu_3O_{7-y}$ High T_c Superconductor, **J. Supercon. & Novel Magn.** 27 (2014) 83-93.

4. **M. Sahoo**, D. Behera, SCOPF analysis of $YBa_2Cu_3O_{7-\delta}$ + x Cr_2O_3 superconductor composite, **J. Phys. Chem. Solids** 74 (2013) 950-956.

5. **M. Sahoo**, D. Behera, Inhomogeneity induced conductivity fluctuation in $YBa_2Cu_3O_{7-\delta}$ / $BaTiO_3$-$CoFe_2O_4$ composite, **International Journal of Morden Physics B** vol. 27 (2013) 1350099(1-15).

6. A. Kujur, **M. Sahoo**, R. K Panda, K. Asokan and D. Behera, The effect of 200 MeV swift heavy Ag ions on the transport property of $YBa_2Cu_3O_{7-\delta}$ thick films, **Physica C** 492 (2013) 168-173.

7. **M. Sahoo**, D. Behera, DC electrical resistivity study of $YBa_2Cu_3O_{7-\delta}$ + x $BaTiO_3$-$CoFe_2O_4$ superconductor, **Physics. Express** 3, 22 (2013) 1-6.

8. **M. Sahoo,** D. Behera**,** Effect of submicron-sized Al_2O_3 inclusions on the superconducting order parameter fluctuation in $YBa_2Cu_3O_{7-\delta}$ superconductor, **Indian Journal of cryogenics** 38 (2013) 1- 4.

9. **M. Sahoo,** B. Bhol, A. Kujur, and D. Behera, Dimensionality fluctuation in the superconducting order parameter of $YBa_2Cu_3O_{7-\delta}$ + x $CoFe_2O_4$ composite, **AIP Conf. Proc.** 1461 (2012) 342-346.

10. **M. Sahoo**, D. Behera, "A comparative study of the structural modifications due to 100 keV Ar^{+1}, O^{+1}, Kr^{+1} ion irradiation on YBCO/ BSO composite thin film" (Communicated).

List of Publications in Conference / Workshop

1. **M. Sahoo**, D. Behera, Structural and microstructural modification due to 100 Kev Ar^{+1} ion irradiation on YBCO/BSO composite thin film: **Presented at 4th International conference on superconductivity and magnetism,** 2014 held at Antalya, Turkey.

2. **M. Sahoo**, D. Behera, Fluctuation induced electrical conductivity study in Ti doped $YBa_2Cu_3O_{7-\delta}$ high temperature superconductor: Presented at **condensed matter day,** 2013 held at NIT, Rourkela, India.

3. **M. Sahoo**, D. Behera, DC electrical resistivity study of YBCO+xBTO-CFO composite: Presented at **condensed matter day**, 2012 held at BIT, Mesra, Ranchi,India.

4. **M. Sahoo,** D. Behera**,** Dimensional fluctuations in $YBa_2Cu_3O_{7-\delta}$+ $xCoFe_2O_4$ superconductor: Presented at **2nd National seminar on Physics and Technology of Novel Materials**, 2012 held at school of physics, Sambalpur University, Jyotivihar, Burla, India.

5. **M. Sahoo,** R. Das, A. Kujur and D. Behera , Dimensional fluctuations in YBCO + x BZT Superconductor : Presented at **condensed matter day**, 2011 held at IIT Gwahati, India.

6. **M. Sahoo,** B. Bhol, A. Kujur and D. Behera, Dimensionality Fluctuation in the Superconducting Order Parameter of $YBa_2Cu_3O_{7-\delta}$+ $xCoFe_2O_4$ Composite : Presented at **International workshop on functional materials**, 2011 held at Nist, Berehmpur, India.

7. **M. Sahoo,** K. Sharma, A. Kujur, D. Behera, Effect of submicron-sized Al_2O_3 inclusions on the superconducting order parameter fluctuation in $YBa_2Cu_3O_{7-\delta}$ superconductor: Presented at **Asian conference on applied superconductivity and cryogenics**, 2011 held at IUAC New Delhi, India.

Workshop Attended

1. Participated in the **"Awareness workshop on the facilities of UGC-DAE consortium for scientific research"** jointly being organized by the UGC-DAE Consortium for Scientific Research, Indore and the Department of Physics, Utkal University, Bhubaneswar during March 23-24, 2012 at the Dept. of Physics, Utkal University, Bhubaneswar, India.

2. Participated in short term course on **"Characterization techniques for multifunctional materials"** held at NIT, Rourkela, India during 28-30th June, 2013.

3. Participated in one day workshop on **"Smart materials and thin films"** held at NIT, Rourkela on 28th August 2013.

ABSTRACT

A dramatic change in the research activity has taken place when high temperature superconductors (HTSCs) having T_c of 90 K, above the boiling point of liquid nitrogen (77 K), was established in $YBa_2Cu_3O_{7-\delta}$ (YBCO). We have selected the well-studied material, YBCO, as our parent material, for its relatively less anisotropic and less toxic nature with easily reproducible phase over other cuprates. HTSCs are widely used in various fields including medical diagnosis like Magnetic Resonance Imaging (MRI), Superconducting Quantum Interference Devices (SQUIDs), Transistors, Josephson Junction Devices, Circuitry connections, Particle accelerators, Sensors, Energy Storage etc.

The in-homogeneities such as mesoscopic in-homogeneities (grain boundaries, voids, and cracks), secondary phases and microscopic in-homogeneities such as oxygen deficiencies, chemical in-homogeneities, and local strains are induced in the HTSC systems during their preparation. Hence, HTSCs are defect ridden. Properties of HTSC are modified by doping and making composites of ferroelectric, dielectric and magnetic materials. Composites of YBCO with other materials started flourishing to enhance material property such as critical temperature T_c, critical current density J_c, transition width ΔT_c , normal state resistivity etc. Substitution at the Cu site is most important among all the cations of YBCO, as Cu-O networks play a major role for the occurrence of superconductivity in these materials. Ion irradiation can also improve the material's property by the addition of defects. The controlled defects produced by the collision cascade obtained by fast moving neutrons, point defects created by low energy ion impact and columnar defects generated by swift heavy ions result in significant enhancement of critical current density. Because of the huge energy loss, the ions in a medium can bring several changes in the target system such as annealing of defects, additional defects, resistivity enhancement, phase change. Ion irradiation can also modify the local geometrical arrangements through introduction of defects which induces resistivity changes in HTSC. Studies on ion beam irradiation of thin films of YBCO showed that T_c can be controllably reduced.

In the present thesis, an attempt has been made to understand the interplay between the in-homogeneities, secondary phases and the thermal fluctuations around the superconducting transition. As the excess conductivity region is affected much by the presence of in-

homogeneities, the main purpose of this study is to explore the physics of doped and composite cuprate superconductors near the superconducting transitions through the evaluation of Super Conducting Order Parameter Fluctuation (SCOPF). The present work aims at studying the various aspects i.e. structural modification, microstructural changes, electrical transport properties in a set of YBCO/BSO, YBCO/BTO-CFO, YBCO/Cr_2O_3 composites and YBCO/TiO_2 doped samples. Further, the work has been focused on the synergetic impact of dual defects i.e. BSO inclusions combined with low energy ion irradiation on structure and superconducting property of YBCO thin film.

The dielectric in-homogeneity $BaSnO_3$(BSO) has been investigated thoroughly as composite with YBCO in bulk as well as in thin film forms, studying all its properties and has achieved great recognition as artificial pining agent. This material raises our interest to be added with YBCO and combine its effects with point defects generated by low energy ion irradiation. Literature does not provide dual impact of defects created by ion irradiation and inclusion of BSO. Hence, our work includes a systematic study on the transport property of YBCO/BSO samples with varying BSO wt.% in bulk form. Further we have used 100 keV energy of Argon (Ar^{+1}), Oxygen (O^{+1}) and Krypton (Kr^{+1}) irradiated YBCO/1wt. % BSO composite thin films with different ion fluences for analyzing structural disorder, microstructure, resistivity and fluctuation conductivity.

Studies on excess conductivity of bulk granular samples of YBCO/x BSO show that BSO decreases the inter-layer coupling. It did not affect the oxygen content and grain size much but the transition temperatures T_c, T_{c0} reduces to a large extent. The Lawrence-Doniach temperature (T_{LD}) centered in the low temperature region for higher wt. % addition of BSO. The synergetic effects of 100 keV O^{+1}, Ar^{+1}, Kr^{+1} irradiation on YBCO/1wt.% BSO thin film shows the elongation of c axis as compared to the a and b lattice parameter. Broadening and shifting of the bridging oxygen mode in the RAMAN data indicates the oxygen deficit from the orthorhombic film that weakens electron-phonon coupling which yields poor superconducting properties. Morphological outlook shows the damaging of the film surface with agglomeration of BSO particles in Ar irradiation and amorphization occurs in the highest fluence for Kr irradiation. The destruction of the long range order of the Cu-O chains or the generation of oxygen vacancies in

the Cu-O square lattice planes due to ion implantation causes the destruction of superconductivity in the samples.

BTO-CFO and Cr_2O_3 are two important composite materials. Reported works focus only on the pinning aspect of these materials. No rigorous work has been done yet on the fluctuation conductivity of these materials as composite with YBCO. Here attempts have been taken to analyze the impact of magneto-electric material (BTO-CFO) and magnetic material (Cr_2O_3) on the structural property and electrical property of YBCO matrix. Addition of Cr_2O_3 and BTO-CFO improves the oxygen ordering in the samples without affecting the oxygen stoichiometry. Grain size is reduced much more with increase in porosity in the Cr_2O_3 added samples, where as the grain size remains intact due to BTO-CFO addition. Addition of BTO-CFO accounts for reduction of normal state resistivity and rise of weak-link resistivity with shifting of T_c towards lower temperature zones. But the addition of Cr_2O_3 enhances the normal state as well as residual resistivity and weak-link resistivity with exponential decrease of T_c towards lower temperature zones. The splitting of transition temperature marked by double peak in the derivative curve could be correlated with Cr_2O_3 residing in the grain boundary which forms weak links or Josephson junction that results in progressive decoupling of grains. Dimensionality of Cooper pair fluctuation shows a crossover from 2D to 3D region as the temperature is lowered in both the composites.

The transition element Ti is attractive for capacitor application in microelectronics due to its high dielectric constant. As the valence state of Ti^{4+} is higher than that of Cu^{2+} and they have similar electronic configurations and ionic sizes, it is of interest to investigate the effect of semiconducting and 3d transition element Ti substitution for Cu in YBCO. The fluctuation conductivity of Ti doped YBCO has not yet been studied rigorously. Here a detailed study on the structural modification and fluctuation conductivity near the SCOPF region for Titanium doping for the cu site of YBCO is presented. Low percentage doping of Ti decreases the normal state resistivity. Grain size is reduced with suppression of the critical region. The different crossover temperatures T_G, T_{LD}, $T_{2D\text{-}SW}$ and the width of transition between various cross over temperatures decrease with increase in doping percentage.

Contents

Declaration …….. **i**

Certificate…… **ii**

Acknowledgement…… **iii-iv**

Curriculum Vitae…… **v-viii**

Abstract…… **ix-xi**

Contents…… **xii-xvi**

List of Figures…….. **xvii-xx**

List of Tables …… **xxi-xxii**

Symbols and Abbreviations…….. **xxii-xxiii**

Chapter 1

INTRODUCTION , LITERATURE REVIEW & MOTIVATION

1. Introduction ……..... **1**

1.1. Basic phenomena…… **1-2**

1.2. Microscopic theory of superconductivity and foundation of BCS theory **3-5**

1.2.1 The London theory

1.2.2 Ginzburg-Landau Theory

1.2.3 BCS Theory

1.3. Types of superconductors.…….. **5**

1.4. Applications of superconductors……... **6**

1.5. High temperature superconductors…….. **6-10**

1.5.1 Spin-fluctuation mechanism in HTSC

1.5.2 Bipolaron concept of HTSC

1.5.3 Phase diagram of HTSC

1.6. Parent Material Chosen ……..…….. **10-14**

1.6.1 $YBa_2Cu_3O_{7-\delta}$ (YBCO) crystal structure

1.6.2 Intra- and Inter granular region in HTSC

1.6.3 Josephson effect and weak-link behavior

1.7. Role of defects and inhomogeneities in cuprates …… 14-18

1.7.1 Mesoscopic inhomogeneity
1.7.2 Microscopic inhomogeneity
1.7.3 Vortex pinning by defects
1.7.4 Irradiation Induced defects in cuprates

1.8. Literature review pertaining to composites……. 18-19

1.9. Literature review pertaining to doping...……. 20-21

1.10. Literature review pertaining to irradiation …….. 21-22

1.11. Literature review pertaining to fluctuation conductivity …… 22-23

1.12. Motivation …… 24

1.13. Objective and outlook of the thesis work …… 25-26

1.14. References …….. 26-31

Chapter 2

EXPERIMENTAL TECHNIQUES

2.1. Introduction…… 32

2.2. Methodology of sample preparation ...……. 32-35

2.2.1 Preparation of bulk $YBa_2Cu_3O_{7-\delta}$ (YBCO) powder
2.2.2 Preparation of $BaSnO_3$ powder
2.2.3 Preparation of $BaTiO_3$ (BTO) powder
2.2.4 Preparation of $CoFe_2O_4$ (CFO) powder
2.2.5 Preparation of $BaTiO_3$-$CoFe_2O_4$ (BTO-CFO) powder
2.2.6 Preparation of YBCO/BSO, YBCO/BTO-CFO, YBCO/Cr_2O_3 composite
2.2.7 Preparation of $YBa_2(Cu_{1-x}Ti_x)_3O_{7-\delta}$ samples
2.2.8 Preparation of YBCO/BSO composite PLD thin film

2.3. Irradiation by low energy ions …… 35-37

2.3.1 Beam Production Techniques

2.4. Characterization techniques of the samples…… 37-48

2.4.1 Micro-Raman Spectroscopy
2.4.2 Powder X-ray diffraction (XRD)
2.4.3 Scanning electron microscopy (SEM)
2.4.4 Field emission scanning electron microscopy (FESEM)
2.4.5 Fourier transform infrared spectroscopy (FTIR)

2.4.6 DC four probe resistivity measurement (R-T measurement)

2.4.7 P-E hysteresis loop measurement

2.5. References ……. 48-49

Chapter 3

SUPERCONDUCTING ORDER PARAMETER FLUCTUATION IN CUPRATES

3.1. General properties of granular superconductors …….. 50

3.2. Normal state and paracoherent resistivity ……. 51-54

3.3. Excess conductivity ……. 55-60

3.3.1 Gaussian Fluctuations

3.3.2 Critical Fluctuations

3.3.3 1D fluctuations

3.3.4 Shortwave fluctuations

3.4. References ……. 60-62

Chapter 4

STUDY OF STRUCTURE AND ELECTRICAL TRANSPORT PROPERTY IN $BaSnO_3$, Cr_2O_3 AND $BaTiO_3$-$CoFe_2O_4$ COMPOSITES OF $YBa_2Cu_3O_{7-\delta}$

4. Introduction ……. 63

***4.1. Part 1: Study of Structure and Electrical Transport property in YBCO/BSO Composite System* 64-77**

4.1.1. Synthesis and characterization tools …… 64

4.1.2. Result and Discussion……. 64-75

4.1.2.1 Phase formation of YBCO/ BSO composite system

4.1.2.2 RAMAN analysis

4.1.2.3 FTIR analysis

4.1.2.4 Microstructural analysis

4.1.2.5 Temperature dependence of resistivity

4.1.2.6 Excess conductivity

4.1.3. Conclusions……..... 76

4.1.4. References …….. 76-77

4.2. Part 2: Structure and Electrical Transport studies in YBCO/Cr_2O_3 Composite System **78-88**

4.2.1. Synthesis and characterization tools …….. 78

4.2.2. Result and Discussion …….. 78-87

4.2.2.1 Phase formation of YBCO/ Cr_2O_3 composite system

4.2.2.2 Raman analysis of YBCO/ Cr_2O_3 composite samples

4.2.2.3 Microstructural analysis of YBCO/ Cr_2O_3 composite samples

4.2.2.4 Temperature dependence of resistivity

4.2.2.5 Dimensionality fluctuations of excess conductivity

4.2.3. Conclusion ……..…….. 87-88

4.2.4. References …… 88

4.3. Part 3 : Study of Structure and Electrical Transport property in YBCO/BTO-CFO composite **89-98**

4.3.1. Synthesis and characterization tools …… 89

4.3.2. Result and Discussion ……. 89-97

4.3.2.1 Phase formation of YBCO/ BTO-CFO composite system

4.3.2.2 RAMAN analysis of YBCO/ BTO-CFO composite system.

4.3.2.3 P-E hysteresis loop of $BaTiO_3$-$CoFe_2O_4$ composite

4.3.2.4 Microstructural analysis

4.3.2.5 Temperature dependence of resistivity

4.3.2.6 Dimensionality fluctuations of excess conductivity

4.3.3. Conclusion …….. 98

4.3.4. References ……. 98

Chapter 5

STUDY OF STRUCTURE AND ELECTRICAL TRANSPORT PROPERTY IN Ti DOPED $YBa_2Cu_3O_{7-\delta}$ SYSTEM

5.1. Introduction…… 99

5.2. Role of Ti in $YBa_2Cu_3O_{7-\delta}$ superconductors ……. 99

5.3. Experimental details and interpretation of results …… 100-111

5.3.1 Synthesis and characterization of $YBa_2(Cu_{1-x}Ti_x)_3O_{7-y}$

5.3.2 Phase formation of $YBa_2(Cu_{1-x}Ti_x)_3O_{7-y}$ system

5.3.3 Raman spectroscopy of $YBa_2(Cu_{1-x}Ti_x)_3O_{7-y}$ system

5.3.4 Morphological outlook of $YBa_2(Cu_{1-x}Ti_x)_3O_{7-y}$ system

5.3.5 Temperature dependence of resistivity of $YBa_2(Cu_{1-x}Ti_x)_3O_{7-y}$

5.3.6 Dimensionality of fluctuations in $YBa_2(Cu_{1-x}Ti_x)_3O_{7-y}$ system

5.4. Conclusion …… 111

5.5. References …….. 111-112

Chapter 6

STUDY OF STRUCTURAL MODIFICATION AND ELECTRICAL TRANSPORT PROPERTY IN LOW ENERGY ION IRRADIATED YBCO/ BSO COMPOSITE THIN FILM

6.1. Introduction …… 113-114

6.2. Experimental details…… 114-115

6.3. Result and Discussion ……. 115-125

6.3.1 X- Ray Diffraction analysis

6.3.2 Raman analysis

6.3.3 FESEM analysis

6.3.4 Temperature dependent resistivity measurement

6.4. Conclusion ……. 125

6.5. References ……. 125-127

Chapter 7

CONCLUSIONS & FUTURE WORK

7.1. Conclusions ……. 128

7.2. Conclusions drawn from the work …….. 128

7.3. Important findings …… 128-130

7.4. Future work …….. 131

List of figures

Sl. no.	Figure Caption	Pg no.
Fig. 1.1.	(a) Zero-resistivity and (b) perfect diamagnetisms in superconductors	**2**
Fig. 1.2.	Schematic representation of the region within current density (J_c), magnetic field (H_c) and temperature (T_c) within which a material remains superconducting.	**2**
Fig. 1.3.	Variation of free energy (F) with order parameter (ψ) and variation of ψ with T_c.	**4**
Fig. 1.4.	Schematic representation of Cooper pair formation.	**4**
Fig. 1.5.	M-H plot and Magnetic field vs. temperature phase diagram of type II superconductor.	**5**
Fig.1.6.	Superconducting pairing and electronic anomalies induced by the spin collective mode in high T_c cuprates. The dots represent the electrons and the arrows represent their corresponding spin orientations.	**7**
Fig.1.7.	Schematic representation of the JT bipolaron.	**9**
Fig.1.8.	Phase diagram of cuprate superconductor. AF, Pseudogap, T_c, T* are defined in the main text.	**10**
Fig.1.9.	Unit cell of (a) $YBa_2Cu_3O_7$ and (b) $YBa_2Cu_3O_{7-\delta}$. The O (5) indicates oxygen sites which are partially filled and absent in orthorhombic structure.	**11**
Fig.1.10.	The effect of oxygen content on the T_c of $YBa_2Cu_3O_{7-x}$.	**12**
Fig. 1.11.	Schematic representation of arrangement of atoms inside the grain and grain boundary region in a polycrystalline material	**13**
Fig. 1.12.	Magnified view of intra-and inter-grain region.	**13**
Fig. 1.13.	Josephson junction array in polycrystalline HTSCs.	**14**
Fig. 1.14.	(a) Schematic representation of how magnetic field enters into superconductor in bundles (b) Trapping of magnetic field or pinning of vortices by defects.	**16**
Fig.1.15.	Basic ion-solid interaction process	**17**
Fig.1.16.	Resistive transition and regular resistivity behavior extrapolated from the normal behavior. Linear fitting of resistivity in the temperature range 150 to 250 K and extrapolated to 0 K gives resistivity slope ($d\rho/dT$) and residual resistivity (ρ_0) for cuprates.	**23**
Fig. 2.1.	The programmable furnace (Baisakh) for varying temperatures up to 1700^0 C in our laboratory.	**33**
Fig. 2.2.	Pulsed laser deposition set up at IOP, Bhubaneswar (Prof. T. Som's Lab): deposition chamber (left) and excimer laser (right).	**35**
Fig. 2.3.	Low energy ion irradiation set-up at IUAC, New Delhi.	**37**

Fig. 2.4.	(a) The schematic diagram of Raman experiment (b) Principle of Raman technique.	**39**
Fig. 2.5.	(a) Schematic view of an X-ray powder diffractometer (b) Reflection of X-rays from two planes of atoms in a solid.	**40**
Fig. 2.6.	(a) Schematic diagram of SEM setup (b) Electron beam interaction process with the sample.	**41**
Fig. 2.7.	Schematic diagram of EDXA principle.	**42**
Fig. 2.8.	Schematic optical diagram of an FTIR spectrometer	**44**
Fig. 2.9.	Schematic diagrams of four probe method.	**45**
Fig. 2.10	DC Four probe Resistivity measurement set up at our laboratory.	**47**
Fig. 2.11	Schematic diagram of a Sawyer Tower circuit for P-E loop measurement.	**48**
Fig. 3.1.	Schematic figure showing typical resistivity vs temperature curve for a granular superconductor (YBCO). $\rho_n(0)$ is the extrapolation to zero temperature of the normal-state resistivity ρ_n, ρ_p is the resistivity of the paracoherent state, ρ_{wl} is the average inter-grain resistivity ρ_{ab} is the intra-grain in-plane resistivity. The other two relevant parameters are the structural factor α_{str} accounting for porosity, micro cracks etc. and the anisotropy factor f arising from the anisotropy and misalignment of grains (α_{str}, f <1).	**53**
Fig. 3.2.	(a) Schematic plot of a Ginzburg-Landau free energy with a cubic term in the order parameter yielding a first-order transition. (b) Free energy with the cubic term at the point where the second minimum starts to appear (full line) and without the cubic term at the critical temperature (dashed line). The latter is displaced from its central position to help visualizing the similarity between the two curves in the region of positive order parameter.	**55**
Fig. 3.3.	log-log plot of excess conductivity $1/\rho - 1/\rho_R$ as a function of reduced temperature $\epsilon = (T-T_c)/T_c$.	**58**
Fig. 4.1.1	XRD Patterns of (a) YBCO+ x BSO Samples (x = 0.0, 0.1, 0.3, 0.5, 1.0, 2.5.0 wt. %) and (b) $BaSnO_3$.	**64,65**
Fig. 4.1.2	Lorentzian-fitting of (005) plane by varying BSO wt. %.	**66**
Fig. 4.1.3	Micro-Raman spectra of YBCO + x BSO samples (x = 0.0, 0.1, 0.3, 0.5, 1.0, 2.5 wt.%) samples.	**68**
Fig. 4.1.4	FTIR spectra of YBCO/BSO composite sample	**69**
Fig. 4.1.5	SEM micrographs of BSO and YBCO + x BSO (x= 0.0, 0.1, 0.3, 0.5, 1.0, 2.5 wt. %) samples marked as a, b, c, d, e, f respectively.	**70**
Fig. 4.1.6	Resistivity dependences on the temperature for YBCO+ x BSO (x = 0.0, 0.1, 0.3, 0.5, 1.0, 2.5, 5.0 wt. %) composites.	**71**
Fig. 4.1.7	Temperature derivative of resistivity and variation of transition temperatures for YBCO + x BSO composites (x = 0.0, 0.1, 0.3, 0.5, 1.0, 2.5 wt. %).	**72**
Fig. 4.1.8	Log-log plot of excess conductivity $1/\rho - 1/\rho_R$ as a function of reduced temperature $\epsilon = (T-T_c)/T_c$ in YBCO+ x BSO composites.	**74**

Fig. 4.1.9	Variation of cross over temperatures with BSO wt. %.	**75**
Fig. 4.2.1	XRD Patterns of YBCO+x Cr_2O_3 Samples (x = 0.0, 2.3, 4.4, 6.1 wt.%).	**78**
Fig. 4.2.2	Micro Raman spectra of YBCO+ x Cr_2O_3 samples (x = 0.0, 2.3, 4.4, 6.1 wt. %).	**80**
Fig. 4.2.3	SEM micrographs of YBCO + x Cr_2O_3 (x = 0.0, 2.3, 4.4, 6.1 wt. %) samples marked as a,b,c,d, respectively.	**81**
Fig. 4.2.4	Resistivity dependences on the temperature for YBCO + x Cr_2O_3 (x = 0.0, 2.3, 4.4, 6.1, 7.4 wt. %) composites.	**82**
Fig. 4.2.5	Temperature derivative of resistivity for YBCO +xCr_2O_3 composites (x = 0.0, 2.3, 4.4, 6.1 wt. %).	**83**
Fig. 4.2.6	Variation of transition temperatures with Cr_2O_3 wt. %.	**85**
Fig. 4.2.7	Log–Log plot of excess conductivity $1/\rho - 1/\rho_R$ as a function of reduced Temperature $\epsilon = (T-T_c)/T_c$ in YBCO+ x Cr_2O_3 composite.	**86**
Fig. 4.2.8	Variation of different cross over temperatures with Cr_2O_3 wt. %.	**87**
Fig.4.3.1(a)	XRD graphs of $BaTiO_3$ and $CoFe_2O_4$.	**89**
Fig.4.3.1(b)	XRD graph of $BaTiO_3$-$CoFe_2O_4$ composite.	**90**
Fig.4.3.1(c)	XRD graphs of (1-x) YBCO+ x $BaTiO_3$-$CoFe_2O_4$ (x= 0.0, 0.2, 0.4, 0.6) composites.	**90**
Fig. 4.3.2	Micro-Raman spectra of YBCO + x BTO-CFO Samples (x = 0.0, 0.2, 0.4, 0.6 wt. %) samples.	**92**
Fig. 4.3.3	P-E hysteresis loop of $BaTiO_3$-$CoFe_2O_4$ composite.	**93**
Fig. 4.3.4	SEM micrographs of (1-x)YBCO+x BTO-CFO (x=0.0,0.2,0.6 wt.%) samples marked as a,b,c respectively.	**93**
Fig. 4.3.5	Resistivity dependences on the temperature for YBCO+ x BTO-CFO(x= 0.0, 0.2, 0.4, 0.6 wt. %) composites.	**94**
Fig. 4.3.6	Temperature derivative of resistivity for (1-x) YBCO + x BTO-CFO composites (x = 0.0, 0.2, 0.4, 0.6 wt. %).	**95**
Fig. 4.3.7	Log-Log plot of excess conductivity $\Delta\sigma = 1/\rho - 1/\rho_R$ as a function of reduced Temperature $\epsilon = (T-T_c)/T_c$ in (1-x) YBCO+ x BTO-CFO composite.	**96**
Fig. 4.3.8	Variation of crossover temperatures with BTO-CFO wt. %.	**97**
Fig. 5.1	XRD Patterns of YBCO and $YBa_2(Cu_{1-x}Ti_x)_3O_{7-\delta}$ (x= 0.01,0.02,0.04,0.05) samples.	**100**
Fig. 5.2	Micro-Raman spectra of YBCO and $YBa_2(Cu_{1-x}Ti_x)_3O_{7-\delta}$ (x = 0.01,0.02,0.04,0.05) samples.	**102**
Fig. 5.3	SEM micrographs of YBCO and $YBa_2(Cu_{1-x}Ti_x)_3O_{7-\delta}$ (x = 0.01,0.02,0.04, 0.05) samples.	**104**

Fig. 5.4	EDX graphs of YBCO and 0.01% Ti doped samples marked as a and b respectively.	**105**
Fig. 5.5	Temperature dependent resistivity of YBCO and $YBa_2(Cu_{1-x}Ti_{-x})_3O_{7-\delta}$(x= 0.01, 0.02, 0.04, 0.05, 0.07) samples.	**106**
Fig. 5.6	Temperature derivative of resistivity of YBCO and $YBa_2(Cu_{1-x}Ti_x)_3O_{7-\delta}$ (x = 0.01, 0.02, 0.04, 0.05) samples.	**107**
Fig. 5.7	Variation of transition temperatures with various TiO_2 percentage.	**108**
Fig. 5.8	Log-Log plot of excess conductivity $1/\rho-1/\rho_R$ as a function of reduced Temperature $\epsilon = (T-T_c)/T_c$ in YBCO and $YBa_2(Cu_{1-x}Ti_x)_3O_{7-\delta}$ (x = 0.01,0.02,0.04,0.05) samples.	**109**
Fig. 5.9	Variation of different cross over temperatures with titanium percentage.	**110**
Fig. 6.1	XRD pattern of YBCO / BSO irradiated thin films with 100 keV (a) O^{+1} (b) Ar^{+1} (c) Kr^{+1} ions with varying dose.	**116**
Fig. 6.2	Micro-Raman spectra of unirradiated YBCO/BSO composite film and irradiated YBCO/BSO films with 100 keV of O^{+1} ions with varying dose.	**119**
Fig. 6.3	Micro-Raman spectra of unirradiated YBCO/BSO composite film and irradiated YBCO/BSO films with 100 keV of Ar^{+1} ions with varying dose.	**119**
Fig. 6.4	Micro-Raman spectra of unirradiated film and irradiated YBCO/BSO films with 100 keV of Kr^{+1} ions with varying dose.	**120**
Fig. 6.5	FESEM micrographs of $YBa_2Cu_3O_{7-\delta}$ / 1 wt. % BSO unirradiated thin film.	**121**
Fig. 6.6	FESEM micrographs of (a) O^{+1} irradiated sample with fluence $5x10^{15}$ ions/cm^2 (b) fluence of 5×10^{16} ions /cm^2.	**121**
Fig. 6.7	FESEM micrographs of Ar^{+1} irradiated samples with fluence (a) 5×10^{15} ions/cm^2 (b) $5x10^{16}$ ions/cm^2.	**122**
Fig. 6.8	FESEM micrographs of Kr^{+1} irradiated samples with fluence (a) $5x10^{15}$ ions/cm^2 (b) 10^{16} ions/cm^2 (c) $5x10^{16}$ ions/cm^2.	**122**
Fig 6.9	Resistivity dependences on the temperature for YBCO+ x $BaSnO_3$ (x = 0.0, 1.0 wt. %) samples.	**124**

List of Tables

Sl No.	Table Captions	Pg no.
Table 1	Transition temperatures of some high T_c superconducting compounds.	**7**
Table 2.1	Growth conditions for PLD film.	**35**
Table 2.2	Various types of low energy ion beams.	**36**
Table 4.1.1	Lattice parameters calculated from XRD graphs.	**66**
Table 4.1.2	Oxygen content calculated using XRD and Raman spectra. 'c' is the lattice parameter along Z direction, 7-y is oxygen content, ν is the frequency of apical oxygen.	**68**
Table 4.1.3	Variation of normal state and superconducting parameters in the composites with different BSO wt. %.	**73**
Table 4.1.4	Parameters extracted from Excess conductivity analysis in YBCO/BSO composites.	**75**
Table 4.2.1	Lattice parameters calculated from XRD graphs	**79**
Table 4.2.2	Oxygen content calculated using XRD and Raman spectra. 'c' is the lattice parameter along Z direction, y is oxygen loss, ν is the frequency of apical oxygen.	**81**
Table 4.2.3	Variation of normal state and superconducting parameters in the composites with different Cr_2O_3 wt. %.	**84**
Table 4.2.4	The parameters extracted from excess conductivity analysis in YBCO/Cr_2O_3 composite.	**86**
Table 4.3.1	Lattice parameter of YBCO with different BTO-CFO wt. %.	**91**
Table 4.3.2	Oxygen content calculated using XRD and Raman spectra. 'c' is lattice parameter along Z direction, δ is oxygen loss, ν is frequency of apical oxygen.	**92**
Table 4.3.3	Variation of normal state and superconducting parameters in the composites with different BTO-CFO wt. %.	**95**
Table 4.3.4	The parameters extracted from excess conductivity analysis in YBCO/ BTO-CFO composite.	**97**
Table 5.1	Lattice Parameters calculated from XRD graphs	**101**
Table 5.2	Oxygen content calculated using XRD and Raman spectra. 'c' is the lattice parameter along Z direction, y is oxygen loss, ν is the frequency of apical oxygen.	**103**
Table 5.3	Variation of normal state and superconducting parameters in the doped samples	**107**
Table 5.4	TiO_2 content dependence of different cross over temperatures (Ginzburg-Landau, Lawrence-Doniach and Shortwave fluctuation)	**110**

Table 6.1 Lattice parameters calculated from XRD graphs for O^{+1} irradiation **117**

Table 6.2 Lattice parameters calculated from XRD graphs for Ar^{+1} irradiation **117**

Table 6.3 Lattice parameters calculated from XRD graphs for Kr^{+1} irradiation **118**

Symbols and Abbreviations

YBCO	$YBa_2Cu_3O_{7-\delta}$
HTSC	High temperature superconductor
SCOPF	Superconducting order parameter fluctuation
SQUID	Superconducting quantum interference device
JT	Jahn-Teller
T_c	Transition temperature
T_{cmf}	Mean field transition temperature
T_{conset}	Onset of transition temperature
T_{c0}	Zero resistivity temperature
T*	Pseudogap temperature
J_c	Critical current density
ΔT_c	Transition width
ρ	Electrical resistivity
ρ_n	Normal state resistivity
ρ_{wl}	Weak-link resistivity
ρ_0	Residual resistivity
ρ_p	Paracoherent resistivity
α_n	Percolation factor
χ	Magnetic susceptibility
B	Magnetic induction
H	Applied filed
SC	Superconductor
E	Electric field
μ_0	Permeability
λ	London penetration depth
GL	Ginzburg-Landau theory
F	Free energy density

ψ	Order parameter
ϕ	Phase of the order parameter
n_s	Superfluid density
H_c	Critical field
H_{c1}	Lower critical field
H_{c2}	Upper critical field
y	Oxygen content
δ	Orthorhombic distortion
Φ_0	Magnetic flux
ξ	Coherence length
J	Inter-layer coupling
PG	Pseudogap
T*	Pseudogap temperature
ε	Reduced temperature
σ	Excess Conductivity
S_n	Nuclear energy loss
S_e	Electronic energy loss
g	Tunnelling conductance
T_{LD}	Lorentz-Doniac temperature
T_G	Ginzburg- Landau Temperature
T_{SW}	Short-Wave Fluctuation Temperature
AL	Aslamazov-Larkin
MT	Maki-Thompson
DOS	Density of states
SHI	Swift heavy ion
XRD	X-ray diffraction
SEM	Scanning electron microscopy
FESEM	Field emission scanning electron microscopy
EDXA	Energy dispersive x-ray analysis
PLD	Pulsed laser deposition
FTIR	Fourier transform infrared spectroscopy
FWHM	Full width half maxima
SRIM	Stopping and ranging of ions in matter

Chapter 1

Introduction, Literature Review & Motivation

1. INTRODUCTION

This chapter introduces the phenomenon of superconductivity with the explanation of some related elementary theories. The practical applications and physical properties of high temperature superconducting materials (HTSC) are described with a clear explanation on phase diagram, intra and inter grain regions of the cuprates. The crystallographic structure of HTSC such as $YBa_2Cu_3O_{7-\delta}$ is examined with role of inhomogeneity and defects towards the weak link behaviour, pinning centres, psudogap, fluctuation conductivity and superconducting order parameter fluctuation (SCOPF). Another important aspect i.e. irradiation and its impact on superconducting materials has been discussed. The chapter ends with a brief motivation followed with objectives of the work carried out in this thesis.

1.1 BASIC PHENOMENA

Generally the electrical resistance of a metal is proportional to temperature. In 1908 Dutch physicist Heike Kammerlingh Onnes of Leiden University successfully liquefied helium. He was able to measure the electrical resistance of metals at very low temperatures. The exciting discovery he made in 1911 was that as the temperature of Hg decreased, its resistance did not fall continuously, but dropped suddenly to zero at around 4.2 K [1]. This phenomenon was termed as superconductivity. This was found to occur for other elements such as Pb, Sn and Al at critical temperatures between 4 -10 K. Onnes was awarded the Nobel Prize in 1913 for liquification of Helium, but not specially for superconductivity. The complete expulsion of magnetic field by the superconducting sample below transition temperature (T_c) is called the "Meissner effect" i.e. perfect diamagnetism (fig 1.1). This property of superconductors was discovered in 1933 by Meissner & Ochsenfeld [2]. Perfect diamagnetism signifies that superconductivity is a true thermodynamic state and moving from the normal to the superconducting state, a material undergoes a thermodynamic phase transition. In order to achieve this, the overall free energy must be lower in the superconducting state than in the normal state. This temperature dependent energy difference is known as the "condensation energy". When an external magnetic field is applied to a material in the superconducting state, energy requires for preventing it from penetrating. If that is larger than the condensation energy, the material will lower its overall free energy by returning to its normal state. Thus, there exists a critical magnetic flux density B_c, which is a function of temperature as represented by the equation:

$$f_n(T) - f_s(T) = \frac{B_c^2(T)}{2\mu_0} \qquad (eq^n\ 1.1)$$

where f_n and f_s are the Helmholtz free energies of the normal and superconducting states respectively and μ_0 is the permeability of free space.

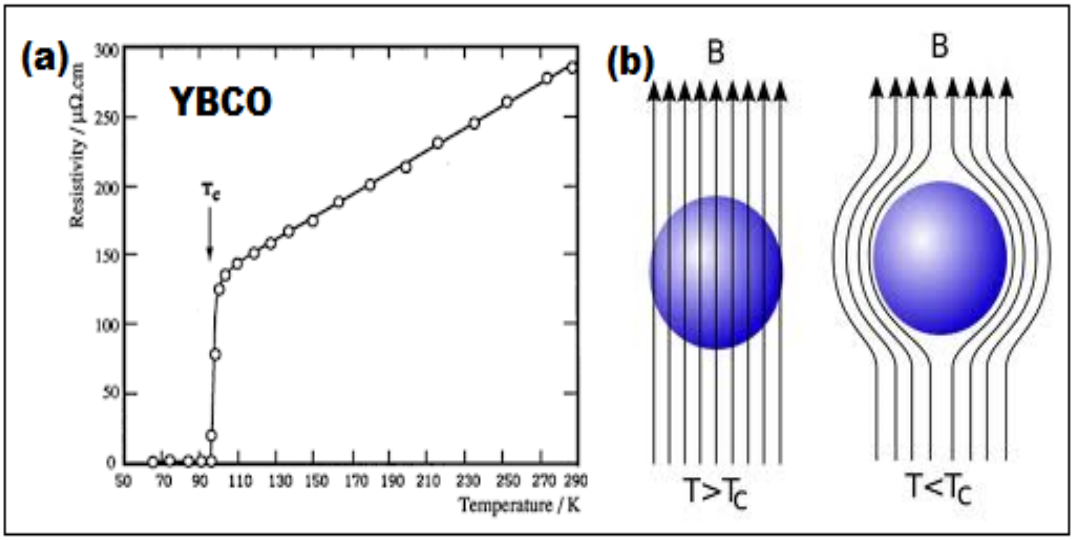

Fig. 1.1 (a) Zero-resistivity and (b) perfect diamagnetisms in superconductors [3].

In addition to the requirement that the temperature and magnetic field must be below the critical value, there is also a limit on the current density in a superconducting material. Hence, the three critical values T_c, H_c and J_c which are all interdependent are shown in figure 1.2 and a material will only remain in the superconducting state within the volume shaded.

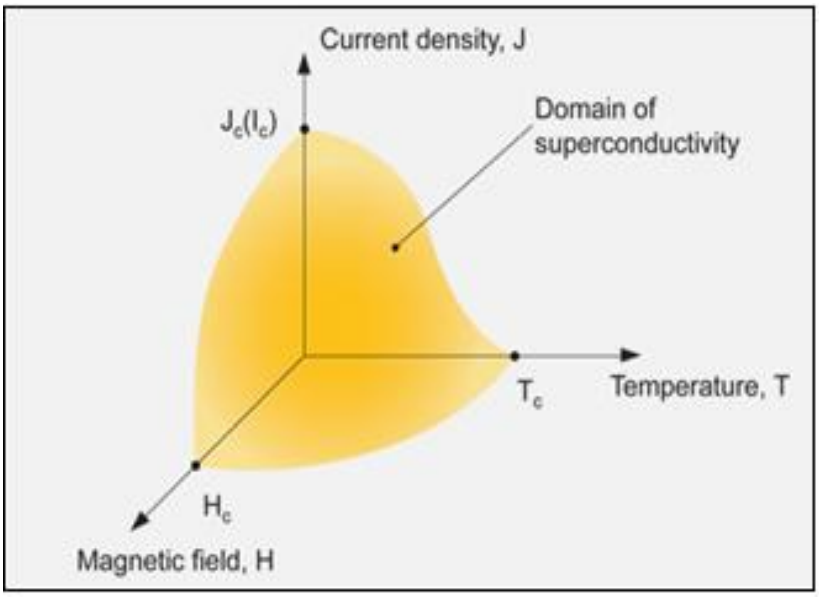

Fig. 1.2 Schematic representation of the region bounded within current density (J_c), magnetic field (H_c) and temperature (T_c) within which a material remains superconducting [4].

1.2 MICROSCOPIC THEORY OF SUPERCONDUCTIVITY & FOUNDATION OF BCS THEORY

Superconductivity was found in materials before the physics community predicted the phenomena. Theories were formed to explain, match and predict the characteristics of these materials that undergo the phase transition.

1.2.1 London's Theory

In order to explain the expulsion of magnetic field from the superconductor, the London brothers proposed a phenomenological theory in 1935 [5] taking into account the previously proposed two fluid model. All the free electrons in a superconductor are divided into two groups i.e. superconducting electrons of density n_s and normal electrons of density n_n, with the total density of free electrons $n = n_s + n_n$. As the temperature increases from 0 to T_c, the density n_s decrease from n to 0. Further, assumptions are that the magnetic flux penetrates to a certain penetration depth λ that is independent on the strength of the magnetic field as well as the dimensions of the sample.

$$\nabla^2 B = B/\lambda_L \qquad (eq^n\ 1.2)$$

where, λ_L is the London penetration depth

But their results consistently overestimated the experimentally found values, and so their assumptions were discarded.

1.2.2 Ginzburg-Landau Theory

First phenomenological theory taking into account the quantum effects was proposed by Ginzburg and Landau in 1950 [6]. It is based on the idea that the superconducting transition is a second order phase transition. The order parameter is described by complex number $\psi = |\psi| e^{i\theta}$. The amplitude $|\psi|$ is zero in the normal phase above the superconducting transition T_c and is finite in the superconducting phase below T_c. In the presence of an external magnetic field the order parameter has a spatial variation. When the spatial variation of the order parameter is taken into account, the free energy of the system can be expressed in terms of the order parameter ψ and its spatial derivative. This is valid in the vicinity of T_c. Below T_c the amplitude $|\psi|$ is small and the length scale for spatial variation is long (Fig.1.3). The order parameter ψ is considered as a wave function for a particle of charge q* and mass m*.

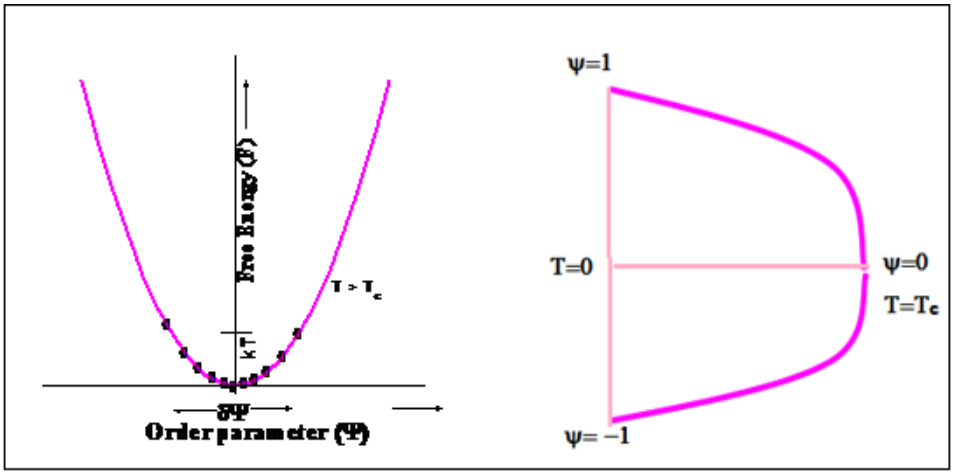

Fig. 1.3 Variation of free energy (F) with order parameter (ψ) and variation of ψ with T_c.

1.2.3 BCS Theory

In 1957 Bardeen, Cooper and Schrieffer (BCS) proposed a theory that explains the microscopic origin of superconductivity. The BCS theory based on the assumption that superconductivity arises when the attractive Cooper pair interaction dominates over the repulsive Coulomb force [7]. A Cooper pair is a weak electron-electron bound pair mediated by a phonon interaction (Fig. 1.4). A paired electron is one with opposite momentum and spin that is attracted to this force. This heuristic explanation is somewhat incomplete, because the phonon-mediated interaction is a long range attraction and hence requires quantum mechanics for a full explanation. Cooper's monumental work in 1956 showed that due to the Fermi statistics of the electron, this paired e^- - e^- state can have energy less than that of the Fermi-energy of the material [8]. Thus at adequately low temperatures, when thermal energy is not a factor, bound e^-- e^- states can form.

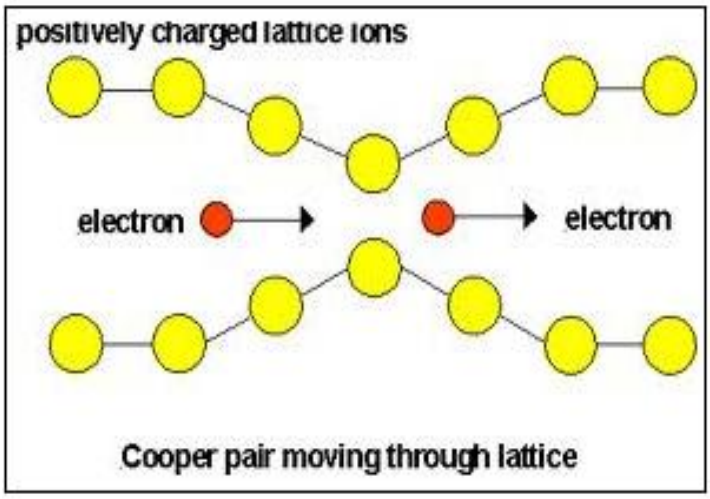

Fig. 1.4 Schematic representation of Cooper pair formation [9].

The two approaches, the BCS theory and the GL theory were remained completely separate until Gorkov [10] showed that, in some limiting cases, the order parameter ψ(r) of the GL theory is proportional to the pair potential Δ(r). At the same time this also shows that q* = 2e and m* = 2m. The parameter $|\psi(r)|^2$ represents the local density of superconducting electrons $n_s(r)$. The macroscopic behaviour of superconductors can be explained well by GL theory. This theory also provides the qualitative framework for understanding the dramatic super-current behaviour as a consequence of quantum properties on a macroscopic scale. Their results were able to accurately match the experimental results of the time and were later shown to be a specific form of the BCS theory. GL theory has been discussed more in chapter III.

1.3 TYPES OF SUPERCONDUCTORS

Based on diamagnetic response, superconductors can be classified into two types.

(a) Type I Superconductor

(b) Type II Superconductor

In type-I superconductors, superconductivity is abruptly destroyed via a first order phase transition, when the strength of the applied field rises above a critical value H_c. This type of superconductivity is normally exhibited by pure metals i.e. aluminium, lead, mercury etc.

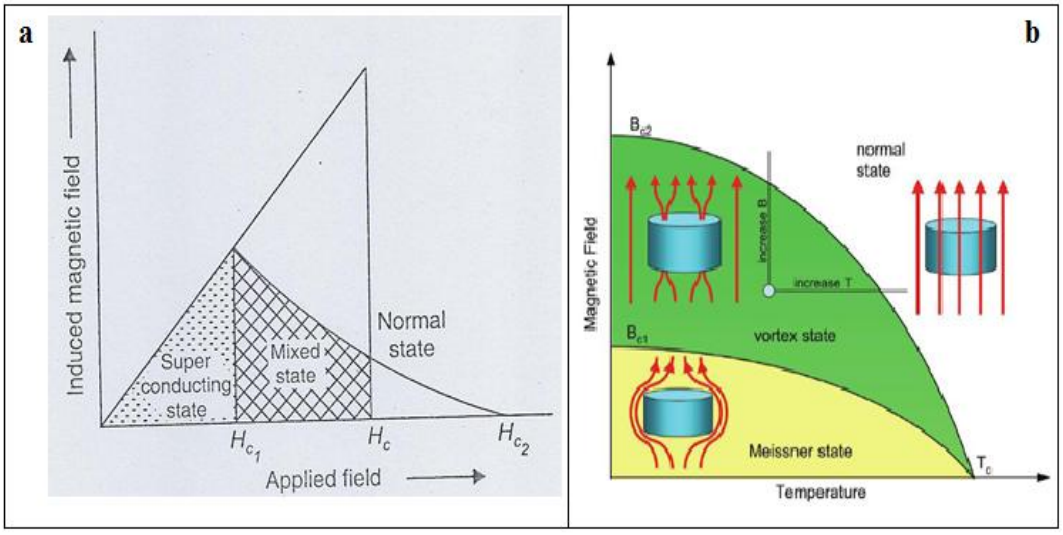

Fig. 1.5 M-H plot and Magnetic field vs. temperature phase diagram of type II superconductor [11].

Type I superconductors does not possess more practical applications due to lower values of H_c and T_c. Type-II superconductor is characterized by the formation of magnetic vortices in an applied magnetic field. This occurs above certain critical field strength H_{c1}. The vortex

density increases with increasing field strength. At a higher critical field H_{c2}, superconductivity is completely destroyed (Fig. 1.5).

1.4 APPLICATIONS OF SUPERCONDUCTORS

The last two decades brought substantial progress in physics of superconductivity due to the discovery and numerous subsequent investigations of high temperature superconductors. Such new materials have opened up promising possibilities of various applications in advanced technologies. Some of them are listed below:

- Medical: Magnetic resonance imaging, biotechnical engineering
- Electronics: SQUIDs, Transistors, Josephson junction devices, circuitry connections, particle accelerators, sensors
- Industrial: Separation, Magnets, Sensors and transducers , Magnetic shielding
- Power Generation: Motors, Generators, Energy Storage, Transmission, Fusion, Transformers and Inductors
- Magnetically levitated vehicles, Marine propulsion

The principle of levitating magnet is being researched in Japan and other countries. The flywheel containing magnet is placed above a superconductor. By spinning the flywheel, electricity can be stored in the form of rotational energy. Now coil is wrapped around the wheel and electricity passed through the coil. By motor principle wheel will start to revolve. If this is done in vacuum it will rotate without loss in power. This arrangement can be utilized for generation of electricity. In case of transmission of power as in case of copper wires, 50 kilowatts are lost to resistance for each kilometre. But with superconductive materials, the loss is thought to be reducible to 35 kilowatts. Hence large amount of power can be saved if superconductors are being used for transmission and reception. Considering the environmental condition the HTSC devices are ahead of conventional devices [12, 13].

1.5 HIGH TEMPERATURE SUPERCONDUCTORS (HTSC)

The understanding of the superconductivity turned upside down when in 1986, J. G. Bednorz and K.A. Muller discovered layered copper oxide superconductor [14, 15]. The pioneering material was $La_{2-x}Ba_xCuO_4$ (LBCO). Tuning the doping at Ba site the material could go from an insulator to a superconductor. The discovery of superconductivity in cuprates was the start

of an avalanche of new superconductors. Decades of work in traditional superconductors had pushed T_c above 20 K. In less than one year after the discovery of superconductivity in cuprates, the effort of hundreds of labs around the world pushed the transition temperature above the boiling point of liquid Nitrogen (77 K) with the discovery of $YBa_2Cu_3O_{7-x}$ (YBCO) [16], the first superconductor with T_c > 77K, and going up to 130K in mercury-based compounds under pressure. A dramatic change in research activity has been started with YBCO discovery (Table 1). The granular nature of the system and the peculiar behaviour of the material even at ambient temperature became a haunting ground for researchers.

Table1. Transition temperatures of some high T_c superconducting compounds

Material	**T_c(K)**
$YBa_2Cu_3O_{7-\delta}$	92
$Bi_2Sr_2CaCu_2O_8$	85
$Bi_2Sr_2Ca_2Cu_3O_{10}$	110
$TlBa_2Ca_2Cu_3O_9$	123
$HgBa_2Ca_2Cu_3O_8$	135

1.5.1 Spin-fluctuation mechanism in HTSC

After 25 years of intense research, the mechanism of superconductivity in cuprates is still illusive. The spin-fluctuation mechanism of high-temperature superconductivity in copper-oxide compounds which is determined by the high intensity of the anti-ferromagnetic exchange interaction is attracting considerable attention of researchers at present [17, 18].

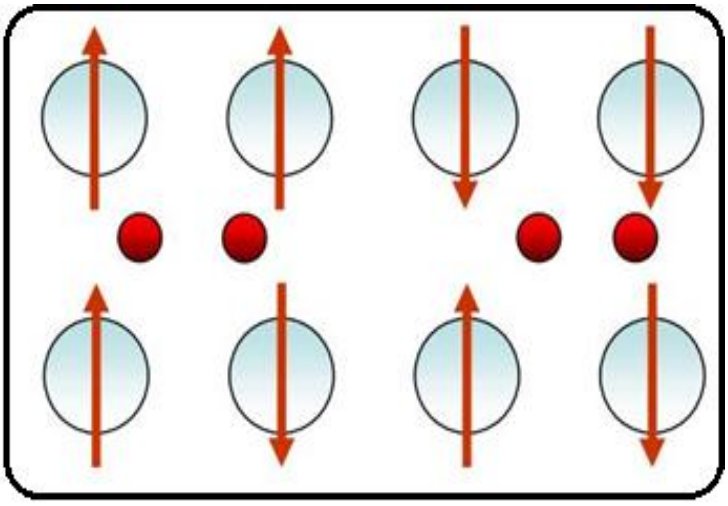

Fig. 1.6 Superconducting pairing and electronic anomalies induced by the spin collective mode in high T_c cuprates [19]. The dots represent the electrons and the arrows represent their corresponding spin orientations.

Anderson was the first to point out a special role of strong electronic correlations in cuprates and the anti-ferromagnetic exchange interaction associated with these correlations (Fig. 1.6). He also proposed the exchange pairing mechanism in the framework of the t-J model [20]. In a high T_c superconductor, the mechanism is extremely similar to a conventional superconductor. In this case, phonons virtually play no role and their role is replaced by spin-density waves. As all conventional superconductors are strong phonon systems, all high-T_c superconductors are strong spin-density wave systems. When an electron moves in a high-T_c superconductor, its spin creates a spin-density wave around it. This spin-density wave in turn causes a nearby electron to fall into the spin depression created by the first electron (called water-bed effect) a Cooper pair is formed. When the system temperature is lowered, more spin density waves and Cooper pairs are created, leading to superconductivity. As these systems are magnetic in nature, due to the Coulomb interaction, there is a strong Coulomb repulsion between electrons. This Coulomb repulsion prevents pairing of the Cooper pairs on the same lattice site. The pairing of the electrons occurs at near-neighbor lattice sites. This is the so called d-wave pairing, where the pairing state has a node (zero) at the origin [21, 22].

1.5.2 Bipolaron concept of HTSC

Several theories and models have been proposed to explain the mechanism of HTSC, but no concrete proposal has been successful. The bipolaron concept is one of the recent proposals by Professor K.A. Muller who had discovered the HTSC in cuprates. The concept of polaron led to the discovery of the copper oxide superconductors. The concept was that if "an electron and a surrounding lattice distortion with a high effective mass can travel through the lattice as a whole, and a strong electron-phonon coupling exists, the perovskite insulator could be turned into a high temperature superconductor" [23]. Bipolarons had been proposed earlier by a number of theoreticians but only the intersite Jahn-Teller (JT) bipolaron (Fig. 1.7) is the true elementary quasi-particle occurring in the copper oxides. Kochelaev, Mihailovic and Kabanov used a three-spin model for an analytical description of this JT bipolaron concept [24-26]. This model consists of two Cu^{+2} ions with each has spin S=1/2 anti-parallel to each other and to the rest of the lattice, plus a hole mainly located on the neighbour oxygen, also with spin S=1/2. Mihailovic and Kabanov add a second hole on oxygen orbitals with the anti-parallel spin to the first.

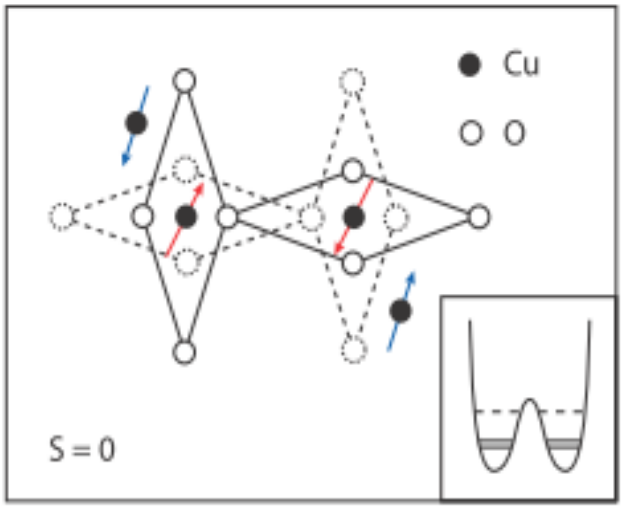

Fig. 1.7 Schematic representation of the JT bipolaron [24, 25].

Therefore, the total spin is S=0, thus overcoming the difficulty to move in the AFM lattice which a single polaron with spin. A large number of properties of the cuprates can be understood with this concept.

1.5.2 Phase diagram of HTSC

Pseudogap in HTSC occurs due to the formation of JT bipolarons below T^* (Pseudogap temperature) upon cooling. By further lowering the temperature the bipolarons become phase-coherent and T_c (Transition temperature) is reached. This explains why superconductivity does not arise in low doping concentration (Fig. 1.8). The transport properties of cuprates change drastically by the introduction of charge carriers to the Cu-O planes. This is done by chemical doping that varies for each family of cuprates. According to band theory, when undoped these materials are insulator. When the band is half filled, each Cu site presents one free electron and therefore it should be a metal. Conduction is suppressed due to the strong Coulomb on-site repulsion which prohibits two electrons to occupy the same site, leading to the so called Mott insulator state. In this state each electron is frozen in a lattice site because it cannot overcome the high energetic double occupancy state. The cuprates also present anti-ferromagnetism when undoped. The back and forth virtual hopping between neighbour sites leads to an overall reduction of the total energy of the state. This process is only possible if neighbour electrons have opposite spins, leading the material into an antiferromagnetic order. The superconductivity, as well as other interesting properties, will arise once we remove some of the electrons, allowing electrons to hop and therefore destroying the anti-ferromagnetic (AF) insulator state. Superconductivity happens within a limited range of doping.

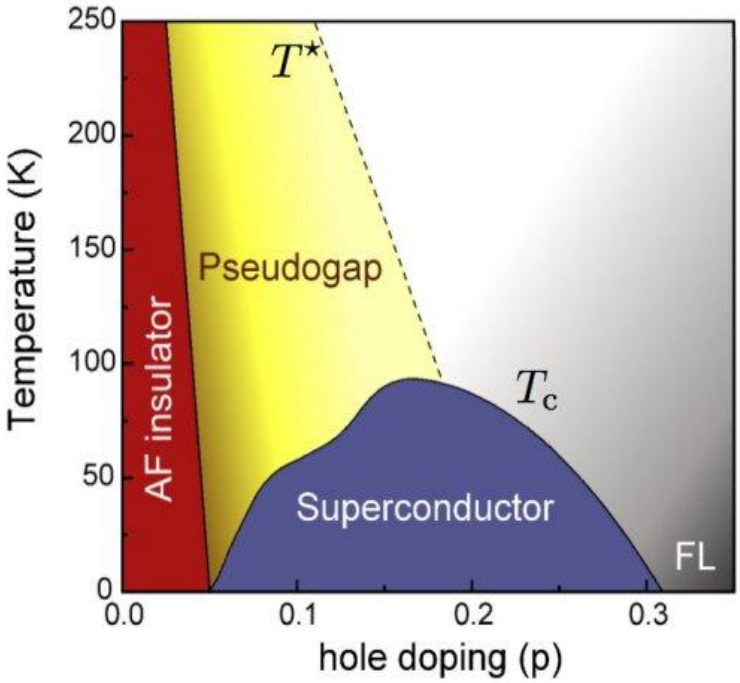

Fig. 1.8 Phase diagram of cuprate superconductor. AF, Pseudogap, T_c, T* are defined in the main text [27].

Not many of the cuprates allow accessing all doping levels but the dome shaped doping dependence of T_c is universal across all families of superconducting copper oxides. When superconducting transition temperature T_c is maximum, we define this doping as optimal doping. Samples with doping lower than the optimal doping are referred as under doped and samples with higher doping than optimal are referred as over-doped. At high doping the electronic states in the cuprates behave as a Fermi liquid (FL) but in the under-doped regime, between the superconducting dome and the AF phase, an unusual metallic state is present. The main signature of this state is the presence of a depression at the density of states near the Fermi energy which identifies it as the pseudogap phase [28].

1.6 PARENT MATERIAL CHOSEN

Among all the HTSCs the cuprate compounds namely yttrium, bismuth, thallium and mercury based compounds bear the advantage of being operated at less costly refrigeration scheme i.e. at the boiling point of readily available liquid nitrogen than the costly liquid helium. The $YBa_2Cu_3O_{7-\delta}$ compound is a well-studied material known for its relatively less toxic nature and easily reproducible phase over other compounds [29]. The limitations of this material are its hygroscopic nature and oxygen stoichiometric. The issues could be sorted out by preserving the samples in vacuum jar with silica gel kept inside and oxygen deficiencies were removed by oxygen annealing. The material synthesis for the pure phase in case of bismuth

layered compound is quite difficult. For instance, the highest T_c ~110 K recorded for $Bi_2Sr_2Ca_2Cu_3Ox$ phase includes intergrowth of the Bi_{2212} phase [30, 31]. However, for stable Bi phase, unfriendly toxic Pb was added, which limits the usage of Bi_{2223}. The highly volatile bismuth loss compensation was another drawback associated with Bi materials. Bi_{2212} phase could be easily prepared with some impurity phase without lead addition but with T_c~80 K i.e. lower than YBCO. The Thallium-based HTSCs i.e. $Tl_2Ba_2Ca_2Cu_3Ox$ (~125 K) and mercury based HTSC phase $HgBa_2Ca_{n-1}Cu_nO_{2n+2+x}$ phase (~135 K) existed in different phases like that of Bismuth materials. The major hindrances of these materials were their highly poisonous nature. Hence, handling of these compounds demands special care and great precaution. Considering the above mentioned factors of non-eco-friendly and health hazard issues of all the cuprates, we conclude YBCO to be a superior rare-earth layered superconductor to be our chosen parent material.

1.6.1 $YBa_2Cu_3O_{7-\delta}$ (YBCO) crystal structure

In 1987 at the University of Houston, Paul Chu with his students discovered the first ceramic material with a transition temperature greater than 77 K i.e YBCO or Y123.

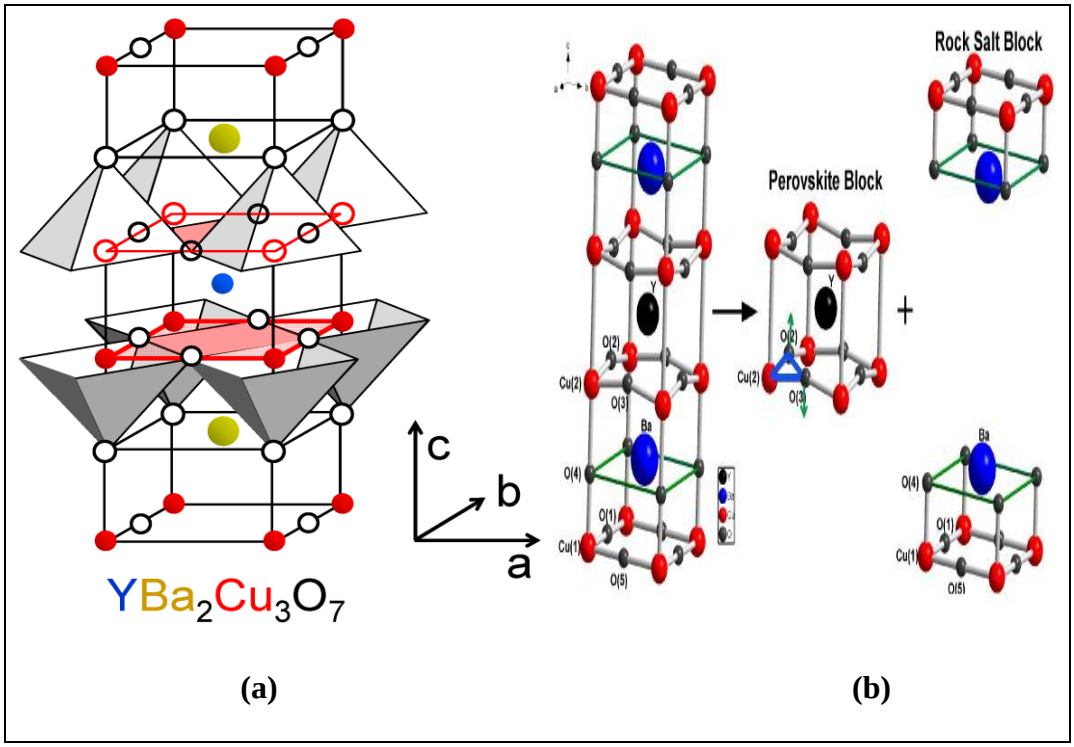

Fig. 1.9 Unit cell of (a) $YBa_2Cu_3O_7$ and (b) $YBa_2Cu_3O_{7-\delta}$. The O (5) indicates oxygen sites which are partially filled and absent in orthorhombic structure [32].

It possesses orthorhombic structure with transition temperature 92 K. Bednorz and Muller [23] in 1986 referred these HTSCs as "oxygen deficient perovskite compounds". The unit cell of YBCO is based on a stack of three perovskite cells as shown in figure 1.9 and the lattice type is either tetragonal or orthorhombic, depending on the oxygen content. The central perovskite cell contains Y atom, sandwiched between CuO_2 planes. Adjacent to the CuO_2 planes there are layers of BaO_2 and at the top and bottom of the cell there are Cu-O chains which have variable oxygen content. The CuO_2 planes forms the basic building block of all cuprates and referred as the charge conducting plane. The chains of CuO supply charge to the CuO_2 planes and act as a charge reservoir layer. The Y layer promotes anisotropy property due to motion of charge-carriers. There exists strong Josephson coupling between the CuO_2 planes in each unit cell [33, 34].

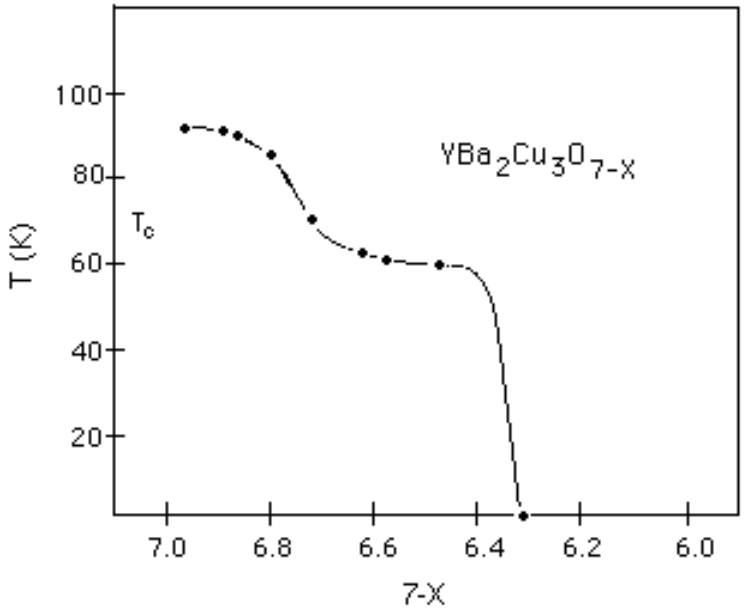

Fig. 1.10 The effect of oxygen content on the T_c of $YBa_2Cu_3O_{7-x}$ [35].

The variation of the oxygen content in YBCO is extremely important in determining the superconducting properties. An optimum T_c of 92 K is obtained for x = 0.08, but if more oxygen is removed from the structure, T_c falls rapidly and for x > 0.56, YBCO is not superconducting (Fig. 1.10).

1.6.2 Intra- and Inter-granular region in HTSC

Granularity has very significant effect on the magnetic and electrical transport properties of high T_c superconductors. Granular region forms during sintering of oxide superconducting materials due to the slow diffusion rate and kinetics in solid state process. The area of grain boundary and the nature of connectivity among grains are controlled by the amount of liquid phase. With conventional sintering process the area of fully developed boundary region with

low energy remains small and cannot be significantly increased unless a large amount of liquid phase is induced. The uneven progress of sintering process at boundary area leads to microstructural variation at grain boundaries which results in poor connectivity of the grains. These weak links result from the short intrinsic coherence length of the oxides, combined with the crystallographic defects of atomic size, such as impurities, composition variation at grain boundaries in polycrystalline ceramics, stacking faults and twin boundaries in single crystals.

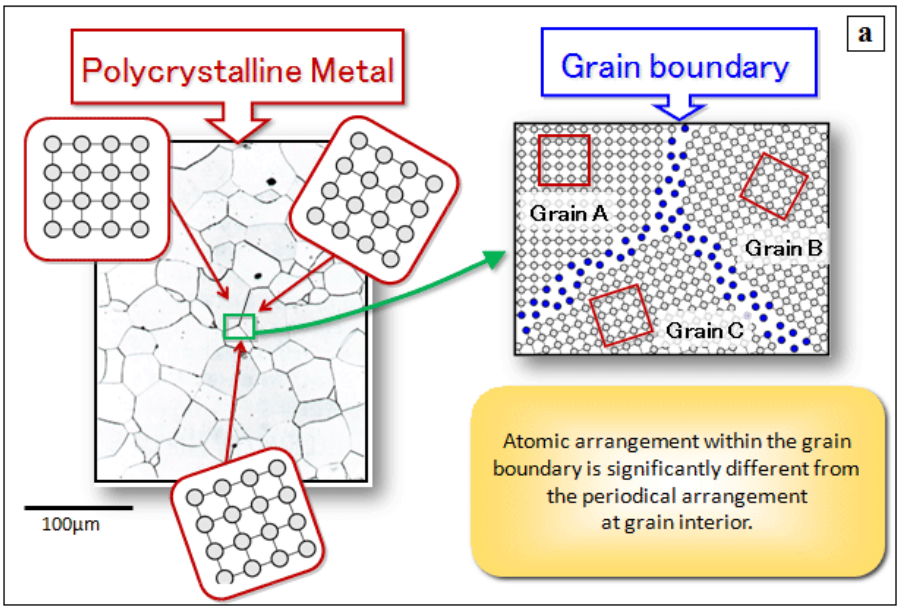

Fig. 1.11 Schematic representation of the arrangement of atoms inside the grain and grain boundary region in a polycrystalline material [36].

The weak link network is connected in a complex way and the distribution of the strengths of the weak links is very broad and depends strongly on the magnitude and direction of the local field within the weak link network.

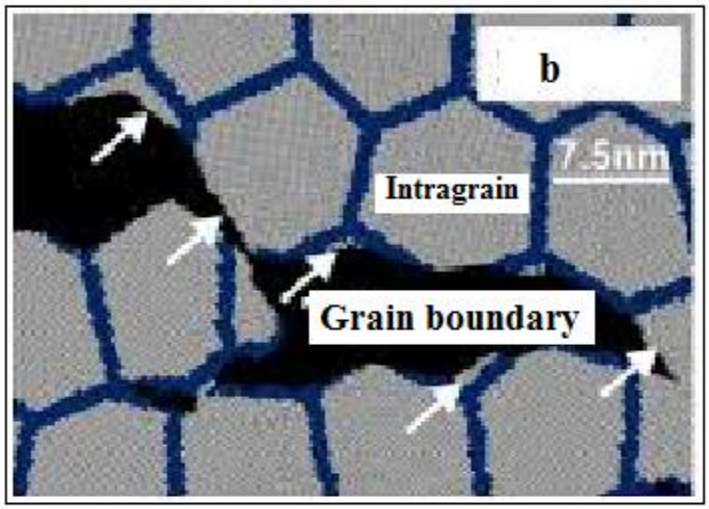

Fig. 1.12 Magnified view of intra-and inter-grain region [37].

Hence, the condensation energy for inter-grain region is smaller than intra-grain region. Therefore, the coupling between the grains diminishes with increasing energy of the system leaving only circulating currents within the grains i.e. intra-grain region. Hence, the crystal coherence and connectivity among grain boundaries have the primary importance for magnetic and transport properties of sintered polycrystalline high T_c superconductors.

1.6.3 Josephson effect and weak link behaviour

Tunnelling of Cooper pairs between two superconductors coupled by a thin non-superconducting layer is termed as Josephson effect and the junction serves as Josephson junction. Spontaneous movement of electron pairs from one superconductor to other create an electric current. The weak link may be a thin insulating barrier i.e. superconductor-insulator-superconductor junction (S-I-S) or a non-superconducting metal (S-N-S). This effect was predicted in 1962 by Brian Josephson [38, 39]. The granular HTSCs possess grain boundaries (GB) oriented in different directions. These GBs acts as weak links i.e. Josephson junctions, in sintered HTSCs ceramics. The super current decays exponentially across the GBs and depends upon barrier thickness, field strength and coherence length. Practical usage of high T_c cuprates is limited When the GBs orientation angle exceeds 3^0-5^0 [40].

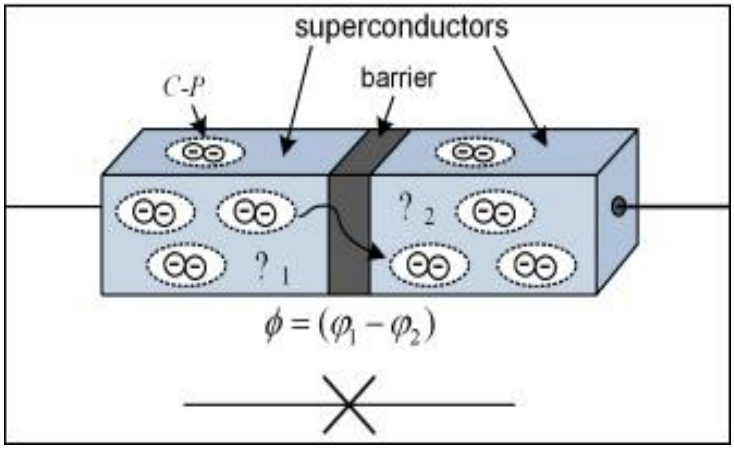

Fig. 1.13 Josephson junction array in polycrystalline HTSCs [41].

1.7 ROLE OF DEFECTS AND INHOMOGENEITIES IN CUPRATES

The layered structure of HTSC with complex crystal chemistry and the inherent granularity lead to strong structural disorder at the microscopic and mesoscopic levels. Defects play a crucial role in controlling the superconducting parameters in these systems. A large number of studies have been devoted to investigate the interplay between the superconducting order parameter fluctuation (SCOPF) and the in-homogeneities in HTSC.

1.7.1 Mesoscopic inhomogeneity

The mesoscopic in-homogeneities like grain boundaries, cracks, voids etc have much larger length scale than the coherence length (ξ_{ab} ~2nm, ξ_c ~ 0.4 nm) and are temperature independent. So they do not influence the SCOPF region [42] but strongly influence the zero resistance state. The presence of grain boundaries in polycrystalline samples, makes them brittle and deteriorating their mechanical properties. These high resistive grain boundaries acts like tunnel junctions and reduces the critical current density (J_c) of the grains [43-45]. The cuprates are highly anisotropic with high resistivity along c-axis (ρ_c) than the ab-plane (ρ_{ab}) and also imposes restriction on the flow of current depending on the alignment of grains. The greater the angle of misorientation at the grain boundary, the less is the critical current [46, 47].

1.7.2 Microscopic inhomogeneity

The microscopic in-homogeneities such as structural defects (twin boundaries, stacking faults) and chemical imperfections (oxygen deficiencies) occur inside the grains during the preparation process. The length scale of these in-homogeneities is smaller than that of the mesoscopic in-homogeneities, but still larger than ξ. These in-homogeneities should have negligible effect on the SCOPF region [48]. However, many studies have shown that these in-homogeneities crucially influence both the critical and the mean field region of SCOPF [49, 50]. The critical region expands with the increase of secondary phases in YBCO and its composites [51]. These in-homogeneities also affect the Lawrence-Doniach crossover temperature (T_{LD}) in the mean field region.

1.7.3 Vortex pinning by defects

The external magnetic field penetrates into the HTSC in the form of discrete bundles (Fig. 1.14 a). Each flux line consists of whirlpools of current known as vortex. Movement of these vortices can impede the flow of charge carriers leading to the destruction of superconductivity state in these materials even at moderate magnetic field. Controlling the movement of the vortices can lead to the increase in critical current density of HTSC in magnetic field. Chemical impurities and the intrinsic defects residing in the structure of HTSC pin the vortices at the location of the impurities by arresting their easy movement in the material (Fig. 1.14 b). Vortex lines prefer to sit at the impurity or defect sites of the material because by doing so, they lower their energy. Since cuprates are of laminar character, these defects can

pin the vortices in the form of pancakes rather than continuous cylinders. The enhancement of vortex pinning is an issue of profound technological importance [52].

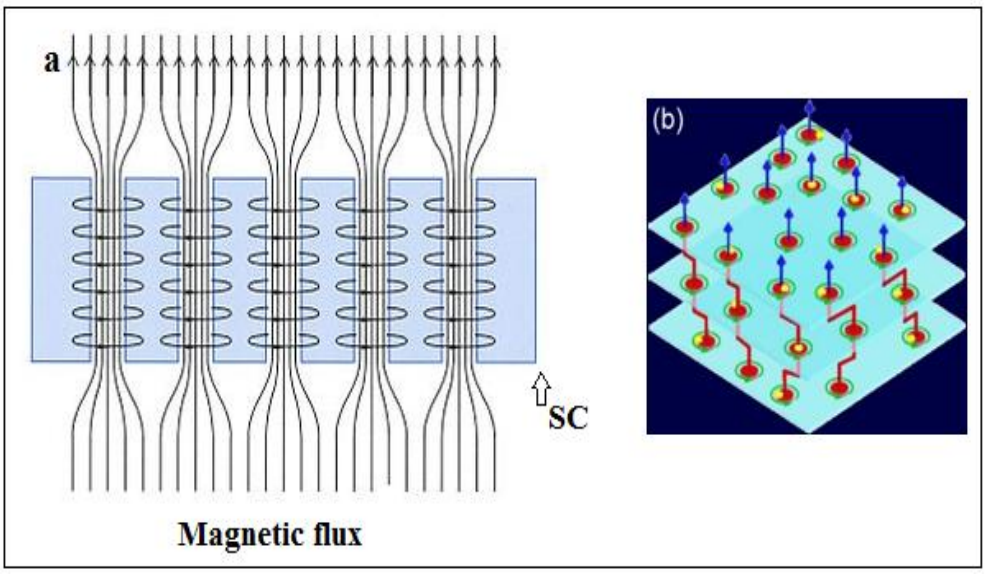

Fig. 1.14 (a) Schematic representation of how magnetic field enters into superconductor in bundles (b) Trapping of magnetic field or pinning of vortices by defects [53].

1.7.4 Irradiation Induced defects in cuprates

In-homogeneities can be induced by irradiating the materials with high energy and low energy ion beams. Energetic ion beams play a vital role in the field of research in materials science. The effect of ion beams on the materials depends on the ion energy, fluence and ion species. Energetic ions lose their energy during passage through HTS material mainly by two processes (Fig. 1.15): (i) by inelastic collisions of the highly charged energetic particles with the atomic electrons of the matter and exciting or ionising the atoms (electronic energy loss $(dE / dx)_e$ or electronic stopping) (ii) elastic scattering from the nuclei of the atoms of the matter and displacing atoms (nuclear energy loss $(dE/dx)_n$ or nuclear stopping) [52]. The nuclear stopping is dominant at low energies and Electronic stopping is dominant at high energies. Heavy ions with high energy are referred as swift heavy ions (SHI). It is expected that the lattice atoms are not displaced in the case of electronic excitation generated by SHI. During the passage of SHI the kinetic energy of the ejected electrons is transmitted to the lattice by electron-phonon interaction which results in the increase of local lattice temperature above the melting point of the material. The temperature increase is followed by a rapid quenching, which results in an amorphous columnar structure when the melt solidifies [54-56].

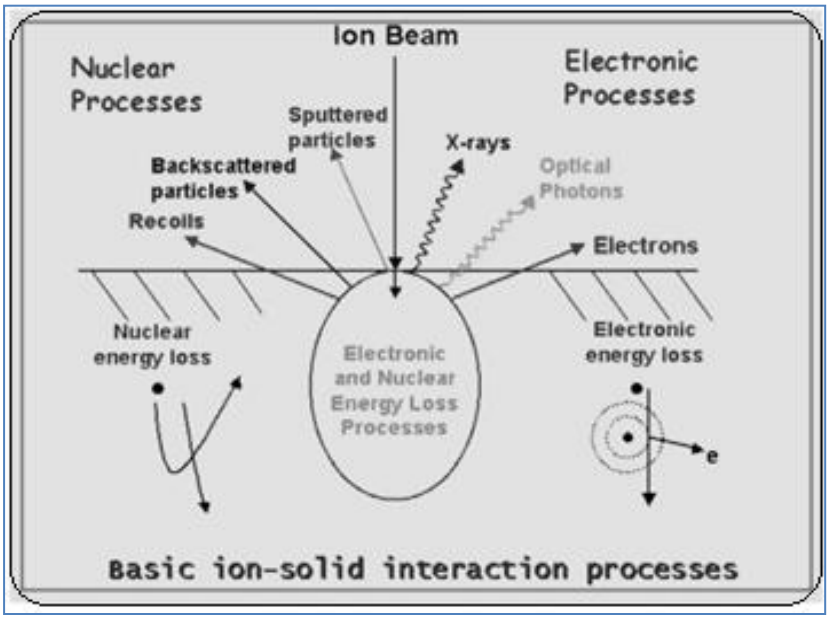

Fig. 1.15 Basic ion-solid interaction process [57].

The basic difference of materials modification by low energy ion implantation (energy in the range of few tens of keV to a few MeV) and swift heavy ion irradiation (energy in the range of few tens of MeV and higher) is that the low energy ions get embedded in the material and cause modification by their presence due to the collision cascade produced by the impinging ions. But in SHI irradiation, the modification of thin films or the near-surface region of the bulk sample occurs due to electronic excitation. In this case, the impinging ions do not get embedded in the film due to their large range (few tens of μm or larger). The modification due to ion irradiation is mainly due to the intermixing of the film atoms and the substrate atoms. Normally the fluence required for ion beam mixing with low energy ions is 10^{16} ions/cm^2. The fluence required for mixing with SHI is about 10^{13} ions/cm^2. The cause of mixing is the displacement of atoms by the electronic excitation and not by the elastic collisions because of the fact that the electronic energy loss is about two orders of magnitude larger than the energy loss due to the nuclear stopping. Unlike ion beam mixing by low energy ions, SHI induced mixing does not have the impinging ions in or near the mixed phase region. Due to high energy, the SHI gets embedded far deep in the substrate, quite away from the mixed region. The effect of introduction of columnar defects into the cuprate superconductors using swift heavy ion irradiation have been the subject of many investigations, because such defects provide the means of pinning the flux lines along its entire length rather than occasional pinning due to a random distribution of point defects [52]. If the diameter of the defects can be made close to the coherence length, then the pinning force at defect sites can be increased considerably for the vortex parallel to the direction of the columns. By controlling the number

of defects per unit area the critical current J_c, can be improved drastically [58-60]. The defect controlled charge transfer in composites and doped systems of superconductors can be studied by swift heavy ion (SHI) interaction. SHI irradiation shows the damaging of insulating grain boundaries and this in turn destroys the superconducting phase coherence. Ion irradiation brings about an improvement in the microstructure that induces alignment of the grains in a randomly oriented granular superconductor [61]. The effect of SHI irradiation on various superconducting and normal state parameters like T_c, J_c, transition width, normal state resistance and its temperature dependence has been probed.

1.8 LITERATURE REVIEW PERTAINING TO COMPOSITES

YBCO is an extensively studied high T_c superconducting material sustaining superconductivity above the boiling point of liquid nitrogen (77 K). Reviews on $REBa_2Cu_3O_{7-\delta}$ (RE = Y, Sm, Nd, etc) coated conductors indicated its valuable future practical applications [62, 63]. However, the randomly oriented grains in polycrystalline bulk material impose complexity in conduction process. The inter-grain boundaries behave as weak link Josephson junctions. Hence, a percolative type of approach has been used to analyze both superconducting and normal state properties [64, 65]. The intrinsic defects like mismatched grains, voids, cracks, grain growth and secondary phases etc, control the granularity in HTSCs [66]. The chemical additives i.e. nano inclusions, secondary phases of ferroelectric embedding and magnetic inclusions play a key role in modifying the grain boundary by filling the voids and cracks. The difficulty arising due to granularity could be overcome by composite formation with some metals like Au, Ag, Al etc, and voids problem may be sorted out by additions of non-superconducting phases like $BaZrO_3$ (BZO), $BaTiO_3$ (BTO), $BaSnO_3$ (BSO), $BaTiO_3$-$CoFe_2O_4$ (BTO-CFO), Cr_2O_3 which modifies electrical, magnetic and mechanical properties [67-70]. Besides, filling the inter-granular spaces these non-superconducting inclusions generate artificial pinning centers that slow down the vortex motion serving as potential pinning sites for magnetic flux lines.

Composite of BSO with YBCO creates nano-columns in YBCO thin films when proper processing conditions were used [71]. These BSO nano-columns particularly contribute to pinning in the c-axis orientation, with J_c is increases by more than two orders of magnitude in high fields. The c-axis correlated defects created by the $BaSnO_3$ particles could help in enhancing the anisotropy of the critical current density [72, 73]. We have reported that

addition of BSO to bulk YBCO does not affects the grain size much and improves the oxygen ordering in the samples [74].

BTO-CFO composites are interesting Magneto-Electric materials due to the individual properties of their components. $CoFe_2O_4$ has a spinel structure with large coercivity and magnetostriction [75]. $BaTiO_3$ exhibits polymorphs depending on the temperature, which is most interesting due to its ferroelectric and piezoelectric properties. Wee et al. have shown that BTO-CFO composite possess enhanced flux pinning property with addition to YBCO matrix [70]. We have reported that BTO-CFO does not affect the grain size much more, but it degrades the grain connectivity and transition temperatures [76].

Isber et al. have shown that low concentration addition of Cr_2O_3 enhances the T_c of YBCO but in high percentage T_c is degraded [77]. We have reported the decrease in grain size due to addition of Cr_2O_3 with improved oxygen ordering. Splitting of transition temperature occurs due to the incorporation of Cr_2O_3 to the grain boundary region [78].

Mohanta et al. have shown that BZO addition to YBCO enhance the J_c value with slight increase in the superconducting transition temperature T_c. Generally, BZO occupies the boundaries of YBCO grains and with the application of magnetic field secondary peak in the temperature derivative of resistivity curve has been observed [79, 51]. It also occurs in clumps filling voids between grains and bulk systems [80, 81].

Ferroelectric material BTO possess similar perovskite lattice structure with that of YBCO. Its crystal chemistry has shown to generate a stress field which acts as pinning centers [82, 83]. Research group has studied the fluctuation conductivity in polycrystalline samples of YBCO/BTO in inter and intra-grain region. The strong influence of BTO content in the composites in the mean field region has been explained and long range superconducting order has been observed due to thermally assisted percolation process through the weak links between the grains [84, 85].

1.9 LITERATURE REVIEW PERTAINING TO DOPING

All the high T_c superconductors are resulted from substitution at one or more cationic sites in the parent material. Since these studies provide a very good probe to understand the mechanism behind superconductivity, they become important from the fundamental point of view.

In YBCO the Y site has been replaced completely or partially with other rare earths and it is found that these substitutions do not affect T_c with the exception of one or two elements like Pr, Tb, Ce, etc [86]. However, substitution at the Ba site with other alkaline earth elements has been found to decrease T_c [87]. Partial substitution for oxygen by fluorine [88] claims a rise in T_c even near to room temperature. But such compounds are found to be highly unstable and the results are often not reproducible. Substitution at the Cu site is most important among all the cations of YBCO, as Cu-O networks play a major role for the occurrence of superconductivity in these materials. For this reason, the Cu site has been doped with almost all the elements. Among them, the 3d transition elements are considered ideal for doping at the Cu site as they have similar electronic configuration and ionic sizes as Cu.

Incorporation of Zn in CuO_2 planes has a dramatic effect on superconducting transition temperature. Zn^{2+} is a non-magnetic and stable 2+ ion. The presence of such ions disturbs the antiferromagnetically coupled spin fluctuations in the CuO_2 planes. Antiferromagnetically coupled spin fluctuations are essential for superconductivity in cuprate systems. The local moments developed due to slowing down of such fluctuations in Zn doped samples of YBCO reduce the strength of Cooper pairs and hence lead to a large suppression of T_c. It also causes atomic displacement and shortening of Cu (1)-O (1) bond length and elongation of Cu(2)-O(1) bond length by 8 to 12%. The hole from the Cu(1) site is interrupted to go to Cu(2) site through the apical oxygen located just below the doped Zn i.e. a hole supplied channel to Cu(2) site is lost by doping a Zn atom. As a consequence, the T_c is reduced [89, 90]. The orthorhombic structure of YBCO is retained with substitution by both Zn and Ni. However, due to Ni doping, T_c suppression is only about half of that due to Zn doping [91].

The valence state of Ti^{4+} is higher than that of Cu^{2+} and substitution of Ti for Cu may decrease the mobile carrier concentration due to hole filling by Ti. Therefore, it is of interest to investigate the effect of Ti substitution for Cu in YBCO on structure, superconductivity, and oxygen content [92]. Yanmaz et al. have reported that for 1 % to 5 wt. % addition of titanium caused a decrease of transition temperature where as 7 to 10 wt. % addition caused a slight increase of transition temperature in YBCO [93]. Nishi et al. have reported that the small amount of titanium addition decreases a and b lattice parameters, whereas ‘c’ does not depend on titanium addition. Excess titanium addition increases a, b and c lattice parameters [94]. We have reported that Ti doping did not improve the weak-link behaviour of the superconducting grains and the critical temperature, T_c. But the normal state resistivity is low

in comparison to the pristine sample in low percentage addition of TiO_2 and grain size reduced [95].

In YBCO, the nature of the charge reservoir layer and the mechanism of charge transfer has been studied through preferential chemical substitutions by trivalent ions like Ga^{3+}, Fe^{3+}, Al^{3+}, Co^{3+} and monovalent ions like Ag^{1+}, Au^{1+} in the CuO chain [96,97]. Such substitution studies have clearly indicated a drastic change in the structure without much change in the superconductivity. Hence, it gives an impression that structural features in the ab-plane may not have much relevance to superconductivity. As the impurity atoms occupy the lattice sites in the CuO basal plane they change the oxygen coordination around neighbouring Cu (1)s. Fe, Co, Ni prefer octahedral oxygen coordination site rather than 4-fold coplanar coordination of Cu(1)s. Presence of octahedrally coordinated impurity ions in Cu(1) site disturb the Cu-O chain and cause an average tetragonal symmetry [98].

Noble metals like Au, Ag when doped in YBCO, substitutes preferentially for the Cu (1) site in CuO basal plane. Neutron diffraction studies showed that in Au doped YBCO the Cu (1)-O (1) bond length expands while Cu(2)-O(1) bond length shortens [99]. Many research groups have reported that T_c remain almost independent in Ag doped YBCO system, whereas some group have shown that T_c increases at a moderate doping regime, reaches a plateau and then decreases at doping levels beyond 0.3 atoms per unit cell [100,101]. Au doping in YBCO has also cause T_c enhancement by about 2 K and reduce normal state resistivity by filling inter-granular spaces [102].

1.10 LITERATURE REVIEW PERTAINING TO IRRADIATION

The controlled defects produced by a collision cascade obtained by fast-moving neutrons, point defects created by low energy ion impact [103-105] and columnar defects [106] generated by swift heavy ion (SHI) resulted in significant enhancement of parent material property. Because of the huge energy loss, the ions in a medium can bring about several changes in the target system such as annealing of defects, additional defects [107], resistivity enhancement [108], phase change [109], creeping in amorphous material [110], and tracks in crystalline alloys [111] and in insulating oxides [112]. Since ion irradiation modifies the local geometrical arrangements through introduction of defects, large number of studies [113,114] has been directed towards understanding the irradiation induced resistivity changes in HTSCs.

Marwick et al. [115] have shown the exponential increase in resistivity in higher dose of irradiation. The exponential increase in resistivity is accompanied by a metal to insulator transition and this can be attributed as to progressive localization of charge carriers culminating in trapping with thermally activated hopping at high doses. Albenque et al. [116] have also explained about this fact as the reduced tunnelling of charge carriers at the grain boundaries which get affected faster than the grains under GeV range ion beam. The tunnelling conductance exponentially depends on the grain boundary thickness and gives rise to the exponential rise of resistivity with fluence. The increased resistance due to ion irradiation is caused due to both by the trapping of the carriers on the created defects and by the decrease of the carrier mobility, particularly due to scattering on ionized defects. Though both the mechanisms contribute to irradiation induced increase in resistance, in a few cases the normal state resistance has been shown to decrease by ion irradiation. This type of resistance variation is highly dependent on the initial quality of the sample and is observed mostly at low fluence.

1.11 LITERATURE REVIEW PERTAINING TO FLUCTUATION CONDUCTIVITY

The thermal fluctuations in HTSC give a finite probability of the formation of Cooper pairs which results excess conductivity during the transport of carriers [117,118]. For all high temperature superconductors, the fluctuation phenomena have been observed and their investigation takes a significant part of the complete understanding of these materials. The interplay between the intrinsic thermal fluctuation effects around the superconducting transition temperature and the extrinsic inhomogeneity effects associated with stoichiometric and structural in-homogeneities at different length scales was already an important problem in low temperature superconductors (LTSC). The unique features of HTSCs are characterized by very short coherence length [38], anisotropy property [119,120] and high T_c which greatly influences superconducting order parameter fluctuations (SCOPF). The Cooper pair formation begins much before T_c at T* (pseudogap temperature) but undergoes a continuous thermodynamic fluctuations due to annihilation and creation of electron pairs. Typical resistive behaviour of YBCO is reported in Fig. 1.16 and can be described as follows: as one approaches T_c the superconducting density increases and macroscopic phase coherence occurred below T_{c0} (zero resistance critical temperature). While approaching from higher

temperature side, the fluctuations have the characteristics of a quasi-1D and quasi-2D geometries, but close to T_c, a crossover occurs to homogeneous 3D Gaussian fluctuations.

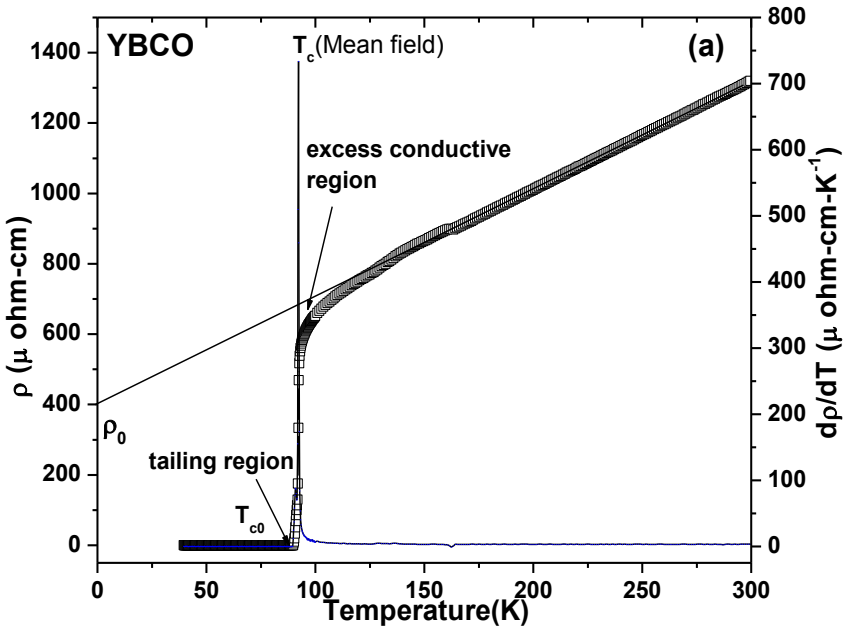

Fig. 1.16 Resistive transition and regular resistivity behaviour extrapolated from the normal behaviour. Linear fitting of resistivity in the temperature range 150 to 250 K and extrapolated to 0 K gives resistivity slope (dρ /dT) and residual resistivity (ρ_0) for cuprates.

The short coherence lengths of the high T_c cuprate superconductors produce a significant rounding of the transition curve, which provides for the possibility to study fluctuating superconducting pairs over an extended temperature region above the transition temperature T_c. Such studies are of interest and may give estimates of microscopic parameters such as the coherence lengths, phase breaking time and dimensionality. Excess conductivity in high T_c superconductors seems to appear as a consequence of second order phase transition. The fluctuation effects influence magnetic susceptibility, magneto-resistance [121] and Hall Effect [122] etc. Fluctuation studies give microscopic information on coherence length, dimensionality of conduction and its associated crossover temperature [123,124]. SCOPF analysis is the important aspect of the thesis under inhomogeneity addition and irradiation impact. In order to calculate the dimensionality cross-over, various models has been proposed. They are Aslamazov-Larkin (AL), Lawrence-Doniach (LD) and Maki-Thompson models (MT) as described elaborately in chapter 3.

1.12 MOTIVATION

In the present thesis, an attempt has been made to understand the interplay between the in-homogeneities, secondary phases and the thermal fluctuations around the superconducting

transition. The excess conductivity or paraconductivity region is affected much by the presence of in-homogeneities. The main purpose of this study is to explore the physics of doped and composite cuprate superconductors near the superconducting transitions through the evaluation of SCOPF. We address the problem around superconducting transitions and the role of in-homogeneities and SCOPF effects in a set of YBCO/BSO, YBCO/BTO-CFO, YBCO/Cr_2O_3 composites and YBCO/Ti doped samples.

The dielectric inhomogeneity $BaSnO_3$ has been investigated thoroughly as composite with YBCO in bulk as well as in thin film forms, studying all its properties and has achieved great recognition for artificial pinning agent. This material raises our interest to be added with YBCO and combine its effects with point defects generated by low energy ion irradiation. Literature does not provide dual impact of defects created by ion irradiation and inclusion of BSO. Hence, our work includes a systematic study on the transport property of YBCO/BSO samples with varying BSO wt.% in bulk form as well as low energy Argon (Ar^{+1}), Oxygen (O^{+1}) and Krypton (Kr^{+1}) irradiated YBCO/1wt.% BSO composite thin films with different ion fluences analyzing structural disorder, microstructure, resistivity and fluctuation conductivity.

BTO-CFO and Cr_2O_3 are two important composite materials. Reported works focus only on the pinning aspect of this material. No rigorous work has been done yet on the fluctuation conductivity of these materials as composite with YBCO. Here attempts have been taken to analyse the impact of magneto-electric material (BTO-CFO) and magnetic element (Cr_2O_3) on the structural property and DC electrical resistivity of YBCO matrix.

The transition element Ti is attractive for capacitor application in microelectronics due to its high dielectric constant. As the valence state of Ti^{4+} is higher than that of Cu^{2+}, it's substitution for Cu may decrease the mobile carrier concentration due to hole filling by Ti. The fluctuation conductivity of Ti doped YBCO has not yet been studied rigorously. Here a detailed study on the structural modification and fluctuation conductivity near the SCOPF region for Titanium doping for the cu site of YBCO is presented.

1.13 OBJECTIVE AND OUTLOOK OF THE THESIS WORK

The objective of the work is to study the structural and electrical transport property on YBCO composite material with and without irradiation effect. The samples under investigation are highlighted below.

(i) Superconducting bulk YBCO phase with T_c ~ 92 K

(ii) (1-x) YBCO/ x BSO bulk composites with x = 0.0, 0.1, 0.3, 0.5, 1.0, 2.5, 5.0 wt. %

(iii) (1-x) YBCO/ x Cr_2O_3 bulk composites with x = 0.0, 2.3, 4.4, 6.1,7.4 wt. %

(iv) (1-x) YBCO/x BTO-CFO bulk composites with x = 0.0, 0.2, 0.4, 0.6 wt.%

(v) $YBa_2 (Cu_{1-x}Ti_x)_3O_{7-y}$ (x = 0.0, 0.01,0.02,0.04,0.05) doped superconductor.

(vi) YBCO/ 1wt.% BSO composite PLD thin film irradiated with 100 keV O^{+1}, Ar^{+1}, Kr^{+1} ions with varying fluence.

The outlook of the whole thesis:

Chapter 1 Introduction to superconductivity discussing its different types and phenomenological theories involved in this thesis has been discussed. The role of inhomogeneity, defects and pinning centers in HTSCs are discussed. Important aspects of irradiation and its impact on superconducting materials have been discussed. Further, the chapter highlights on the parent compund chosen describing the crystal structure of YBCO and focussing on literature reviews. The chapter ends with motivation followed with objectives of the work carried out in the thesis.

Chapter 2 This chapter is concerned with sample preparation and characterization techniques. The synthesis of $YBa_2Cu_3O_{7-\delta}$ (YBCO), $BaSnO_3$ (BSO), Cr_2O_3, $BaTiO_3$-$CoFe_2O_4$ and thin films of YBCO/BSO composite by PLD technique is discussed. The effect of low energy ion beam irradiation on superconducting samples is discussed.

Chapter 3 This chapter gives an elaborative description of the normal state and paracoherent resistivity of granular superconductors with their general properties. The method of analysis of the fluctuation conductivity by different theoretical model fittings and the dimensionality of fluctuations has been discussed.

Chapter 4 In this chapter attempts have been made to study superconducting properties in composite and doped systems of YBCO. The structural and electrical transport property of YBCO/ x BSO, YBCO/ x Cr_2O_3 and YBCO/ x BTO-CFO bulk composite systems has been investigated with varying concentration. The systems have been analyzed for fluctuation conductivity, emphasizing on the conduction mechanism.

Chapter 5 In the present chapter we discuss some of our recent results on modification of structure, microstructure and superconducting properties due to microscopic and the mesoscopic inhomogeneities in $YBa_2(Cu_{1-x}Ti_x)_3O_{7-y}$ (x=0.01,0.02,0.04,0.05) doped superconductor. We analyze the mechanism of charge transfer in YBCO when its charge

reservoir layer is perturbed due to doping with 3d transition element TiO_2. Doping to the Cu site of YBCO has significantly influence the structure and the excess conductivity region as well as the tailing region.

Chapter 6 Effect of irradiation with 100 keV O^{+1}, Ar^{+1}, Kr^{+1} ion on structure, microstructure and electrical transport properties of YBCO/1 wt. % BSO composite thin films is studied. The crystallographic modification is correlated with transport property.

Chapter 7 This chapter deals with conclusions and important findings of the present work. It gives future direction of work on the related aspects.

1.14 References

[1] D.V. Delft, P. Kes, Physics Today 63 (9) (2010) 38.

[2] A.M. Forrest, Eur. J. Phys. 4 (1983)117.

[3] http://en.wikipedia.org/wiki/Superdiamagnetism.

[4] http://web.ornl.gov/info/reports/m/ornlm3063r1/pt3.html.

[5] F. London and H. London. Proc. Roy. Soc. A 149 (1935) 71.

[6] V. L. Ginzburg and L. D. Landau. Zh. Eksp. Teor, Fiz. 20 (1064) 1950.

[7] J. Bardeen, L. N. Cooper and J. R. Schrieer, Phys. Rev. 108 (1957) 1175.

[8] L.N. Cooper, Phys. Rev. 104 (1956) 1189.

[9] webs. mn.catholic.edu.au.

[10] L.P. Gorkov, Sov. Phys. JETP 36 (9) (1959) 1364.

[11] inspirehep.net.

[12] T. Hartikainen, J. Lehtonen and R. Mikkonen, Supercond. Sci. Technol. 16 (2003) 963.

[13] N. Murata, J. Haruyama, J. Reppert, A. M. Rao, T. Koretsune, S. Saito, M. Matsudaira, and Y. Yagi, Phys. Rev. Lett. 101 (2008) 027002.

[14] J. G. Bednorz and K. A. Müller, Z. Physik, B-Condensed Matter 64 (1986) 189.

[15] K.A. Muller and J.G. Bednorz, Proc. Natl. Acad. Sci. USA 84 (1987) 4678.

[16] M. K. Wu , J. R. Ashburn, C. J. Torng, P. H. Hor, R. L. Meng, L. Gao, Z. J. Huang, Y. Q. Wang, and C. W. Chu, Phys. Rev. Lett. 58 (1987) 908.

[17] N. M. Plakida, L. Antona, S. Adama, and Gh. Adama, J. of Experimental and Theoretical Physics 97 (2003) 331.

[18] D.J. Scalapino, Phys. Reports. 250 (1995) 329.

[19] iramis.cea.fr.

[20] P. W. Anderson, Science 235 (1987) 1196.

[21] F. Onufrieva and P. Pfeuty, PRL 102 (2009) 207003.

[22] T. Dahm and L. Tewordt, Phys. Rev. Lett. 74 (1995) 793.

[23] J. G. Bednorz and K. A. Muller, Z. Phys. B 64 (1986) 189.

[24] V. V. Kabanov and D. Mihailovic, J. Supercon. 13 (2000) 959.

[25] D. Mihailovic and V. V. Kabanov, Phys. Rev B 63 (2001) 054505.

[26] B. J. Kochelaev, J. Sichelschmidt, B. Elschner, W. Lemor, A. Loidl, Phys. Rev. Lett. 79 (1997) 4274.

[27] http://www.toulouse.lncmi.cnrs.fr/.

[28] H. Alloual, F. Rullier-Albenque, B. Vignolle, D. Colson, A. Forget, arXiv:1006.3165 (cond-mat.supr-con).

[29] D.E. Ford, S.S. Scott, S.S. Ang and W.D. Brown, Proceedings Arkansas Academy of Science 48 (1994) 45.

[30] E. U.S. Koyama and T. Kawai, Jpn. J. Appl.Phys. 27 (1988) L1467.

[31] E. U.S. Koyama and T. Kawai. Jpn. J. Appl. Phys. 28 (1989) L190.

[32] http://www.wmi.badw.de/.

[33] M. Suzuki and T. Watanabe, Phys. Rev. Lett. 85 (2000) 4787.

[34] Y. Yamada, K. Anagawa, T. Shibauchi, T. Fujii, T. Watanabe, A. Matsuda, and M. Suzuki, Phys. Rev. B 68 (2003) 054533.

[35] http://www.scielo.br/.

[36] http://www.bnm.mtl.kyoto-u.ac.jp/.

[37] http://cacs.usc.edu/.

[38] B. D. Josephson, Physics Letters 1 (1962) 251.

[39] B. D. Josephson, Rev. Mod. Phys. 46 (2) (1974) 251.

[40] D. Dimos, P. Chaudhari, J. Mannhart, Phys. Rev. B 41 (1990) 4038.

[41] http://postreh.com/.

[42] J. Maza and F. Vidal, Phys. Rev. B Condensed Matter 43 (1991) 10560.

[43] S. Lee, J. Park, G. Park and K. Lee, Supercond. Sci. Technol. 9 (1996) A5.

[44] P. H. Hor, L. Gao, R.L. Meng, Z.J. Huang, Y.Q. Wang, K. Forster, J. Vassilious, C.W. Chu, M.K. Wu, J.R. Ashburn and C.J. Torng, Phys. Rev. Lett. 58 (1987) 911.

[45] B.W. Veal, H. You, A.P. Paulikas, H. Shi and J.W. Downey, Phys. Rev. B 42 (1990) 4770.

[46] D. Dimos, P. Chaudhuri, I. Mannhart, F. Legoues, Phys. Rev. Lett. 61 (1988) 219.

[47] M. Prester, Supercond. Sci. Technol. 11 (1998) 333.

[48] E.J. Cukauskas and L.H. Allen, J. Appl. Phys. 84 (1998) 6187.

[49] D.K. Aswal, A. Singh, S. Sen, M. Kaur, C.S. Viswandham, G.L. Goswami and S.K. Gupta, J. Phys. and Chem.of Solids 63 (2002) 1797.

[50] T. Sato, H. Hakane, S. Yamazaki and N. Mori, Physica C 372 (2002) 1208.

[51] A. Mohanta and D. Behera, Physica C 470 (2010) 295.

[52] D. Kanjilal, Vacuum 48 (1997) 979.

[53] http://hoffman.physics.harvard.edu/research.

[54] A. Dunlop, D. Lesueur and H. Dammak, Nucl. Instrum. Methods B 90 (1994) 330.

[55] T.A. Tombrello, Nucl. Instrum. Methods B 103 (1995) 318.

[56] D. Lesueur, Radiat. Eff. & Defects Solids 126 (1993)123.

[57] http://www.iopb.res.in/~tsom/research.htm-Ion.

[58] A. K Pradhan, S.B Roy, P. Chaddah, D. Kaijilal, C. Chen and B.M Wanklyn, Supercond. Sci. Technol. 9 (1996) 743.

[59] R.C Budhani, W.L. Holstein and M. Suenaga, Phys. Rev. Lett. 72 (1994) 566.

[60] W. Jiang, N.C Yeh, D.S Reed, U. Kriplani, D.A Beam, M. Konczylowski, T.A Trombello and F. Holtzberg, Phys. Rev. Lett. 72 (1994) 550.

[61] D. Behera, K. Patnaik, N.C Mishra, Modern Physics Letters B 15 (2001) 69.

[62] D. C. Larbalestier, A. Gurevich, D. M. Feldmann, A. Polyanskii, Nature 414 (2001) 368.

[63] S. R. Foltyn, L. Civale, J. L. M. Driscoll, Q. X. Jia, B. Maiorov, H. Wang, M. Maley, Nat. Materials. 6 (2007) 631.

[64] J.A.Veira and F. Vidal, Physica C 159 (1989) 468.

[65] A. Diaz, J. Maza, F.Vidal, Physical Rev. B 55 (1997)1209.

[66] Y. Y. Luo, Y. C. Wu, X. M. Xiong, et al., J. Supercon. & Novel magnetism 13 (2000) 575.

[67] M. Peurla, H. Huhtinen, M.A. Shakhov et al, Phys. Rev. B 75 (2007) 184524.

[68] J. L. Macmanus-Driscoll, S.R. Foltyn, Q.X. Jia, et al. Nat. Mater. 3 (2004) 439.

[69] D. Behera, N.C. Mishra, Supercond. Sci. Technol. 15 (2002) 72.

[70] S. H Wee, J. Shin, C. Cantoni, Y. L Zuev, S. Cook, A. Goyal , Supercond. Sci. Technol. 23 (2010) 014007.

[71] C. V. Varanasi, J. Burke, H. Wang, J. H. Lee and P. N. Barnes, App. Phy. Lett. 93, (2008) 092501.

[72] C. V. Varanasi, P. N. Barnes, J. Burke, L. Brunke, I . Maartense, T. J. Haugan, E. A. Stinzianni, K. A Dunn, P. Haldar, Supercond. Sci. Technol. 19 (2006) L37.

[73] P. Mele, K. Matsumoto, T. Horide, A. Ichinose, M. Mukaida, Y. Yoshida, S. Horii, R. Kita, Supercond. Sci. Technol. 21 (2008) 032002.

[74] M. Sahoo, D. Giri, D. Behera, J. Low Temp.Phys. 177 (2014) 257.

[75] J. B. Silva et al., Mater. Sci. Eng. B 112 (2004) 182.

[76] M. Sahoo, D. Behera, International J of Morden Physics B 27 (2013) 1350099.

[77] S. Isber and C. Madi, J of Physics: Conference Series 97 (2008) 012130.

[78] M. Sahoo, D. Behera, J of Physics and Chemistry of Solids 74 (2013) 950.

[79] A. Mohanta, D. Behera, Solid State Communications 150 (2010) 1325.

[80] S. Kang, K. J. Leonard, P. M. Martin, J. Li and A. Goyal, Supercond. Sci. Technol. 20 (2007) 11.

[81] N. M. Kirby, N.W. Chen-Tan, C.E. Buckley, J of the European Ceramic Society 27 (2007) 2039.

[82] W. Gawalek, T. Habisreuther, K. Fischer, G. Bruchlos, P. Gornert, Cryogenics. 33 (1993) 65.

[83] M. A Sekkina, A. R Tawfik, O. Hemeda, M. A.T. Dawoud, S. Elattar, Turk J Phys, 29 (2005) 329.

[84] A. Kujur, A. Mohanta and D. Behera, International J. of Material Science. 5 (2010) 683.

[85] A. Mohanta, D. Behera, S. Panigrahi and N. C. Mishra, Indian J. Phys. 83 (2009) 455.

[86] Z. Fisk, J. D. Thompson, E. Zirngiebi, J. L. Smith and S.W. Cheong, Solid State Commn. 62 (1987) 743.

[87] N.S. Raman and B. Viswanathan, Bull. Mate. Sci. 16 (1993) 381.

[88] S. R. Ovshinsky, R. T. Young, D. D. Allred, G. Demaggio and G. A. Van Der Leeden, Phys. Rev. Lett. 58 (1987) 2579.

[89] W. H. Fietz, R. Quenzel, H. A. Ludwig, K. Grube, S. I. Schlachter, F.W. Hornung, T. Wolf, A. Erb, M. Klaser, G. Muller-Vogt, Physica C 270 (1996) 258.

[90] A. Li, Y.N Wang, X.N. Ying, Q.M. Zhang and W.M Chen, Supercond. Sci. Technol. 12 (1999) 645.

[91] N. Peng and W.Y. Liang, Physica C 223 (1994) 61.

[92] K. M. Jadhav, R. L. Raibagkar, G. K. Bichile, D. G. Kuberkar, and R. G. Kulkarni, J of Superconductivity 8 (1995) 373.

[93] E. Yanmaz, S. Balci, T. Kucukomeroglub, Materials Letters 54 (2002) 191.

[94] Y. Nishi, S. Moriya, S. Tokunaga, J of materials science letters 7 (1988) 359.

[95] M. Sahoo, D. Behera, J of Supercon. Nov Magn. 27 (2014) 83.

[96] J.V. Andersen, N.H. Andersen, O.G. Mauritsen and H.F. Poulsen, Physica C 214 (1998) 143.

[97] R. Suryanarayan, L. Ouhammou, O. Gorochov and H. Pankowska, Physica C 199 (1992) 37.

[98] B. W. Veal, A. P. Paulikas, H. You, H. Shi, Y. Fang, J. W. Downey, Phys. Rev. B 42 (1990) 6305.

[99] M.Z. Cieplak, G. Xiao, C. Chien, A. Bakhashi, D. Artymowicz, W. Bryden, J.K. Stalick and J.J. Rhyne, Phys. Rev. B 42 (1990) 6200.

[100] A.P. Li, Q.N. Ni, Q.P. Kong, Phys. Stat. Solidi A27 (1991) 187.

[101] C.H. Kao, Y.S. Shiue, S. R. Sheen and M.K. Wu, Physica C 205 (1993) 186.

[102] G. Xiao, M. J. Cieplak, D. Musser, A. Gavrin, L.L. Chien, J.J. Rhyne and J. A. Gottas, Nature 332 (1988) 238.

[103] F. J. Baca, D. Fisher, R.L.S Emergo, J.Z. Wu, Supercond. Sci. Technol. 20 (2007) 554.

[104] L. Gozzelino, D. Botta, R. Cherubini, A. Chiodoni, R. Gerbaldo, G. Ghigo,F. Laviano, B. Minetti, E. Mezzetti, Eur. Phys. J. B 40 (2004) 3.

[105] J. C. Barbour, E. L. Venturini, and D. S. Ginley, Nucl. Instrum. Methods Phys. Res. B 59-60 (1991) 1395.

[106] A. Lakhani, V. Ganesan, S. Elizabeth, H.I. Bhat, R. Singh, D. Kanjilal, Nucl. Instrum. Methods Phys. Res. B 244 (2006) 120.

[107] A. Dunlop, D. Lesueur, J. Morillo, J. Dural, R. Spohr and J. Vetter, C.R. Acad. Sci Paris 309 (1989) 1277.

[108] E. Paumier, A. Audouard, F. Beuneu, Ch. Dufour, J. Dural, J.P. Girard, A. Hairie, M. Levalois, A. Barbu, A. Dunlop, D. Lesueur and N. Lorenzelli, Philos. Mag. Lett. 67 (1993) 253.

[109] H. Dammak, A. Barbu, A. Dunlop, D. Lesueur and N. Lorenzelli, Phil. Mag. Lett. 67 (1993) 253.

[110] S. Klaumunzer, Ming-domg Hou and G. Schumacher, Phys. Rev. Lett. 57 (1986) 850.

[111] A. Barbu, A. Dunlop, D. Lesueur and R. S. Averback, Europhys. Lett. 15 (1991) 37.

[112] A. Meftah, F. Brisard, J.M. Costantini, E. Dooryhee, M. Hage-Ali, M. Herview, J. P. Stoquert, F. Studer and M. Toulemonde, Phys. Rev. B 49 (1994) 12457.

[113] J.R. Liu, Z.H. Zhang, J. Wu, K. Ma, Y. J. Zhao, N. Yu, P. Hsieh and Wei Kan Chu, Nucl. Instrum. Methods B 62 (1991) 74.

[114] F. Rullier Albenque, A. Legris, S. Bouffard, E. Paumier and P. Lajay, Physica C 175 (1991)111.

[115] A.D. Marwick, G.J. Clark, D.S. Yee, R.B. Laibowitz, G. Coleman and J.J. Cuomo, Phys. Rev. B 39 (1989) 9061.

[116] F. Rullier Albenque, A. Legris, S. Bouffard, E. Paumier and P. Lajay, Physica C 175 (1991)11.

[117] D.S. Fisher, M.P.A. Fisher, D.A. Huse, Phys. Rev. B 43 (1991) 130.

[118] P.C. Hohenberg, B.I. Halperin, Rev. of Mod. Phys. 49 (1977) 435.

[119] E. F. Talantsev, N. M. Strickland, P. Hoefakker, J.A. Xia, N.J. Long, Current Appl. Phys. 8 (2008) 388.

[120] E. Giannini, R. Gladyshevskii, N. Clayton, N. Musolino, V. Garnier, A. Piriou, R. Flukiger, Curr. Appl. Phys. 8 (2008) 115.

[121] L. Civale, Supercond. Sci. Technol. 10 (1997) A11.

[122] N. Hassan,N. A. Khan, J. Appl Physics 104(2008) 103902.

[123] Y. Ishii, J. Shimoyama, Y. Tazaki, T. Nakashima, S. Horii, K. Kishio, Appl. Phys. Lett. 89 (2006) 202514.

[124] M. Irfan, N. Hassan, S.A. Manzoor, B. Shabbir, N. A. Khan, J Appl. Phys. 106 (2009) 113913.

Chapter 2

Experimental Techniques

2.1 INTRODUCTION

This chapter deals with the sample preparation and characterization techniques used to measure different aspects of high temperature superconductivity. Composites bulk of YBCO with $BaSnO_3$ (BSO), Cr_2O_3, $BaTiO_3$-$CoFe_2O_4$ (BTO-CFO) and composite thin film of YBCO with BSO by pulsed laser deposition have been prepared. Ion matter interaction with low energy ions has been discussed with reference to YBCO. Phase formation, surface analysis, elemental analysis and different characterization techniques are mentioned briefly. Measurement of resistivity by DC four-probe set up and characterizations tools include phase formation and surface modification study with the help of X-ray diffraction (XRD), Raman spectroscopy (RAMAN), Energy dispersive X-ray analysis (EDXA), Scanning electron microscopy (SEM) and Field emission scanning electron microscopy (FESEM) have been highlighted in this section.

2.2 METHODOLOGY OF SAMPLE PREPARATION

2.2.1. Preparation of bulk $YBa_2Cu_3O_{7-\delta}$ (YBCO) powder

Superconducting sample $YBa_2Cu_3O_{7-\delta}$ (YBCO) is prepared through solid state reaction route. For the preparation of YBCO, stoichiometric amount of the chemicals Y_2O_3 (99.9% pure), $BaCO_3$ (99.9% pure) and CuO (99.9% pure) were taken with cationic ratio 1:2:3. The weighed chemicals were mixed and ground well with an agate mortar and pestle for about 2-3 hrs till a gray powder of the compound was obtained. The grinded powder was put in an alumina crucible and calcined in a programmable box furnace (Fig. 2.1). First heating was done at 900^0 C for 12 hrs. The furnace was then turned off and the sample was allowed to cool slowly in the furnace. The crucible was removed when it attained room temperature. The black mass was gently dislodged from the crucible to the mortar and reground for 2-3 hrs and then again heated inside the furnace. Repeating the calcinations process four times assured complete removal of CO_2 by the reaction.

$$\tfrac{1}{2}\, Y_2O_3 + 2\, BaCO_3 + 3\, CuO + \tfrac{1}{2}\, O_2 \rightarrow YBa_2Cu_3O_{7-\delta} + 2\, CO_2 \qquad (eq^n\ 2.1)$$

After through grinding, final pellets (10 mm diameter, 2 mm thickness) were made by applying a pressure of 100 Kg/cm^2 by a hydraulic press. After pelletization the samples were again placed in an alumina crucible and sintered at 920^0 C for 12 hrs followed by oxygen annealing at 500^0 C for 8 hrs. Then the samples were allowed to cool slowly (1^0 C/ min) to room temperature. Slow

cooling allows oxygen to be taken up by the samples and provides oxygen stoichiometry close to seven. After cooling the pellets to room temperature, the pellets were preserved in a desiccator to avoid atmospheric moisture and CO_2 degrading the samples.

Fig. 2.1 The programmable furnace (Baisakh) for varying temperatures up to 1700^0 C in our laboratory.

2.2.2. Preparation of $BaSnO_3$ powder

$BaSnO_3$ (BSO) powder has been synthesized by solid state reaction route. Barium carbonate ($BaCO_3$) and Tin oxide (SnO_2) was used as precursors. The powder was ground for 2 hours and then calcined at 1200^0 C for 16 hours to have crystallized $BaSnO_3$ powder [1].

2.2.3. Preparation of $BaTiO_3$ (BTO) powder

$BaCO_3$ and TiO_2 have been used in 1:1 molar ratio as the precursor for the synthesis of $BaTiO_3$ powder. The mixed powder was calcined in temperature of 1200° C for 4 hrs to obtain BTO powder [2].

2.2.4. Preparation of $CoFe_2O_4$ (CFO) powder

$CoFe_2O_4$ is prepared by mixing Co_3O_4 and Fe_2O_3 in 1:1 molar ratio and the mixed oxides were calcined in the temperature range of 1200^0 C for 4 hrs to have CFO powder.

2.2.5. Preparation of $BaTiO_3$-$CoFe_2O_4$ (BTO-CFO) powder

Composite of $BaTiO_3$-$CoFe_2O_4$ was prepared by taking the powder BTO and CFO in the ratio of 70:30 mole percentages respectively. The precursor powder was ground for 2-3 hrs and then calcined in the temperature range of 1200^0 C for 6 hrs to have BTO-CFO powder.

2.2.6. Preparation of YBCO/BSO, YBCO/BTO-CFO and YBCO/Cr_2O_3 composite

The YBCO powder were thoroughly ground and mixed well with BSO, BTO-CFO and Cr_2O_3 powder separately by varying the weight percentage as (1-x) YBCO + x BSO (x = 0.0, 0.1, 0.3, 0.5, 1.0, 2.5, 5.0 wt.%), (1-x) YBCO + x BTO-CFO (x = 0.0, 0.2, 0.4, 0.6 wt.%) and (1-x) YBCO + x Cr_2O_3 (x = 0.0, 2.3, 4.4, 6.1,7.4 wt.%) before the final stage of sintering. The grinded powders were pressed into pellets and sintered at 920° C for 12 hrs followed with cooling at 500° C where the samples were maintained at continuous flow of oxygen for 8 hrs. Then the samples were allowed to cool slowly to room temperature and preserved in a desiccator to avoid atmospheric moisture degrading the samples.

2.2.7. Preparation of $YBa_2(Cu_{1-x}Ti_x)_3O_{7-\delta}$ samples

A series of polycrystalline samples of $YBa_2(Cu_{1-x}Ti_x)_3O_{7-\delta}$ (x = 0.01, 0.02, 0.04, 0.05, 0.07) has been prepared by the standard solid-state reaction method from the appropriate amounts of high-purity powders of constituent oxides and $BaCO_3$ in the required proportions. Calcination of the mixtures was done at 920^0 C for 24 hours. Finally, the samples were pressed into pellets and sintered at 925^0 C for 24 hours, annealed at 450^0 C for 10 hours in oxygen atmosphere for oxygen uptake and cooled to room temperature over a period of 10 hours.

2.2.8 Preparation of YBCO/BSO composite PLD thin film

YBCO powder was prepared by solid state reaction route as discussed above. 1 wt. % BSO powder was mixed well with YBCO, pelletized and sintered at 920° C followed by oxygen annealing at 500° C which served as the target. YBCO/BSO films were deposited on (*l00*) oriented $LaAlO_3$ (LAO) single crystal (1 cm^2) substrates by the pulsed laser deposition (PLD) at IOP, Bhubaneswar (Fig. 2.2). The growth conditions of thin film are summarized below in Table 2.1.

Table 2.1 Growth conditions for PLD film.

Laser	KrF excimer laser (λ= 248 nm)
Target	YBCO + 1wt. % BSO pellet
substrate	(l 00)-oriented $LaAlO_3$ (LAO)
Target substrate distance	5 cm
Repetition frequency	10 Hz
Thickness	~150 nm
Laser energy	220 mJ
Substrate temperature	750 °C
Oxygen pressure	400 mTorr

Fig. 2.2 Pulsed laser deposition set up at IOP, Bhubaneswar (Prof. T. Som's Lab): deposition chamber (left) and excimer laser (right).

2.3. IRRADIATION BY LOW ENERGY IONS

The superconducting thin films of YBCO/BSO composite were subjected to low energy ion irradiation at Inter University Accelerator Centre (IUAC), New Delhi. The low energy ion beam facility at the Inter-University Accelerator Centre provides multiple charged ion beams at a wide range of energies (few keV to MeV) for experiments in atomic, molecular and material sciences.

This is used for material science experiments (including implantation, surface modification, sputtering etc) in a dedicated chamber provided with a multiple sample holder that can be either heated (for high temperature implantation) or cooled to liquid nitrogen temperature. The various types of available low energy ion beams, their range of charge states, energies and beam currents are tabulated below:

Table 2.2 Various types of low energy ion beams

Types of ion	Range of charge states (q)	Range of energy (E)	Range of beam current (eμA)
Oxygen (O)	1+ to 6+	50 keV to 0.9 MeV	0.1 to 100
Argon (Ar)	1+ to 10+	50 keV to 1.5 MeV	0.1 to 15
Xenon (Xe)	1+ to 20+	50 keV to 3.0 MeV	0.1 to 15
Lead (Pb)	1+ to 15+	50 keV to 2.2 MeV	0.1 to 8

2.3.1 Beam Production Techniques

The following techniques are used for the production of a wide variety of beams:

Gas inlet: This is the simplest and most robust way to produce ions. The elements whose ions are required are injected into the ECR source in the form of a gas. This is most suitable for the noble gases and elements like oxygen, nitrogen and hydrogen etc.

Micro-oven: For elements that cannot be obtained in gaseous form, a micro-oven is available. The oven is inserted into the plasma chamber and can be heated up to a 1000^0 C. Volatile compound loaded into the micro-oven and used to produce ions.

Sputtering: A mechanized arrangement to insert a long thin wire (1mm or 0.5 mm thick) of any element may be introduced into the source plasma volume. The high energy electrons can sputter out elements present in the wire, ionize them and produce the required beam.

MIVOC: For metal ions, the technique of metal ions from volatile organic compounds has been indigenously implemented. Organic compounds that have a metal atom and are volatile are sealed into a stainless steel chamber and then allowed to permeate the ECR source volume. This allows us to extract metal ion beams that are difficult to produce by other techniques.

Fig. 2.3 Low energy ion irradiation set-up at IUAC, New Delhi.

The target ladder is a cylindrical stainless steel rod of length 1m with a solid rectangular copper block at one end. The samples are mounted on the four sides of the copper block. The ladder is placed perpendicular to the ion beam path and could be adjusted up and down by linear movement. The ladder is also provided with a provision of 360° rotation fitted within a chamber. Then the ladder has been placed inside the beam line chamber and evacuated using high vacuum pumping system. After the sample is loaded and achieved the desired vacuum the system become ready for irradiation. The samples are scanned by magnetic scanner over an area 1×1 cm^2. The irradiation fluence can be varied by adjusting the time of exposure of the sample for irradiation. The scanning area can be varied as required for the experiments with scanner. The current and energy is controlled through the control room.

2.4. CHARACTERIZATION TECHNIQUES OF THE SAMPLES

The bulk sintered pellets and thin films were characterized by the following techniques.

1. Micro-Raman Spectroscopy
2. Powder X-ray diffraction (XRD)
3. Scanning electron microscopy (SEM)
4. Field emission scanning electron microscopy (FESEM)
5. Fourier transform infrared spectroscopy (FTIR)
6. Four probe DC resistivity measurement at varying temperatures down to 10 K
7. P-E hysteresis loop measurement

The characterization techniques are discussed below:

2.4.1 Micro-Raman Spectroscopy

Micro-Raman spectroscopy is the technique based on inelastic scattering of monochromatic light (laser source) where the frequency of photons changes upon interaction with sample. Photons of the laser light are absorbed by the sample and then re-emitted. Frequency of the re-emitted photons shifted up or down in comparison with original monochromatic frequency. This shift provides information about vibrational, rotational and other low frequency transitions in molecules. Raman spectroscopy can be used to study solid, liquid and gaseous samples.

The Raman Effect exhibits when light impinges upon a molecule and interacts with the electron cloud and the bonds of that molecule. For the spontaneous Raman effect, a photon excites the molecule from the ground state to a virtual energy state. When the molecule emits a photon and returns to the ground state, it returns to a different rotational or vibrational state. The difference in energy between the original state and this new state leads to a shift in the emitted photon's frequency away from the excitation frequency. A change in the molecular polarization potential or amount of deformation of the electron cloud with respect to the vibrational coordinate is required for a molecule to exhibit a Raman effect. The amount of the polarizability change will determine the Raman scattering intensity. The position and intensity of the vibrational bands are characteristic of the molecular motion and consequently the atoms participating in the chemical bond, their confirmation, and their immediate environment (Fig. 2.4) [3].

(i) A molecule with no Raman-active modes absorbs a photon with the frequency υ_0. The excited molecule returns back to the same basic vibrational state and emits light with the same frequency υ_0 as an excitation source. This type of interaction is called an elastic Rayleigh scattering.

(ii) A photon with frequency υ_0 is absorbed by Raman-active molecule which at the time of interaction is in the basic vibrational state. Part of the photon’s energy is transferred to the Raman-active mode with frequency υ_m and the resulting frequency of scattered light is reduced to υ_0-υ_m. This Raman frequency is called Stokes frequency.

(iii) A photon with frequency υ_0 is absorbed by a Raman-active molecule, which at the time of interaction, is already in the excited vibrational state. Excessive energy of excited Raman active mode is released, molecule returns to the basic vibrational state and the resulting frequency of scattered light goes up to $\upsilon_0+\upsilon_m$. This Raman frequency is called Anti-Stokes frequency.

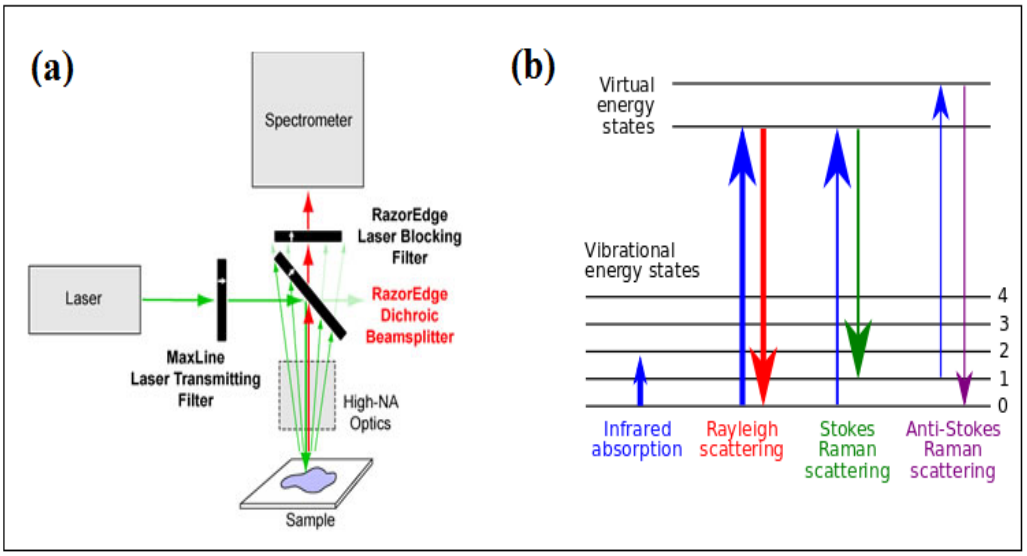

Fig. 2.4 (a) The schematic diagram of Raman experiment (b) Principle of Raman technique [4].

2.4.2 Powder X-ray diffraction (XRD)

Materials are made of atoms. Knowledge of how atoms are arranged into crystal structures and microstructures is the foundation on which we build our understanding of the synthesis, structure and properties of materials. X-ray diffraction (XRD) is a fingerprint characterization of crystalline materials to know the spatial arrangements of atoms in materials and the determination of their structure. Once the material has been identified, XRD may be used to determine its structure i.e. how the atoms pack together in the crystalline state and what the inter-atomic distance and angle etc. XRD technique has the additional advantage that it requires only very little amount of sample and is a non-destructive technique. Here the incident waves must have wavelengths comparable to the spacing between atoms [5].

Diffraction patterns are observed when X-ray of wavelength (λ) interacts with the atomic arrangement of atoms comparable with the inter-planar spacing (d) of crystals, satisfying the Bragg condition [6]

$$2d\ sin\theta = n\lambda \qquad \text{(eq. 2.2)}$$

Where θ is the incident angle (Fig. 2.5)

For cubic crystals with lattice parameter a_0, the inter-planar spacing (d_{hkl}) of planes labeled by Miller indices (hkl) are:

$$d_{hkl} = a_0 / (h^2+k^2+l^2)^{1/2} \qquad \text{(eq. 2.3)}$$

d_{hkl} relation became more complicated when the crystal symmetry is different [6]

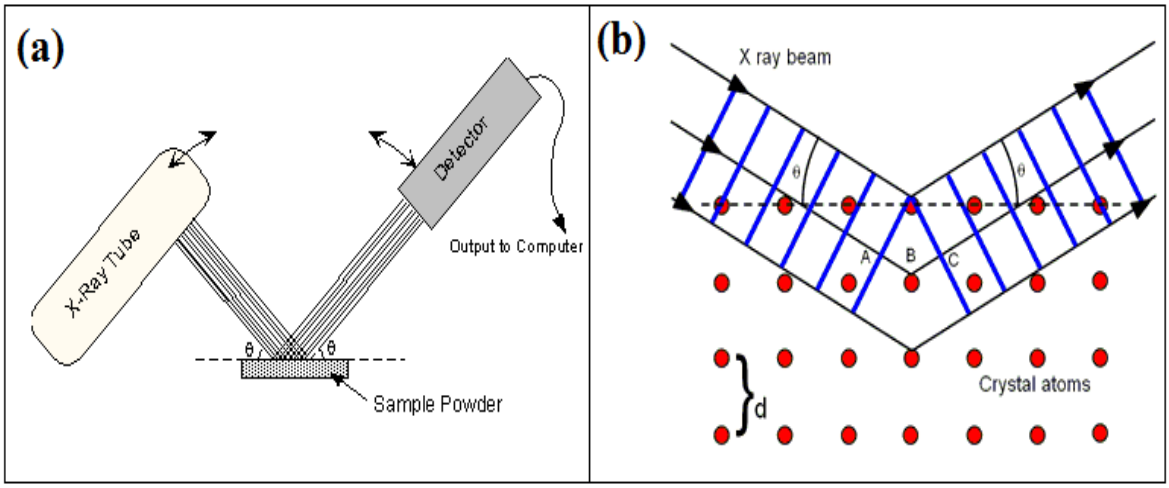

Fig. 2.5 (a) Schematic view of an X-ray powder diffractometer (b) Reflection of X-rays from two planes of atoms in a solid [7].

2.4.3 Scanning electron microscopy (SEM)

The Scanning electron microscope produces a largely magnified image by using electrons instead of light to form an image. A beam of electrons is produced at the top of the microscope by an electron gun. The electron beam follows a vertical path through the microscope, which is held within a vacuum. The beam travels through electromagnetic fields and lenses, which focus the beam down toward the sample. Once the beam hits the sample, electrons and X-rays are ejected from the sample. Detectors collect these X-rays, backscattered electrons, and secondary electrons and convert them into a signal that is sent to a screen similar to a television screen. This produces the final image (Fig. 2.6). All of these advantages, as well as the actual strikingly clear images, make the scanning electron microscope one of the most useful instruments in research today. SEM images give information about the topography, morphology, composition and crystallographic information of the specimen. The shape, size and arrangement of the particles

building up an object that is lying on the surface of the sample or has been exposed by grinding or chemical etching. The elements and compounds the sample is composed of and their relative ratios [8, 9].

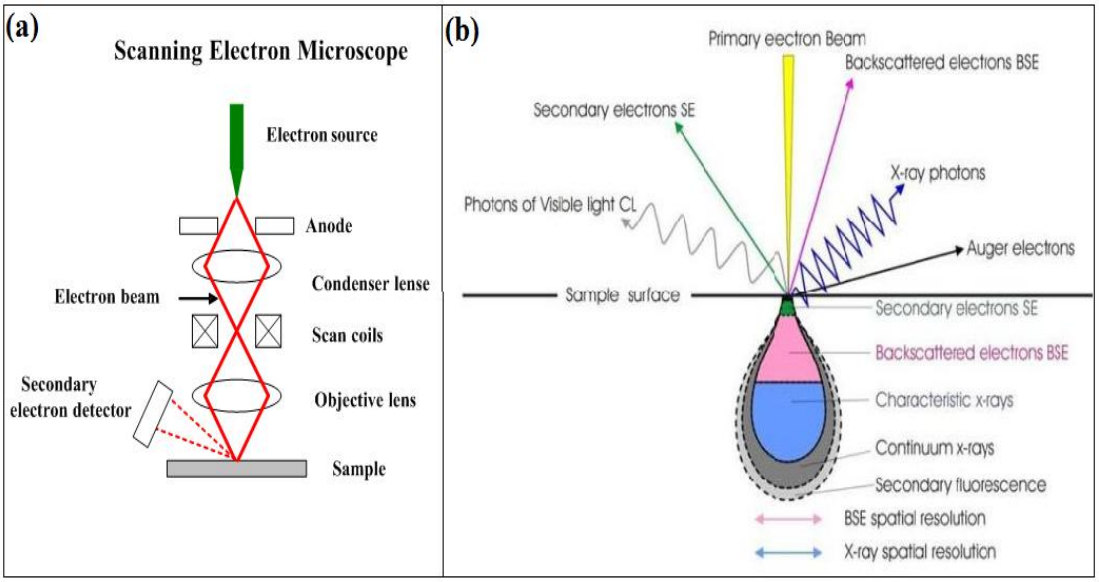

Fig. 2.6 (a) Schematic diagram of SEM setup (b) Electron beam interaction process with the sample [10].

Energy dispersive X-ray (EDX) is an analytical technique used for the elemental analysis or chemical characterization of a sample. The EDX analysis system works as an integrated feature of a scanning electron microscope. During EDX analysis, the specimen is bombarded with an electron beam inside the scanning electron microscope. The impact of the electron beam on the sample produces X-ray that is characteristic of the elements present on the sample. At rest, an atom within the sample contains ground state (unexcited) electrons in discrete energy levels or electron shells bound to the nucleus. The incident beam may excite an electron in an inner shell, ejecting it from the shell while creating an electron hole where the electron was. An electron from an outer higher-energy shell then fills the hole, and the difference in energy between the higher energy shell and the lower energy shell may be released in the form of an X-ray. The number and energy of the X-ray emitted from a specimen can be measured by an energy-dispersive spectrometer. As the energy of the X-rays is characteristic of the difference in energy between the two shells and of the atomic structure of the element from which they were emitted, this allows the elemental composition of the specimen to be measured (Fig. 2.7).

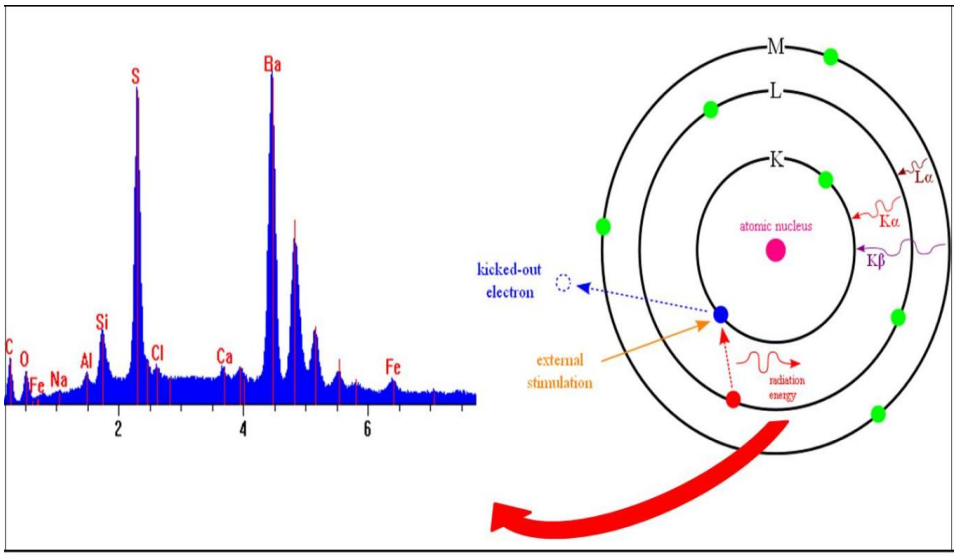

Fig. 2.7 Schematic diagram of EDXA principle [11].

2.4.4 Field emission scanning electron microscopy (FESEM)

Field emission scanning electron microscope works with electrons instead of light. These electrons are liberated by a field emission source. The object is scanned by electrons in a zigzag pattern. FESEM is used to visualize very small topographic details on the surface or entire or fractioned objects. In FESEM electrons are liberated from a field emission source (electron gun) and accelerated in a high electrical field gradient. The electron gun provides a large and stable current in a small beam. Emitter type is the main difference between the SEM and FESEM. In SEM, thermionic emitters use electrical current to heat up a filament. The two most common materials used for filaments are Tungsten and Lanthanum Hexaboride. When the heat is enough to overcome the work function of the filament material, the electrons can escape from the material itself. Thermionic sources have relative low brightness, evaporation of cathode material and thermal drift during operation. Field emission is one way of generating electrons that avoids these problems. A field emission gun (FEG), also called a cold cathode field emitter, and does not heat the filament. The emission is reached by placing the filament in a huge electrical potential gradient. The FEG is usually a wire of Tungsten fashioned into a sharp point. The significance of the small tip radius (~ 100 nm) is that an electric field can be concentrated to an extreme level, becoming so big that the work function of the material is lowered and electrons can leave the cathode. FESEM uses FEG for producing a cleaner image with less electrostatic distortions and

spatial resolution (three or six times better than SEM). Within the high vacuum column these primary electrons are focused and deflected by electronic lenses to produce a narrow scan beam that bombards the object. The vacuum allows electron movement along the column without scattering and helps discharges inside the gun zone. As a result secondary electrons are emitted from each spot on the object. The angle and velocity of these secondary electrons relates to the surface structure of the object. A detector catches the secondary electrons and produces an electronic signal. This signal is amplified and transformed to a video scan-image that can be seen on a monitor or to a digital image that can be saved and processed further.

The followings are the advantages of FESEM:

- Ultra high resolution at low kV
- Quantitative elemental analysis of the bulk material
- Fast elemental mapping and line scan of area of interest
- Topographical, compositional analysis and other information
- Detection of small variations of trace element content
- Digital output
- Oil-free vacuum
- Large specimen capacity
- Rapid sample introduction

2.4.5 Fourier transform infrared spectroscopy (FTIR)

FTIR offers quantitative and qualitative analysis for organic and inorganic samples. It identifies chemical bonds in a molecule by producing an infrared absorption spectrum. It is an effective analytical instrument for detecting functional groups and characterizing covalent bonding information. When a sample exposed to infrared radiation, its molecules absorb radiation of specific wavelengths which causes the change of dipole moment of sample molecules. Consequently, the vibrational energy levels of sample molecules transfer from ground state to excited state.

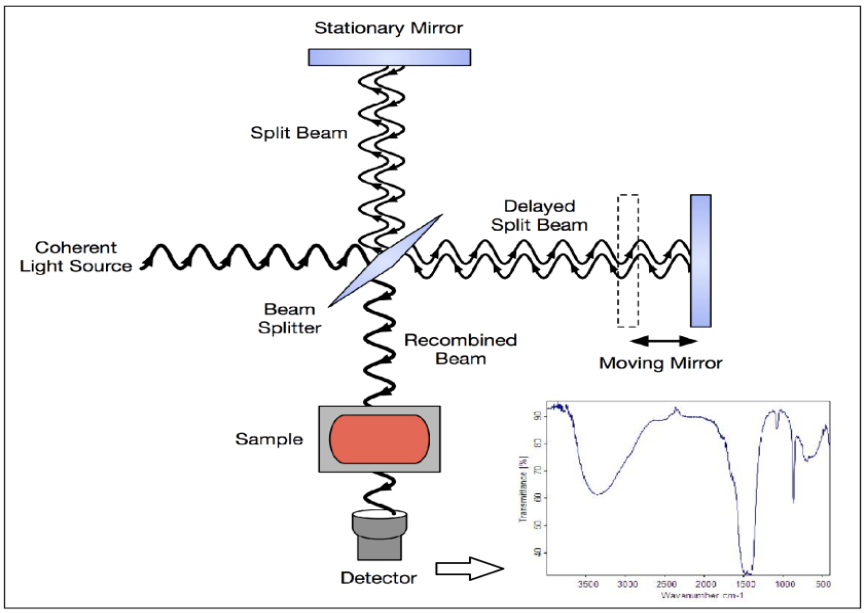

Fig. 2.8 Schematic optical diagram of an FTIR spectrometer [12].

The frequency of the absorption peak is determined by the vibrational energy gap. The number of absorption peaks is related to the number of vibrational freedom of the molecule. The intensity of absorption peaks is related to the change of dipole moment and the possibility of the transition of energy levels. Therefore, by analyzing the infrared spectrum, one can readily obtain abundant structural information of a molecule (Fig. 2.8). Most molecules are infrared active except for several homo-nuclear diatomic molecules such as O_2, N_2 and Cl_2 due to the zero dipole change in the vibration and rotation of these molecules. The common used region for infrared absorption spectroscopy is 4000 ~ 400 cm^{-1} because the absorption radiation of most organic compounds and inorganic ions is within this region.

2.4.6 DC four probe resistivity measurement (R-T measurement)

At a constant temperature, the resistance (R) of a conductor is (i) proportional to its length (ii) inversely proportional to its area of cross-section,

$$R \alpha \frac{L}{A} \qquad \text{or} \qquad R = \rho \frac{L}{A}$$

The constant of proportionality ρ is called resistivity of the material. Resistivity of a material is equal to the resistance offered by a wire of this material of unit length and unit cross-sectional area. The unit of resistance is ohm (Ω) and unit of resistivity is ohm.meter (Ω.m). Two or four

probe methods can be used for resistivity measurement depending on the type of probing material. Two probe method is sufficient to measure the resistivity of highly resistive materials such as multiferroic, semiconducting materials. However, four probe method is more accurate for measurement of resistance of superconductors as their resistance vanishes beyond certain critical temperature.

Drawbacks of two probe method:

(i) The major problem in such method is error due to contact resistance of measuring leads.

(ii) This method cannot be used for materials having random shapes.

(iii) For some type of materials soldering the test leads would be difficult.

(iv) In case of semiconductors, the heating of samples due to soldering results in injection of impurities into the materials, thereby affecting the intrinsic electrical resistivity.

To overcome first two problems, a collinear equidistant four-probe method is used (Fig. 2.9).

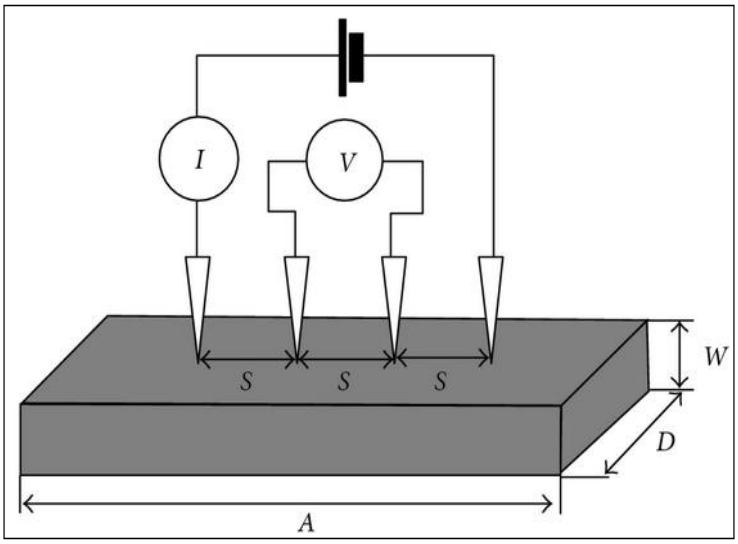

Fig. 2.9 Schematic diagrams of four probe method [13].

This method provides the measurement of the resistivity of the specimen having wide variety of shapes but with uniform cross-section. The soldering contacts are replaced by pressure contacts to eliminate the last two problems discussed above. The sintered pellets were cut into rectangular slabs with dimension $5\times3\times2$ mm^3 by pellet cutter which serves as the specimens for four probe

measurement. The following units involved in the characterization of superconducting samples for four probe resistivity measurements (Fig. 2.10).

- Closed cycle He refrigerator

A closed cycle He refrigerator (Janis Model) is used for cooling the sample chamber from room temperature to 10 K. A two stage, oil sealed mechanical vacuum pump was employed for creating vacuum in the shroud. Using the principle of Gifford-McMahon thermodynamic cycle the helium gas is compressed and expanded [14]. A heater and silicon diode sensor are fitted closer to the sample holder that precisely controls the sample temperature.

- Temperature controller

Temperature of the cold head is controlled with a digital temperature controller (Lakeshore model-332).This is a microprocessor based indicator system designed to interface with cryogenic refrigeration systems. The controller measures and displays the process temperature by a silicon diode temperature sensor. It controls power to a heater within the cold head, in order to maintain process temperature at a fixed set point value. Both the heater and the temperature sensor are located close to sample holder in the cold head. The temperature can be controlled from 10 K to 300 K [15].

- Current source

Keithley 6221 AC/ DC current source is used to supply current to the experimental samples. It provides high resolution, low noise and fast output over a wide range of compliance settings [16]. It provides AC currents from 1pA to 100 mA, with 10 MHz output update rate.

- Digital Nanovoltmeter

Voltage developed in the samples due to application of current is measured by a Digital Nanovoltmeter (Keithley, Model 2182A). It performs resistance measurements with low noise, low voltage measurements, less power dissipation with sensitivity down to 10 nV [17].

- Data acquisition

All the components of the R-T setup i.e. constant current source, nanovoltmeter and the temperature controller were interfaced with GPIB IEEE-488 to a computer for automatic

resistivity data measurement with varying temperature in a lab view programme. Fig.2.10 shows resistivity measurement arrangement in our laboratory without magnetic field.

Fig. 2.10 DC Four probe Resistivity measurement set up at our laboratory.

2.4.7 P-E hysteresis loop measurement

The ferroelectric (Polarization-Electric field) hysteresis is a defining property of ferroelectric materials. It is a very intensive study for ferroelectric materials, due to the potential applications of ferroelectric thin films in nonvolatile memories. A P-E loop for a device is a plot of the charge or polarization (P) developed, against the field applied to that device (E) at a given frequency. In ferroelectric memories the information is stored as positive or negative remanent polarization state. The most widely studied characteristics of ferroelectric hysteresis were those of interest for this particular application: the value of the switchable polarization (the difference between the positive and negative remanent polarization, P_R- (-P_R)), dependence of the coercive field E_c on sample thickness, decrease of remanent or switchable polarization with number of switching cycles, polarization imprint, endurance, and retention.

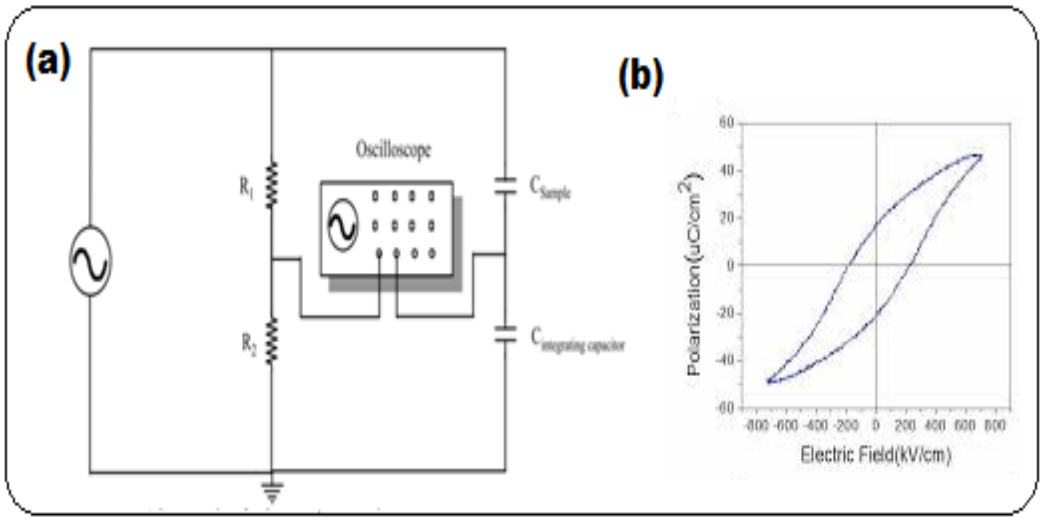

Fig. 2.11 Schematic diagram of a Sawyer Tower circuit for P-E loop measurement [18, 19].

In P-E loop measurement, the field applied across the sample is attenuated by a resistive divider, and the current is integrated into charge by virtue of a large capacitor in series with the sample. Both these voltages are then fed into the X and Y axes of an oscilloscope to generate the P-E loop (Fig. 2.11). The applied voltage was usually a sinusoid at mains frequency as this was the simplest method to generate the required voltage and current [18].

2.5 References

[1] M.G. Smith, J.B. Goodenough, A. Manthiram, R.D. Taylor, W. Peng, C.W. Kimball, J. Solid State Chem. 98 (1992) 181.

[2] U. Manzoor and D.K Kim, J. Mater.Sci.Technol. 23 (2007) 655.

[3] P. P Kalantri, R. R. Somani and D. T Makhija, Der Chemica Sinica 1 (1) (2010) 1.

[4] http://en.wikipedia.org/wiki/Raman_spectroscopy.

[5] B. Fultz, J. Howe, Transmission Electron Microscopy and Diffractometry of Materials, Graduate Texts in Physics, Springer-Verlag Berlin Heidelberg (2013).

[6] B. D Cullity, "Elements of X-ray Diffraction", 2nd Edition, Addison-Wesley Publishing Company, Inc. (1978).

[7] http://www.tulane.edu.

[8] D. Brandon, W.D. Kaplan, Microstructural characterization of materials. 2nd Edition, John Wiley & Sons (2008).

[9] P. J. Goodhew, J. Humphreys, R. Beanland, Electron microscopy and Analysis, (3rdEdition) Taylor & Francis (2001).

[10] http://www.substech.com & http://www.gla.ac.uk.

[11] http://epimtg.blogspot.in/2012/12/energydispersive-x-ray-spectroscopy-edx.html.

[12] http://en.wikipedia.org/wiki/Fourier_transform_infrared_spectroscopy.

[13] http://www.hindawi.com/journals/jnm/2011/606714/fig2/.

[14] www.janis.com.

[15] www.lakeshore.com.

[16] www.keithley.com.

[17] www.keithley.com.

[18] C. B Sawyer, C. H Tower, Phys Rev 35 (1930) 269.

[19] http://www.intechopen.com.

Chapter 3

Superconducting Order Parameter fluctuation in Cuprates

3.1 GENERAL PROPERTIES OF GRANULAR SUPERCONDUCTORS

The inherent granular nature of YBCO has drawn attention for the intrinsic properties due to the grains and the extrinsic properties due to grain boundaries which leads strong structural disorder [1-3] at the microscopic and mesoscopic levels respectively. A superconductor can be assumed as an array of superconducting granules coupled via electron tunnelling. The superconducting properties of an array are determined by the properties of the granules of which it is formed [1]. Diffusive scattering by grain boundaries is similar to the scattering by potential impurities in the bulk [1]. An array with sufficiently strongly coupled grains should be able to maintain the superconducting coherence in the whole sample because the coupling reduces the phase fluctuations. In the limit of weak coupling the strong Coulomb interaction should lead to the Coulomb blockade of the Cooper pairs [4-6]. Coulomb blockade can be summarized as follows; generally a polycrystalline sample consists of arrays of inter-connected granules rather than a single grain coupled to a bulk metal. In the strong intergranular coupling regime, tunnelling conductance g is very large i.e. $g >> 1$. So that electrons propagate easily through the granular sample and the Coulomb interaction is screened. But in the low coupling regime the tunnelling conductance $g << 1$, the charge on each grain becomes quantized and electrons cannot propagate easily through the granular sample. This is called Coulomb blockade behaviour. Josephson coupling tends to lock the phases of neighbouring grains and delocalize the Cooper pairs, while the Coulomb interaction tends to localize the Cooper pairs and thus enhance the quantum phase fluctuations. In the strong coupling regime, the granular system resembles the homogeneously disordered system. Within the accuracy of the mean-field BCS theory the thermodynamics of such a system is essentially the same as that of a pure bulk electron system. This means that the granular sample turns to the superconducting state immediately after the superconducting gap appears locally in each grain. The insulating state where superconductivity exists locally i.e being absent in the whole sample, may be obtained only beyond the BCS approximation. Corrections to the BCS theory may come from the Coulomb interaction and superconducting fluctuations. But they are expected to be small in the limit $g >> 1$. This result allows us to come to the conclusion that at $g >> 1$ the BCS theory is a good starting point to describe the granular system [1]. If the coupling between the grains is sufficiently strong and the system is well conducting, role of irregularities are not very important. Irregularities become crucial in the limit of low coupling where the system is an insulator. One of the most important energy parameters of the granular system is the single-grain Coulomb charging energy (E_c). This

energy is equal to the change in energy of the grain during the process of adding or removing one electron. It plays a crucial role in the transport properties in the insulating regime when electrons are localized in the grains, such that the charge of each grain is quantized [1].

3.2 NORMAL STATE AND PARACOHERENT RESISTIVITY

Generally in the normal-state electrical conduction of granular samples, current path frustration and meandering of current may occur due to two mechanisms. One is associated with the orientational disorder of anisotropic grains [7]. It depends on the degree of texturization, and has its origin in the extreme anisotropy of the copper oxides, the in-plane resistivity ρ_{ab} being orders of magnitude less than the out of plane resistivity ρ_c [8]. We assume that due to the extreme conduction anisotropy, current is blocked along the pathways with misaligned grains and current percolates through the sample along unobstructed paths, which results in a cross section reduction and path lengthening which increases the resistivity by a multiplicative factor, denoted as 1/f ($0 < f \leq 1$) [9]. Another source of resistivity enhancement comes from structural defects of the grains (i.e. pores, isolating boundaries, micro cracks etc.) denoted as $1/\alpha_{str}$ ($0 < \alpha_{str} \leq 1$). Besides the percolative process, a contribution to resistivity coming from the inter-grain barriers (ρ_{wl}) is to be added. So the observed normal state resistivity can be written as,

$$\rho_n = (1/\alpha_n)(\rho_{ab}+\rho_{wl}) \qquad (eq^n\ 3.1)$$

where α_n is a shorthand for

$$\alpha_n = f \,.\, \alpha_{str} \qquad (eq^n\ 3.2)$$

and it may be referred to as the normal-state percolative factor. The normal-state resistivity of polycrystalline HTSC is linear with temperature. This linearity of ρ_n enables for the determination of the two sample parameters α_n and ρ_{wl}. Taking temperature derivatives of the equation (3.1) and assuming ρ_{wl} constant we can get [10, 11]

$$\alpha_n = \rho'_{ab} / \rho'_n \qquad (eq^n\ 3.3)$$

where the prime stand for temperature derivatives. Similarly from Eq^{n}s. (3.1) and (3.3)

$$\rho_{wl} = \rho'_{ab} / \rho'_n \, \rho_n(0) = \alpha_n \, \rho_n(0) \qquad (eq^n\ 3.4)$$

All the parameters are shown in Fig. 3.1 for typical granular superconductor (YBCO). Based on single crystal measurements ρ_{ab} is assumed [12] to vary linearly with temperature (ρ'_{ab} = 0.5 $\mu\Omega.cm.K^{-1}$) with a negligible zero-temperature intercept. For typical polycrystalline Y-based HTSC α_n is in the range 0.2-0.05 [13]. The main difference between percolation in the normal state and in paracoherent state is that in the latter the orientational disorder is irrelevant as the grain resistivity becomes vanishingly small both in the ab plane and the c direction, resulting in the loss of anisotropy. Once bulk grains go superconducting (but the intergrain junctions remain normal) nothing hinders conduction along that path. Only the structural quality factor α_{str} and the intergrain resistivity ρ_{wl} enter the paracoherent resistivity ρ_p , [14]

$$\rho_p = (1/\alpha_{str})\,\rho_{wl} \qquad (eq^n\ 3.5)$$

From eq (3.2) and (3.4)

$$\rho_p = f\,\rho_n(0) \qquad (eq^n\ 3.6)$$

The relation should be $\rho_n(0) > \rho_p > \rho_{wl}$. For YBCO, ρ_p should be equal to approximately one-third of the normal-state resistivity extrapolated to zero temperature. The transition of the electrical resistance offered by polycrystalline samples is a two-stage process (Fig 3.1) [15-17]. As the temperature decreases, it is first observed a pairing transition and then a coherence transition. At the pairing transition, the superconductivity stabilizes in homogeneous regions within the grains at a temperature which virtually coincides with the critical temperature (T_c) of the bulk sintered. The resistive transition exhibits two different regimes. The first region is characterized by the normal state that shows a metallic behaviour (above $2T_c$ i.e $d\rho/dT > 0$). The normal state resistivity follows Anderson and Zou relation $\rho_n(T) = A+BT$, where $\rho_n(T)$ is calculated by using the values of A and B parameters, which are obtained from the linear fitting of resistivity in the temperature range $2T_c$ to 300 K and extrapolated to 0 K gives resistivity slope ($d\rho/dT$) and residual resistivity ρ_0 respectively.

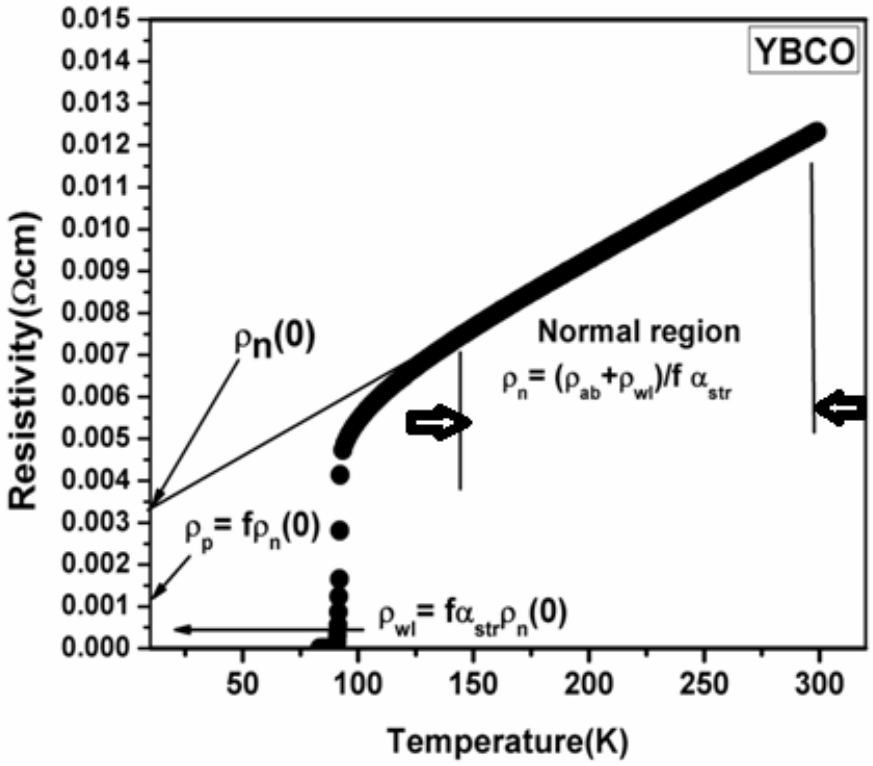

Fig.3.1 Schematic figure showing typical resistivity vs temperature curve for a granular superconductor (YBCO). $\rho_n(0)$ is the extrapolation to zero temperature of the normal-state resistivity ρ_n, ρ_p is the resistivity of the paracoherent state, ρ_{wl} is the average intergrain resistivity ρ_{ab} is the intragrain in-plane resistivity. The other two relevant parameters are the structural factor α_{str} accounting for porosity, microcracks etc. and the anisotropy factor f arising from the anisotropy and misalignment of grains (α_{str}, f <1).

The second region is characterized by the contribution of Cooper pairs fluctuation to the conductivity below T_c, where $\rho(T)$ is deviated from linearity. This is mainly due to the increasing rate of Cooper pair formation on decreasing the temperature. The wave function Ψ (r) describing a superconducting state is also called the order parameter, which is characterized by an amplitude and a phase. Cuprates and most unconventional superconductors have two superconducting order parameters i.e. the pairing order parameter and phase-coherence order parameter [18]. Conventional superconductors have only one order parameter i.e. the pairing one. Because the phase coherence in conventional superconductors is established due to the overlap of Cooper pair wave functions, the process is not governed by an order parameter. In cuprates, the phase coherence is not mediated by the overlap of Cooper pair wave functions. Hence, superconducting cuprates have two distinct order parameters. Phonons are responsible for pairing and spin fluctuations mediate the phase coherence. The pairing order parameter (Δ_p) in cuprates is internal while the phase coherence order parameter (Δ_c) is external. According to Gorkov, in a superconductor the amplitude of pairing order parameter is proportional to the energy gap in electronic excitation spectrum,

arising at the Fermi surface. In conventional superconductors, the symmetry of order parameter, thus the energy gap is isotropic or slightly anisotropic s-wave [18].

According to Ginzburg-Landau (GL) [19] theory of second order phase transition, T_c is defined as the temperature at which the coefficient 'α' changes its sign in the leading term of the free energy expansion:

$$F = F_0 + \alpha |\Psi|^2 + ½ \beta |\Psi|^4 + \ldots\ldots\ldots \quad (eq^n\ 3.7)$$

Above the transition the free energy is raised by an amount KT_c. Hence, the thermal fluctuations would thus raise the order parameter Ψ from zero to a finite value proportional to $e^{-F/KTc}$. The Ginzburg-Landau free-energy F varies as a function of the order parameter as shown in Fig. 3.2(a). The appearance of a minimum at non-zero of |Ψ| is due to the presence of a third-order term in this parameter in the free energy [20]. This leads to the existence of fluctuation induced superconductivity effects above T_c. Hence the free energy is given by,

$$F = \alpha |\delta\Psi|^2 + 1/2\ \beta |\delta\Psi|^4 \quad (eq^n\ 3.8)$$

Neglecting higher order terms in equation (3.8) for the fluctuation amplitude close to minimum of the free energy it modifies to,

$$|\delta\Psi|^2 \sim KT/\alpha = KT/\alpha_0\ (t\text{-}1) \quad (eq^n\ 3.9)$$

Since Ψ_0 above T_c is zero, all the superconducting effects including excess conductivity arise from fluctuations δΨ. The square of the order parameter amplitude $|\delta\Psi|^2$ in equation (3.9) diverges as $(T\text{-}Tc)^{-1}$. Below T_c, the expression for minimum free energy is,

$$F_0 = -\alpha^2/2\beta = \alpha_0^2\ (t\text{-}1)^2/2\beta \quad (eq^n\ 3.10)$$

This gives a non-zero value of the order parameter as,

$$|\Psi|^2 = -\alpha/\beta = \alpha_0(t\text{-}1)/\beta \quad (eq^n\ 3.11)$$

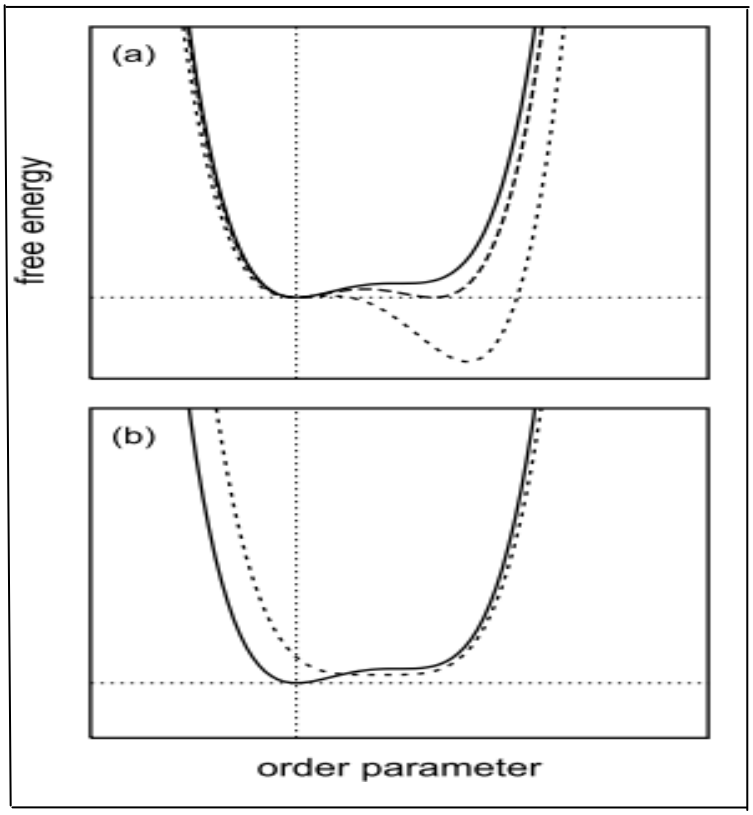

Fig. 3.2 (a) Schematic plot of a Ginzburg-Landau free energy with a cubic term in the order parameter yielding a first-order transition. (b) Free energy with the cubic term at the point where the second minimum starts to appear (full line) and without the cubic term at the critical temperature (dashed line). The latter is displaced from its central position to help visualizing the similarity between the two curves in the region of positive order parameter [20].

3.3 EXCESS CONDUCTIVITY

Thermal fluctuations create Cooper pairs in superconductors above T_c from a temperature around $2T_c$ and the number of Cooper pairs increases rapidly at the expense of the normal electron density which gives rise to a region of excess conductivity or paraconductivity. The analysis of fluctuation induced electrical conductivity leads to three distinct contributions named the Aslamazov-Larkin (AL), the Maki-Thompson (MT), and density of states (DOS) terms. In the first one, the formation of Cooper pair leads to a parallel superconducting channel in the normal phase; the second takes into account the coherent scattering of impurities of the interacting electrons; finally, the third one is due to the rearrangement of the states close to the Fermi energy since electrons involved in pair transport are no longer available for single particle transport. Both the AL and MT terms lead to an enhancement of the conductivity whereas the DOS correction is of opposite sign [21]. The weak-localization (WL) correction is of a purely quantum origin. It stems from the quantum interference of

electrons moving along self-intersecting trajectories and is proportional to the return probability of an electron diffusing in a disordered medium. In the absence of an external magnetic field, the total conductivity above T_{c0}, can be expressed in a combination of three terms as follows,

$$\sigma = \sigma_n + \sigma_{AL} + \sigma_{MT} \qquad (eq^n\ 3.12)$$

The above equation states that, above T_{c0}, the conductivity is enhanced above the normal state conductivity (σ_n) by the fluctuation conductivity of both the Aslamzov-Larkin (AL) term (σ_{AL}) and the Maki-Thompson term (σ_{MT}). The MT term has been usually ignored in the analysis of various zero-field fluctuation conductivity measurements, because of the general belief that the intrinsic large inelastic scattering rates in these materials would reduce significantly the contribution of the MT term to the fluctuation conductivity. Also as the ceramic HTSC are in the dirty superconductor limit, the MT contribution is probably negligible in zero-applied magnetic field [22-24]. Since it has been well known that YBCO has a quasi two-dimensional nature as well as the characteristics of dimensional crossover as a function of temperature, AL model is best to analyze the excess conductivity. The density of states at the Fermi energy contribution introduced by Tewordt and coworkers [25-28] by using a quasi two-dimensional tight binding model is better adapted to copper-oxide HTSC. But this may introduce variations in the excess conductivity amplitude 'A'. But all these effects are being taken directly into account in the approximation for normal state resistivity (ρ_n). Excess conductivity in HTSC is a consequence of second order phase transition. Explanation for the enhancement in conductivity in the superconducting order parameter fluctuations (SCOPF) region has been given by Aslamazov and Larkin [29] and Lawrence-Doniach [30].

According to AL theory the excess-conductivity ($\Delta\sigma$) above T_c generated by the thermodynamic fluctuations diverges as a power-law given by

$$\Delta\sigma = A\varepsilon^{-\lambda} \qquad (eq^n\ 3.13)$$

$\Delta\sigma$ is defined by

$$\Delta\sigma = (1/\rho - 1/\rho_R) = \sigma\,(T) - \sigma_R\,(T) \qquad (eq^n\ 3.14)$$

where σ (T) is the measured conductivity and σ_R (T) is the extrapolated conductivity under the assumption of a linear behavior of temperature dependent resistivity. The reduced temperature $\varepsilon = (T-T_c)/T_c$, is defined with respect to the mean field critical temperature T_c. λ is the

Gaussian critical exponent depending on the dimensionality of the HTSC system. The dimensionality D of the fluctuation system is related through the expression,

$\lambda = 2\text{-}D/2.$ (eq^n 3.15)

The effective value of the critical exponent for 3D and 2D are λ=0.5 and λ=1 respectively [31]. A is a temperature-dependent parameter and its values for 3D and 2D are $A=e^2/32\hbar\xi(0)$ and $e^2/16\hbar d$ respectively. 'ξ (0)' is the zero-temperature coherence length or GL correlation length and 'd' is the effective separation of CuO_2 layers. These relations are based on GL theory and are valid only for the mean field temperature region ($1.01T_c$ to $1.1T_c$). According to this approach, the excess conductivity in one, two and three dimensions are given by the formulae,

$\Delta\sigma\ (1D) = [(\pi e^2\xi\ (0))/16\hbar s]\varepsilon^{-3/2}$ (eq^n 3.16)

$\Delta\sigma\ (2D) = [e^2\ /16\hbar d]\varepsilon^{-1}$ (eq^n 3.17)

$\Delta\sigma\ (3D) = [e^2/32\hbar\xi(0)]\varepsilon^{-1/2}$ (eq^n 3.18)

2D to 3D cross over is mainly found above the critical temperature at a particular temperature T_{LD} which is different for different samples [32-34]. However, it is reported that there is a temperature regime where the superconductor is neither 2D nor 3D and the extent of the regime is controlled by the ratio of the Josephson coupling. Lawrence and Doniac (LD) [30] introduced the concept of interlayer coupling in the vicinity of the critical temperature via Josephson coupling J and in LD model, $\Delta\sigma$ is expressed as,

$\Delta\sigma\ (T)_{LD} = e^2/16\hbar d\varepsilon\{1+(2\xi(0)/d)^2\}^{-1/2}$ (eq^n 3.19)

At temperature close to T_c, $2\xi(0)/d >>1$ and $\Delta\sigma(T)$ diverges as $\varepsilon^{-1/2}$ which corresponds to 3D behavior whereas at $T >> T_c$, $2\xi\ (0)\ /d <<1$ and $\Delta\sigma\ (T)$ diverges as ε^{-1} which corresponds to 2D behavior. This expression predicts a cross over from 2D to 3D behavior of the order parameter fluctuations at temperatures T_{LD} on decreasing temperature of the superconductors.

$T_{LD} = T_c\{1+[2\xi c(0)/d]^2\}$ (eq^n 3.20)

Equation (3.20) reduces to the AL equation with the approximations $\xi\ (\varepsilon) \ll d$ *and* $\xi(\varepsilon) \gg d$ in 2D and 3D region, respectively.

Figure 3.3 displays the logarithmic plot of excess conductivity as a function of reduced temperature (ε). Different regions of the plot are linearly fitted and the exponent values are

determined from the slopes. The plot reveals three distinct regimes, mean-field region or the Gaussian fluctuations, critical fluctuations and short wave fluctuation region. The different crossover temperatures are marked as T_{LD} (Lawrence and Doniach temperature), T_G (Ginzburg temperature) and T_{SW} (short wave fluctuation temperature).

3.3.1 Gaussian Fluctuations

The Gaussian fluctuation region is marked between the temperature T_G and T_{SW}. The first exponent of the Gaussian region lies at log ε (-0.6 ≥ log ε ≥ -1) and its value is 1. It indicates that the order parameter dimensionality (OPD) is two-dimensional (2D). The second exponent lies at log ε (-1 ≥ log ε ≥ -2) and its value is 0.5, which signifies that the OPD is three-dimensional (3D). The temperature at which dimensionality fluctuation occurs from 3D to 2D is denoted by the T_{LD}. T_{LD} value is higher than the T_c value. It signifies that the thermodynamically activated Cooper pairs are generated within the grain at comparatively higher temperatures, but due to the intra-granular disturbances the mean field critical temperature comes down to lower value. When the temperature is diminished near T_c, first superconductivity is established in the CuO_2 planes, as a 2D regime, and crosses up to a well defined 3D regime [35].

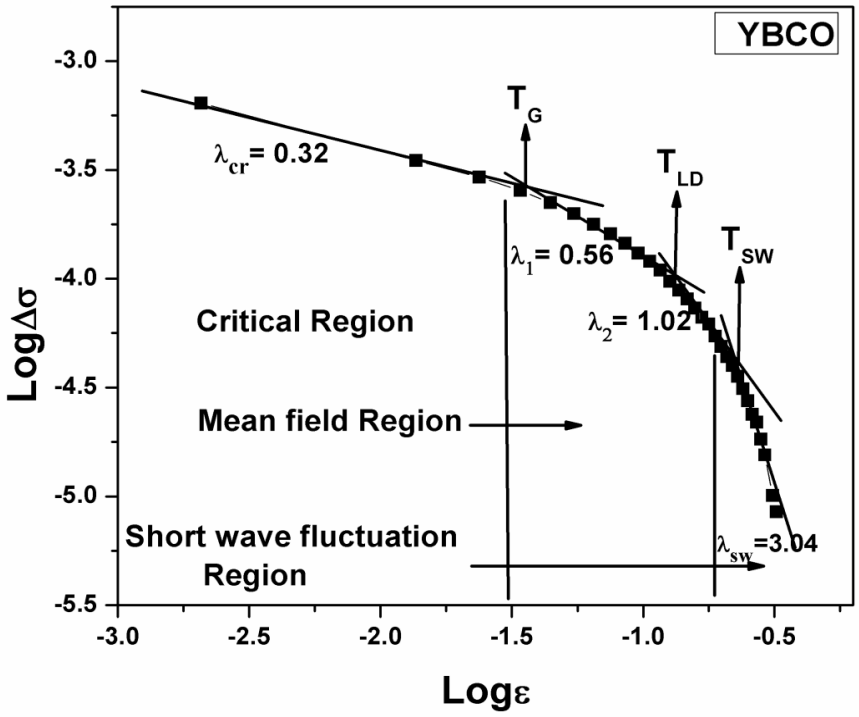

Fig. 3.3 log-log plot of excess conductivity $1/\rho - 1/\rho_R$ as a function of reduced temperature $\epsilon = (T-T_c)/T_c$.

3.3.2 Critical Fluctuations

The critical fluctuation region is marked below the temperature T_G where rapid creation and annihilation of Cooper pairs occurs. Josephson coupling occurs between the superconducting grains inside a superconductor. In the absence of magnetic field, their interaction is two-dimensional. The CuO_2 planes are responsible for their dimensionality and their anisotropic properties. The critical exponent of excess conductivity is obtained from Drude formula as [36-40]

$$\lambda_{cr} = \nu (2\text{-}D\text{-} \eta + z) \qquad (eq^n\ 3.21)$$

where z is the dynamical exponent, η is the exponent of the order parameter correlation function, D is the dimensionality of the fluctuations and ν is the critical exponent for the coherence length. According to renormalization group calculations, $\nu = 0.67$ and $\eta = 0.03$ are expected and $z = 0.32$ being predicted by the theory of dynamical critical scaling [41]. Using these values with D=3 yields $\lambda^{(1)}_{cr} = 0.33$. This is followed by a new regime characterized by the exponent $\lambda^{(2)}_{cr} = 0.17$. This regime has a width of at most 0.1 K which is absent for fields above $\mu_0 H$ = 5mT. This scalling behavior called as 3D-XY-E was first observed in polycrystalline and single crystal YBCO [42- 43,15] and also in $Bi_2Sr_2CaCu_2O_8$ [44].This new scaling is associated with a weak first-order transition. The critical fluctuation and 3D fluctuation regions intersect at temperature $T_{G.}$

3.3.3 1D fluctuations

The appearance of the 1D fluctuation conductivity suggests the existence of 1D conductivity channels, which may represent the CuO_x contribution to the conduction in the RE-123 superconductors. The 1D fluctuation conductivity in the cuprate superconductors would have a significant effect on our understanding of the superconducting process in these materials. The value of the conductivity exponent (λ) for the 1D region fluctuations is 1.5.

3.3.4 Shortwave fluctuations

Above the crossover temperature $T_{SW,}$ the region is called shortwave fluctuation region where GL theory breaks down. The GL theory breaks down for higher values of ε, because it is no longer remains a small parameter and short-wave fluctuations play a dominant role [19]. In this temperature region for $\varepsilon \geq 0.1$, the thermal fluctuations may be deeply affected by the short wavelength fluctuation effects that appear when their characteristic wavelength becomes

of the order of the superconducting coherence length amplitude. In this region $\Delta\sigma$ is theoretically predicted to be falling sharply as ε^{-3}. The cross over temperature from 2D to short wave fluctuations is denoted as $T_{2D\text{-}SW}$. Temperature dependence of paraconductivity data in YBCO in a temperature range above the mean field region is quantitatively analyzed by introducing a short-wavelength cutoff into the Gaussian fluctuation spectrum. This implies that the 3D short-wavelength Gaussian fluctuation dominates in YBCO and suggests a rapid attenuation of these fluctuations with decreasing wavelength in short-coherence length systems as compared to the case of the conventional GL theory [45].

3.4 References

[1] I. S. Beloborodov, A. V. Lopatin, V. M. Vinokur and K. B. Efetov, Reviews of Modern Phys. 79 (2007) 469.

[2] M. Tinkham, Phys. Rev. Lett. 61(1988) 1658.

[3] A. Mohanta, D. Behera, Physica B : Condensed Matter 406 (2011) 877.

[4] B. Abeles, Phys. Rev. B 15 (1977) 2828.

[5] P.W. Anderson , Lectures on the Many-Body Problems Academic, New York 2 (1964) 113.

[6] E. Afsaneh, H. Yavari, Solid State Commun. 152 (2012) 1933.

[7] J.W. Ekin, A.I. Braginski, A.J. Panson, M.A. Janocko, D.W. Capone, N.J. Zaluzec, B. Flandermeyer, O. F. de Lima, M. Hong, J. Kwo, S. H. Liou, Appl. Phys. 62 (1987) 4821.

[8] T.A. Friedmann, M.W. Rabin, J. Giapintzakis, J. P. Rice, D. M. Ginsberg , Phys. Rev. B 42 (1990) 6217.

[9] J. Halbritter, Int. J. Mod. Phys. B 3 (1989) 719.

[10] S.S. Bungre, R. Meisels, Z. X. Shen, A. D. Caplin, Nature (London) 341 (1989) 725.

[11] E. Babic, M. Prester, Z. Marohnic, T. Car, N. Biskup, S.A. Siddiqui, Solid State Commun. 72 (1989) 753.

[12] B. Batlogg, Physics of High-Temperature Superconductors, Springer Series in Solid-State Sciences 106 (1992) 219.

[13] A. Diaz, J. Maza, F. Vidal, Physical Review B 55 (1997) 1209.

[14] M. Sahoo and D. Behera, J Material Sci Eng 1 (2012) 1000115.

[15] P. Pureur, R. Menegotto Costa, P. Rodrigues Jr, J. Schaf , J. V. Kunzler, Phys. Rev. B. 47 (1993) 11420.

[16] A. A. Khurram, N.A. Khan, M. Mumtaz, Physica C 469 (2009) 279.

[17] A. R. Jurelo, J. V. Kunzler, J. Schaf, P. Pureur, J. Rosenblatt, Phys. Rev. B. 56 (1997) 14815.

[18] A. Mourachkine , Fundamental Theories of Physics 125 (2002) 207.

[19] V.L. Ginzberg and L.D. Landau, Zh. Eksperimi, Teor Fiz. 20 (1950) 1064.

[20] Rosangela Menegotto Costa, Paulo Pureur, Miguel Gusma, Sadok Senoussi, K. Behnia, Solid State Communications 113 (2000) 23.

[21] C. Biagini, R. Ferone, Rosario Fazio, F. W. J. Hekking, and V. Tognetti, Phys. Rev. B 72 (2005) 134510.

[22] S. Hikami, A.I. Larkin, Mod. Phys. Lett. B 2 (1988) 693.

[23] A.G Aronov, S. Hikami, A.I Larkin, Phys. Rev. Lett. 62 (1989) 965.

[24] K. Maki, R.S Thomson, Phys. Rev. B 39 (1989) 2767.

[25] L. Tewordt, Phys. Rev. Lett. 83 (1999) 1007.

[26] L.Tewordt and T. Dahm, Phys. Rev. B 63 (2001) 092505.

[27] L. Tewordt and D. Fay, Phys. Rev. B 64 (2001) 024528.

[28] L. Tewordt and D. Fay, Phys. Rev. B 65 (2002) 104510.

[29] L.G. Aslamazov and A.I. Larkin, Fiz. Tverd.Tela 10 (1968) 1104 (Sov. Phys. Sol. St. 10 (1968) 875.

[30] J. Lawrence and S. Doniach, Proc. of 12th Conf. on Low-temp. Phys. Kyoto , ed. E. Kanda (Tokyo, Keigaku) (1970) 361.

[31] M. Sahoo, D. Behera, International J. of Modern Physics B 27 (2013) 1350099.

[32] A. K. Ghosh, S. K. Bandyopadhyay, and A. N. Basu, J. Appl. Phys. 86 (1999) 3247.

[33] M. Ausloos, Ch. Laurent, S. K. Patapis, C. Politis, H. L. Luo, P. A. Godelaine, F. Gillet, A. Dang and R. Cloots, Z. Phys. B: Condens. Matter 83 (1991) 355.

[34] P. Konsin, B. Sorkin, and M. Ausloos, Supercond. Sci. Technol. 11 (1998) 1.

[35] A. Kujur, D. Behera, Thin Solid Films 520 (2012) 2195.

[36] V.N. Vieira, P. Pureur, J. Schaf, Phys. Rev. B 66 (2002) 224506.

[37] A. Esmaeili, H. Sedghi, M. Amniat-Talab, M. Talebian, Eur.Phys. J. B 79 (2011) 443.

[38] Y. Zhao, C.H. Cheng, J.S. Wang, Supercond. Sci. Technol. 18 (2005) S43.

[39] S.W. Tozer, et al, Phys. Rev. Lett. 59 (1987) 1768.

[40] T.R. Dinger, T.K. Worthington, W.J. Gollagher, R.L. Sandstorm, Phys. Rev. Lett. 58, (1987) 2687.

[41] J.C. Le, J. Guillou Zinn-Justin, Phys. Rev. B. 21 (1980) 3976.

[42] W. Holm, Yu. Eltsev, O. Rapp, Phys. Rev. B 51 (1995) 11992.

[43] J. Kim, N. Goldenfeld, J. Giapintzakis, D.M. Ginsberg, Phys. Rev. B 56 (1997) 118.

[44] R. Menegotto Costa, P. Pureur, L. Ghivelder, J.A. Campa´, I. Rasines, Phys. Rev. B 56 (1997) 10836.

[45] A. Harabor, N. A. Harabor, M. Deletter, Optoelectronics and advanced materials 8 (2006) 1072.

Chapter 4

STUDY OF STRUCTURE AND ELECTRICAL TRANSPORT PROPERTY IN $BaSnO_3$, Cr_2O_3 AND $BaTiO_3$-$CoFe_2O_4$ COMPOSITES OF $YBa_2Cu_3O_{7-\delta}$

4. INTRODUCTION

This chapter deals with the structural modifications and temperature dependence of resistivity on a series of polycrystalline samples of (1-x) YBCO + x $BaSnO_3$ (x = 0.0, 0.1, 0.3, 0.5, 1.0, 2.5, 5.0 wt.%), (1-x) YBCO + x Cr_2O_3 (x = 0.0, 2.3,4.4, 6.1,7.4 wt.%) and (1-x) YBCO + x BTO-CFO (x = 0.0, 0.2, 0.4, 0.6 wt.%) prepared by solid-state sinter route. Emphasis has been made on the conduction mechanism in this chapter. Phenomenological investigation of thermodynamic fluctuations in the transport properties of high T_c superconductors has appeared to explain the cause of excess electrical conductivity ($\Delta\sigma$) related to the structural properties. The fluctuation conductivity has been analyzed using the logarithm of the excess conductivity by identifying the Gaussian and critical regimes. YBCO structure can be viewed as constituted of superconducting layers composed of CuO_2 planes separated by isolating CuO chains with complex crystal chemistry and granularity. The principal aim of this chapter is closely related to the inclusion of dielectric ($BaSnO_3$), magnetic (Cr_2O_3) and magneto-electric material ($BaTiO_3$-$CoFe_2O_4$) to observe the changes in the superconducting properties of YBCO through the fluctuation conductivity. Since the discovery of HTSC, on-site substitution studies have proved to be very useful in understanding the mechanism of high temperature superconductivity [1,2]. Analysis of the temperature dependence of resistivity in a series of these samples with varying BSO, Cr_2O_3 and BTO-CFO contents enable us to quantify the effect of fluctuation induced conductivity in these systems in terms of weak-link resistivity across grain boundaries arising due to the misaligned grains and sample dependent defects such as voids and cracks.

4.1 PART 1. STUDY OF STRUCTURE AND ELECTRICAL TRANSPORT PROPERTY IN YBCO/BSO COMPOSITE SYSTEM

4.1.1. Synthesis and characterization tools

Synthesis of YBCO/ $BaSnO_3$ composites

The synthesis of composite material consisting of (1-x) YBCO + x BSO (x = 0.0, 0.1, 0.3, 0.5, 1.0, 2.5, 5.0 wt. %) has been described in chapter 2 (section 2.2.2). All the samples were characterized by XRD, RAMAN, FTIR and SEM techniques. DC electrical resistivity measurement was done by four probe setup connected by a Nano-voltmeter (Keithley-2182A) and constant current source (Keithley-6221). Temperature variation is made through controller (Lakeshore 332). Low temperature was achieved by closed cycle He refrigerator (Janis cryostat). Data acquisition was carried out by a computer controlled Lab view program. Details are described in chapter 2 (section 2.4.6).

4.1.2. Result and Discussion

4.1.2.1. Phase formation of YBCO/ BSO composite system

(a)

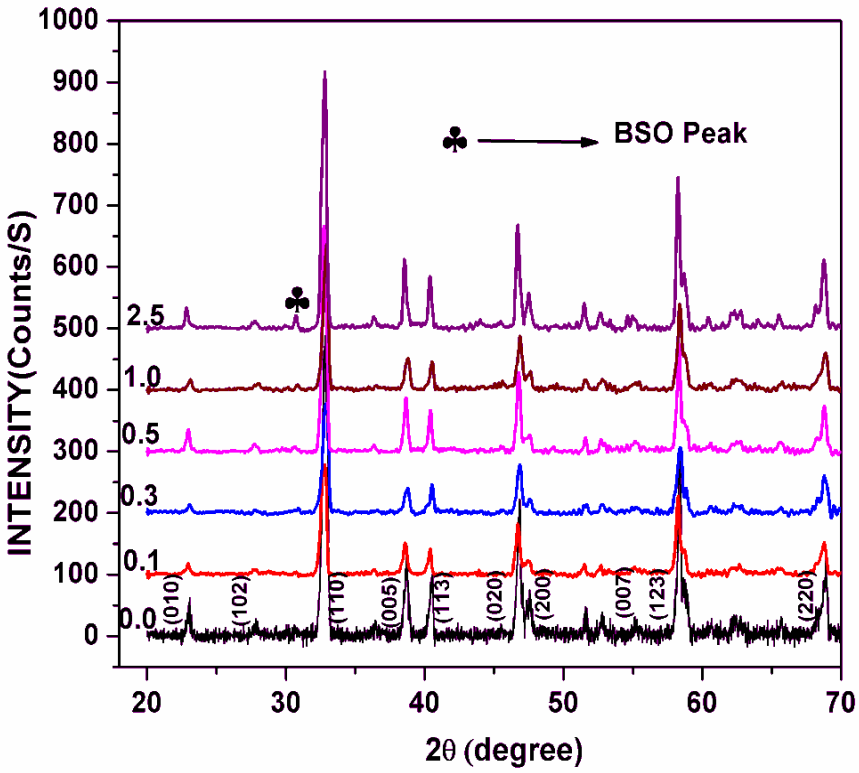

(b)

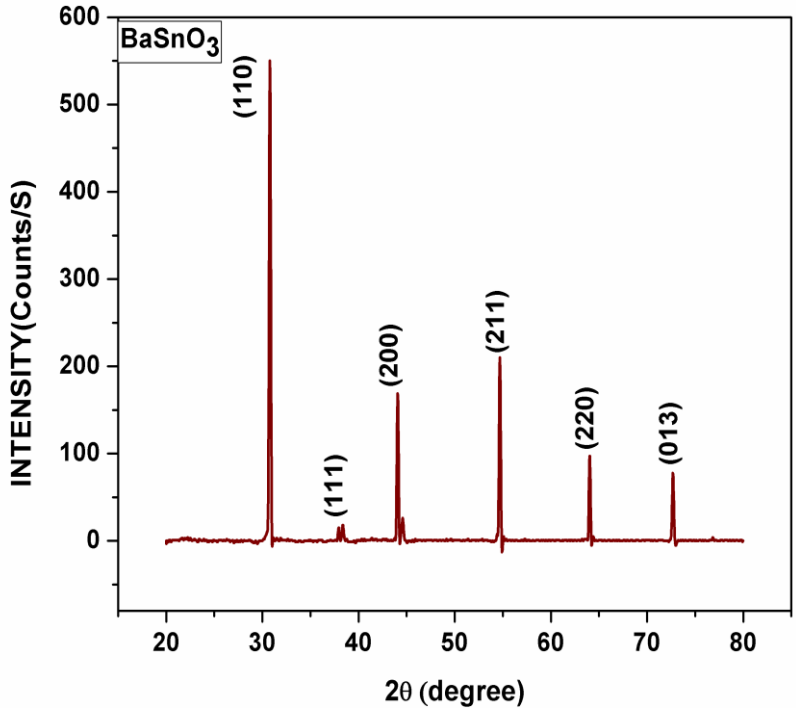

Fig 4.1.1 XRD Patterns of (a) YBCO+ x BSO Samples (x = 0.0, 0.1, 0.3, 0.5, 1.0, 2.5 wt. %) and (b) $BaSnO_3$.

Fig 4.1.1 shows the diffraction pattern of $BaSnO_3$ and $YBa_2Cu_3O_{7-y}$/x $BaSnO_3$ composite samples. The diffraction pattern of $BaSnO_3$ shows cubic structure with space group P_{m3m} and lattice parameter a = b = c = 4.108 Å. Diffraction pattern of the composite samples is indexed using Check Cell software and the results are found to be in orthorhombic phase with a space group P_{mmm}, with some BSO peaks.

Fig 4.1.2 shows magnified (005) peak. A non-monotonic decrease in intensity and broadening of peaks as a function of BSO wt. % is clearly shown in the plot. This is due to the strain applied by BSO particles in the YBCO matrix. Basically the crystallite size is reflected in the broadening of a particular peak in a diffraction pattern associated with a particular planar reflection from the crystal unit cell. It is inversely related to the FWHM of an individual peak. The more narrow the peak, the larger the crystallite size. The figure 4.1.2 gives a clear picture of gradually broadening of FWHM with addition of BSO. The FWHM is highest for 1.0 wt. % addition of BSO (~0.57) and smallest for 2.5 wt. % (~0.14). It signifies the decrease in crystallite size with BSO addition.

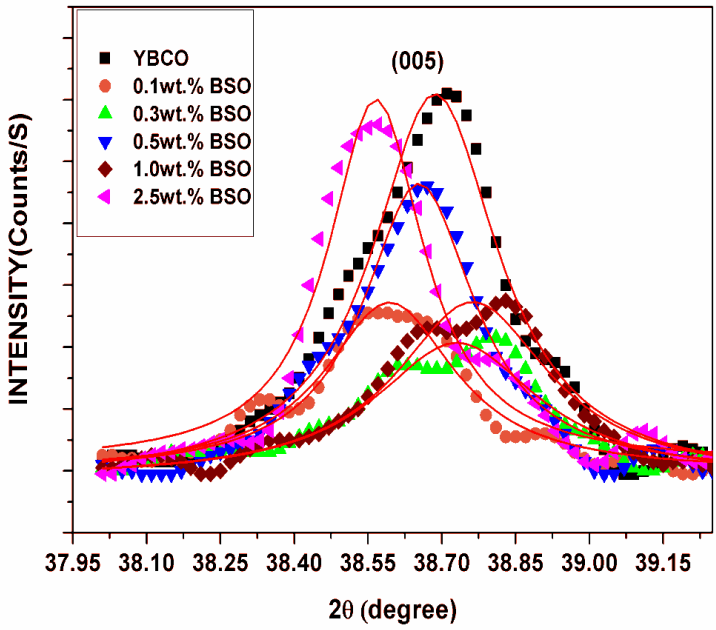

Fig 4.1.2. Lorentzian fitting of (005) plane by varying BSO wt.%.

The lattice parameters and unit cell volumes of these samples are tabulated in Table 4.1.1.

Table 4.1.1 Lattice parameters calculated from XRD graphs

BSO (wt. %)	a (Å)	b (Å)	c (Å)	V (Å^3)	Anis.	δ= b-a /b+a	FWHM
YBCO	3.818 (1)	3.884 (1)	11.681 (2)	173.218	1.7	0.008	0.21
0.1	3.814(2)	3.883(1)	11.670(4)	172.829	1.7	0.008	0.28
0.3	3.818(2)	3.889(2)	11.683(7)	173.471	1.8	0.009	0.38
0.5	3.824(1)	3.884(1)	11.681(6)	173.491	1.5	0.007	0.19
1.0	3.821(1)	3.873(1)	11.669(5)	172.686	1.3	0.006	0.57
2.5	3.826(1)	3.883(1)	11.674(3)	173.433	1.4	0.007	0.14

The tabulated data clearly shows that there is no significant change in 'a' parameter for the lower wt. % BSO added samples, but increases slightly for higher percentage addition. The length of 'b' parameter remains almost constant excluding the 1.0 wt. % added sample, where it reduced a little bit. There is a fluctuating behaviour in magnitude of 'c' lattice parameter and crystallite volume. The percentage deviation from tetragonal structure is expressed as anisotropy (=100(b-a)/0.5(b+a)) [3] (presented in Table 4.1.1). The anisotropy increases from 1.7 for pure YBCO to 1.8 for BSO content of x=0.3, but the lowest anisotropy equals to 1.3 for the higher BSO content of x=1.0. There is variation in orthorhombic distortion (δ) of the

samples and higher value signifies better oxygen ordering. Superconductivity of YBCO is associated not only with the oxygen content, but also with the ordering of the oxygen atoms and oxygen vacancies in the Cu-O basal plane. The complete ordering is reflected in rows of empty O (5) and filled oxygen sites O (1). This asymmetric distribution of oxygen leads to an orthorhombic distortion (b-a / b+a), that is a measure of ordering. The big difference between b and a corresponds to the higher ordering degree [4, 5]. The lattice parameter 'c' is smaller for the sample with higher ordering. The smaller 'c' value could be responsible for a better interlayer exchange and consequently, could give better superconducting properties [6]. The oxygen stoichiometry value is calculated from the relation 7-y = 75.250-5.856c (presented in Table 4.1.2) [7]. If the substitution takes place on Cu (2) site, there is no orthorhombic to tetragonal structural transition i.e. the structure remains orthorhombic even for higher dopant concentrations and oxygen ordering in the CuO chains remains intact. As the ionic radius of Sn (0.69 Å) is smaller than that of Cu (0.73 Å) and Sn also possess +2 valence it substitutes preferentially at the Cu (2) site. From the tabulated values of δ and O_{7-y} it is also clear that the structure remains orthorhombic and sample shows improved oxygen ordering.

4.1.2.2. RAMAN analysis

Raman spectroscopy is a characterization method that measures the frequencies of the long-wavelength lattice vibrations (phonons). Figure 4.1.3 shows the Raman spectra of (1-x) YBCO+ x BSO (x = 0.0, 0.1, 0.3, 0.5, 1.0, 2.5 wt. %) composite samples. The 500 cm^{-1} represents the stretching of apical oxygen or the bridging oxygen O (4) denoted as O (4) Ag. 432 cm^{-1} represents the in phase vibration of O(2)-O(3) oxygen atom in CuO_2 plane marked as $O(2,3)A_g$ and 339 cm^{-1} represents out-of-phase c-axis vibration of O(2)-O(3) oxygen atom in CuO_2 plane labeled as $O(2,3)\ B_{1g}$ [8-11]. The other two Raman active modes are vertical along the c-axis given by Cu (2) atoms. 151 cm^{-1} denoted as Cu (2) A_g i.e. plane Cu in phase and 115 cm^{-1} marked as BaA_g i.e. Ba vibration. Generally the strong peak of 500 cm^{-1} shifts to the lower frequency side as the oxygen content decreases. In addition, the 115 cm^{-1} peak disappears for 7-y = 6.2 [12].

In our experimental RAMAN spectra (fig 4.1.3) the peak seen at 300 and 630 cm^{-1} for 2.5 wt.% added BSO sample is due to CuO [13] and $BaCuO_2$ [14] respectively. The mode at 223 cm^{-1} is due to oxygen depletion and attributed to the vibrations of Cu (1) and O (1) atoms [15]. The peaks at 664 and 690 cm^{-1} belong to an additional defect-induced modes caused by oxygen disorder in the O (1) or O (4) sites [16, 17]. Another remarkable feature is that the 500

cm^{-1} peak softens and broadens in the highest percentage of BSO (2.5 wt.%) whereas the vibrational mode at 115 cm^{-1} and 151 cm^{-1} gets harder with increase in BSO percentage.

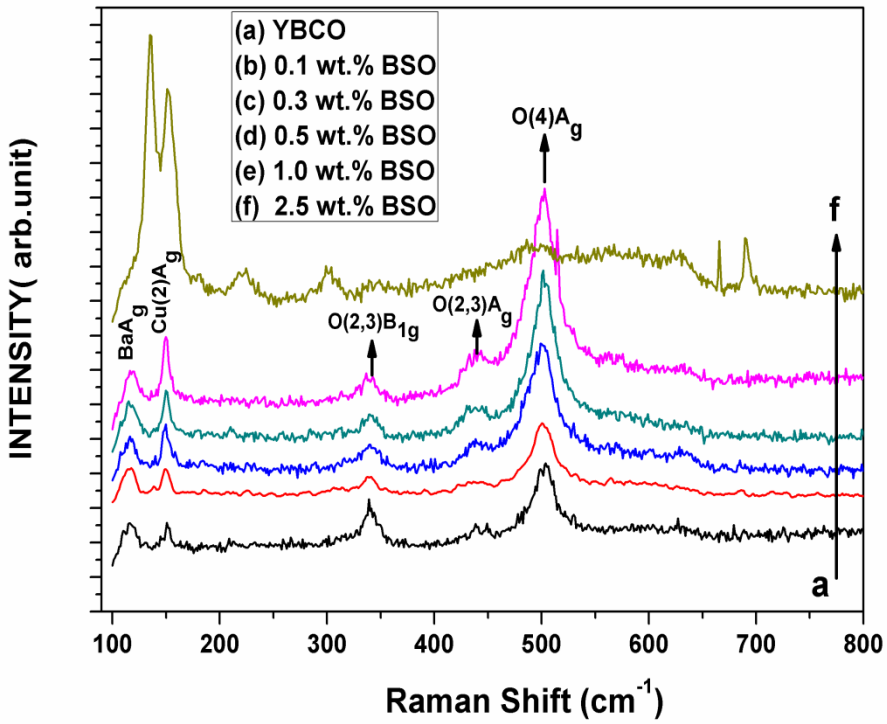

Fig 4.1.3. Micro-Raman spectra of YBCO + x BSO Samples (x = 0.0, 0.1, 0.3, 0.5, 1.0, 2.5 wt.%) samples.

Generally the O (4) phonon mode is associated with the oxygen content (y). Huong et al. proposed the following relationship between oxygen content and the peak frequency of the O (4) mode as y = 13.58-0.027ν where ν is the peak frequency of the O (4) mode [18].

Table 4.1.2 Oxygen content calculated using XRD and Raman spectra. 'c' is the lattice parameter along Z direction, 7-y is oxygen content, ν is the frequency of apical oxygen.

$BaSnO_3$ (wt. %)	c (Å)	O_{7-y} (from XRD)	ν (cm^{-1})	O_{7-y} (from Raman)
0.0	11.681(2)	6.85	504	7.02
0.1	11.670(4)	6.90	502	6.97
0.3	11.683(7)	6.80	500	6.92
0.5	11.681(6)	6.80	500	6.92
1.0	11.669(5)	6.90	502	6.97
2.5	11.674(3)	6.80	495	6.85

Linear relation is portrayed between oxygen content and the c axis lattice parameter. The c axis tends to increase with the decrease in oxygen content. Table 4.1.2 shows the oxygen content (7-y) evaluated using frequency of Raman mode and the c axis of XRD. It gives an insight of oxygen suppression occurring on the apical site and lengthening of the c axis due to BSO addition. The oxygen stoichiometry value calculated from XRD and RAMAN are found to be approximately same. Another thing was noticed that, even if the oxygen value remains high in all the pure as well as composite samples, the T_c value reduces to a large extent in the BSO added samples (seen from R~T plots). This signifies that the oxygen concentration is not the predominant factor for high T_c superconductivity in YBCO system. Its role is to adjust the coupling strength between positive and negative ions.

4.1.2.3. FTIR analysis

FTIR analysis of the sample reported in Fig. 4.1.4 indicates the structure of the molecules. The bonds corresponding to the labeled peaks have been identified and explained. The appearance of absorption peaks within 400 cm^{-1} to 800 cm^{-1} in FTIR spectrum are due to the presence of various kinds of metal oxygen bonds in the sample.

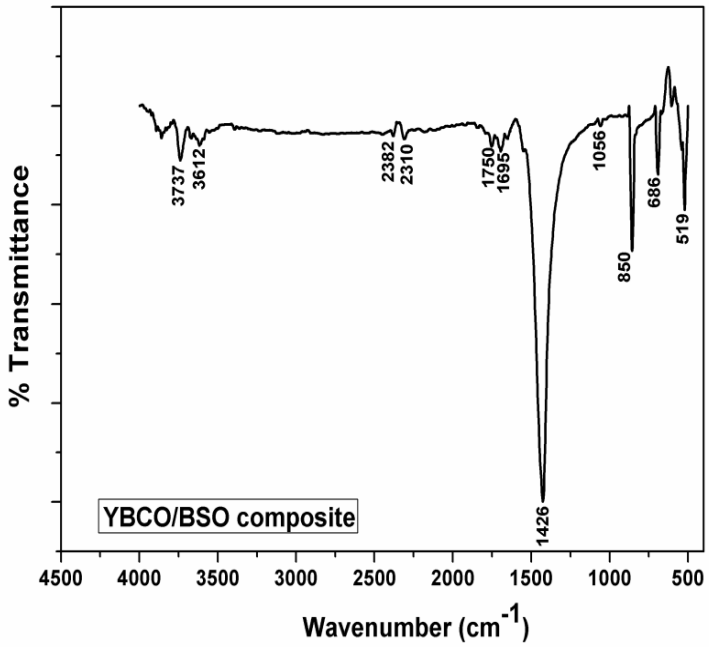

Fig 4.1.4 FTIR spectra of YBCO/BSO composite sample.

The observed intense peak at 1426 cm^{-1} is probably due to carbonate bond that is bonded with Ba ions [19]. Around 1695 cm^{-1} and 1750 cm^{-1} another two bonds appear which are assigned to be the C=O stretching modes [20]. The intense peak observed at 686 cm^{-1} corresponds to Sn-O asymmetric stretching mode. At 850 cm^{-1} and 1056 cm^{-1} two peaks are observed. These

correspond to stretching modes of CO_3^{2-}. The presence of these two peaks at different wave numbers can be attributed to the coupling motion of the C-O and C = O bonds. Carbonates, basically $BaCO_3$, may form due to the absorption of CO_2 from atmosphere during FTIR analysis.

4.1.2.4. Microstructural analysis

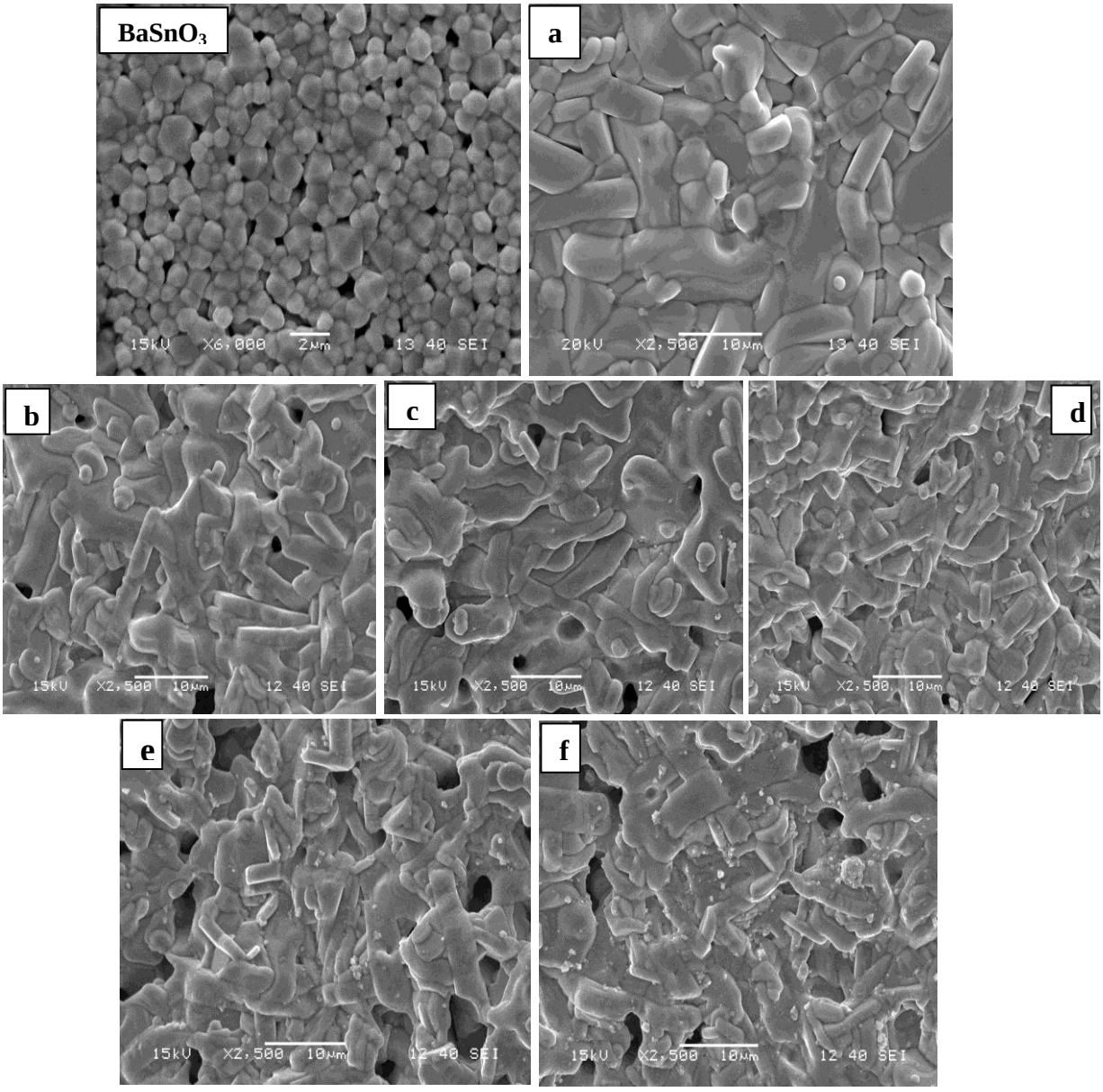

Fig 4. 1. 5. SEM micrographs of BSO and YBCO + x BSO (x= 0.0, 0.1, 0.3, 0.5, 1.0, 2.5 wt. %) samples marked as a, b, c, d, e, f respectively.

The grain size distribution of the pristine and composite samples is shown in fig 4.1.5. Pristine YBCO exhibits large and elongated grains randomly oriented in all directions. Microstructures clearly show that there is no significant change in the grain size due to the

addition of BSO. But the porosity, cracks and voids increases due to the addition of BSO. Extra deposition of BSO is observed as white dots between grains for 1.0 and 2.5 wt. % (fig 4.1.5 e, f) which may be accounted for excess addition of $BaSnO_3$. The microstructure of BSO shows hexagonal grains with average size less than 2 μm.

4.1.2.5. Temperature dependence of resistivity

Figure 4.1.6 shows the temperature dependence of resistivity measurement for different samples with various amount of the BSO. The resistive transition exhibits two different regimes. The first region is the normal state that follows a metallic behaviour (above $2T_c$). The normal state resistivity follows Anderson and Zou relation ρ_n (T)=A+BT. The ρ_n(T) is calculated by using the values of A and B parameters, which are obtained from the linear fitting of resistivity in the temperature range $2T_c$ to 300 K and extrapolated to 0 K gives resistivity slope (dρ/dT) and residual resistivity ρ_0 respectively.

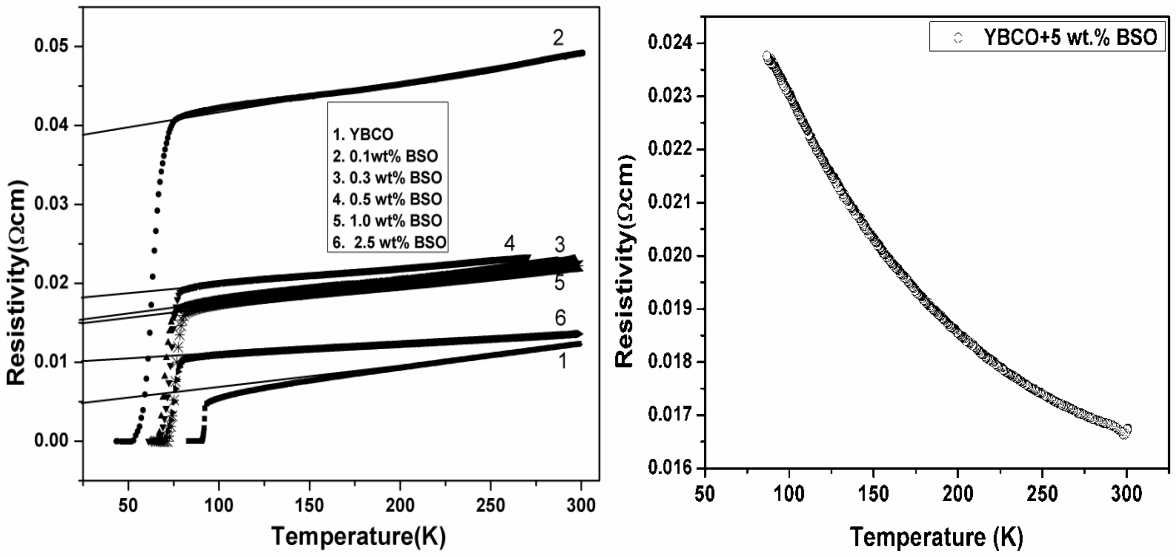

Fig 4.1.6 Resistivity dependences on the temperature for YBCO+ x BSO (x = 0.0, 0.1, 0.3, 0.5, 1.0, 2.5, 5.0 wt. %) composites.

The second region is characterized by the contribution of Cooper pairs fluctuation to the conductivity below T_c, where ρ (T) is deviated from linearity behaviour. This happens due to the increasing rate of Cooper pair formation on decreasing the temperature. Therefore, the fluctuation induced conductivity in this region follows the AL model to yield the dimensional exponent appropriate to fluctuation-induced conductivity. The normal state resistivity of the composite samples is higher than that of pure samples (Table 4.1.3). At temperature T_{c0} the electrical resistivity vanishes which signifies the coherence transition. A finite tailing is observed in the superconducting transition for all the YBCO/BSO composites before the

resistance attains zero value. It indicates that the superconducting grains get progressively coupled to each other by Josephson tunneling across the grain boundary weak links. The zero-resistance at T_{c0}, characterizes the onset of global superconductivity (where all the grains become superconducting i.e. intra-grain as well as grain boundaries become superconducting) in the samples. The superconducting transition temperature (T_c) is severely damaged by the low wt. % addition of BSO as observed from figure 4.1.7. T_c gradually increases with increase in wt. % of BSO and attends a plateau like behavior for higher percentage addition. For 5 wt. % the sample loses its superconducting property. The reason for the depressed T_c may be due to replacement of Sn^{+4} for Cu^{+2} ion in Cu (1) site in YBCO as observed in the $YBa_2Cu_{3-x}Sn_xO_{7-y}$ and Bi-2212 system. The change in T_c is only due to the amount of Sn replacing for Cu^{+2} in Cu (1) site which is very small. After doping in YBCO system Sn no longer exist as SnO_2 but as Sn^{+4} and occupies four sites namely Ba, Y, Cu(1), Cu(2) respectively. Sn mostly prefers Ba sites than Y, Cu (2) and probability for Cu (1) site is least. As Cu^{2+} is replaced by Sn^{4+}, in order to maintain the charge balance, the oxygen content must be increased. The variation of the oxygen content is dependent on the necessity of the charge balance [21].

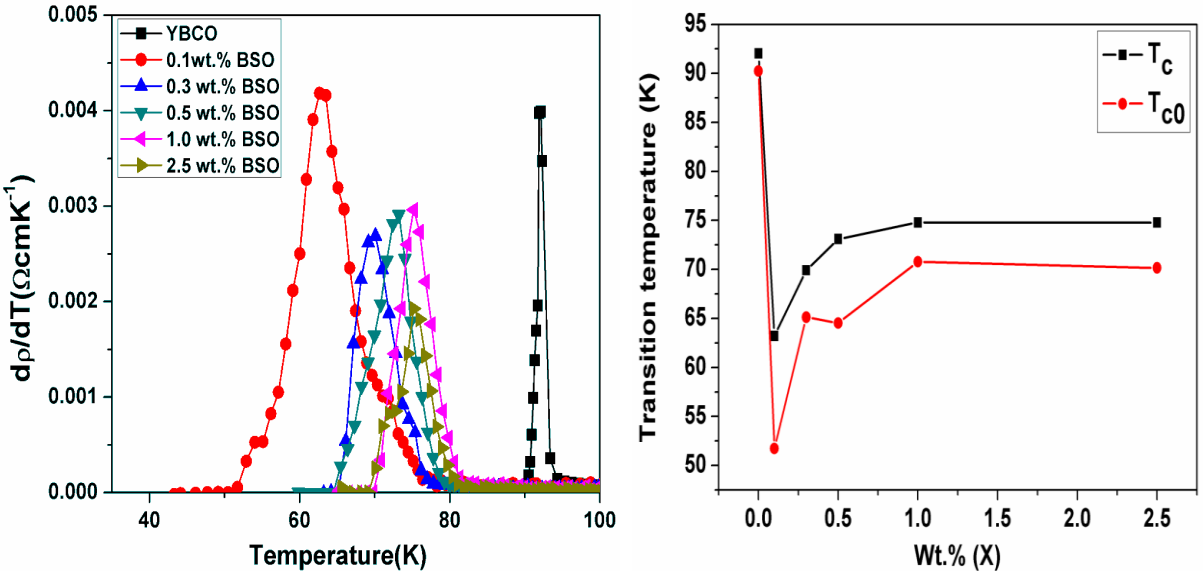

Fig 4.1.7 Temperature derivative of resistivity and variation of transition temperatures for YBCO + x BSO composites (x = 0.0, 0.1, 0.3, 0.5, 1.0, 2.5 wt. %).

Temperature derivative of resistivity graphs (fig 4.1.7) shows a sharp peak at T_c, which is related to intra-granular fluctuation. The temperature value corresponding to this maximum peak is close to the bulk critical temperature value T_c which broadens for composite samples.

The transition width (ΔT_c) defined as full width half maxima which increase with addition of composite. This may be due to the gradual occurrence of non-superconducting additional phases and the effect of microscopic inhomogeneity. The increasing value of ρ_0 and the decreasing trend in the value of T_{c0} indicates that the connectivity between grains decreases gradually with the addition of composite. The percolation factor 'α_n' arising due to current frustration caused by misalignment of anisotropic grains and sample defects such as voids and cracks are estimated from the temperature coefficient of resistivity $d\rho/dT$. This factor contributes to percolate conduction in granular copper oxides.

Table 4.1.3 Variation of normal state and superconducting parameters in the composites with different BSO wt.%.

BSO (wt.%)	T_{c0} (K)	T_c(K)	ΔT_c(K)	α_n	$\rho_n(0)$ ($\mu\Omega$ cm)	ρ_{wl} ($\mu\Omega$.cm)	ρ_P($\mu\Omega$.cm)	$\alpha_{str.}$
0.0	90.24	92.04	1.8	0.016	3130	50.7	1043	0.048
0.1	51.73	63.21	11.48	0.013	37730	494.2	12576	0.039
0.3	65.13	69.92	4.79	0.019	15360	297.9	5120	0.058
0.5	64.53	73.10	8.57	0.025	18080	464.6	6026	0.077
1.0	70.78	74.79	4.01	0.020	15060	313.2	5020	0.062
2.5	70.15	74.77	4.62	0.038	9660	368.0	3220	0.114

4.1.2.6. Excess conductivity

The fluctuation induced ordering in localized charge carriers is studied carefully by analyzing resistivity ρ (T) plots (shown in Fig. 4.1.6). Chapter 3 discussed extensively on the theory of excess conductivity giving details of all the critical exponents correlated with dimension of fluctuation. The excess conductivity plot is shown in Fig.4.1.8 representing two linear fits: one with slope value 0.5 for 3D fitting and the other with slope 1 for 2D fitting. These fittings match well for theoretically predicted values close to 1 and 0.5. In HTSCs the CuO_2 conducting planes are coupled to charge reservoir layers. The 2D fit reflects the localization of Cooper pairs in CuO_2 conduction plane at $T_{c\ onset}$ temperature range [22]. The 3D nature highlights the intra-cell coupling of CuO_2 layer where the charge carrier's tunnels through the resistive reservoir layer by charge transfer process at temperatures lower than $T_{c\ onset}$. As the temperature is lowered a crossover occurs from 2D regime to 3D regime denoted by T_{LD}.

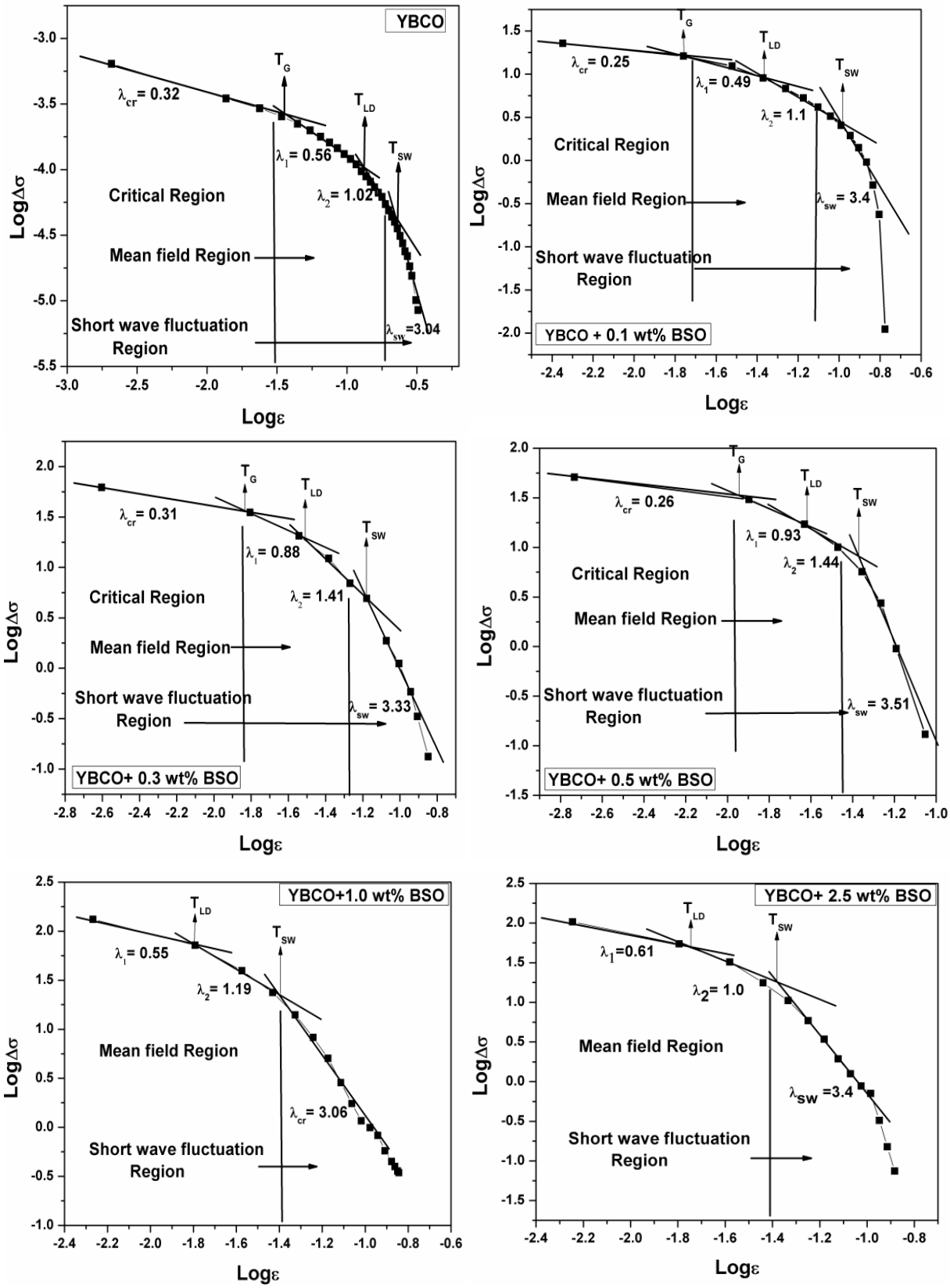

Fig. 4.1.8 log-log plot of excess conductivity $1/\rho - 1/\rho_R$ as a function of reduced temperature $\epsilon = (T-T_c)/T_c$ in YBCO+ x BSO composites.

Table 4.1.4 Parameters extracted from Excess conductivity analysis in YBCO/BSO composites.

BSO (wt. %)	T_G(K)	T_{LD}(K)	$T_{2D\text{-}SW}$(K)	$\xi_c(0)$ (A^0)	$J = [2\,\xi_c(0)]^2/d^2$
0.0	113.43	129.99	140.02	3.74	0.410
0.1	64.31	65.90	86.66	1.19	0.041
0.3	71.01	84.96	91.38	2.70	0.213
0.5	84.08	87.53	91.66	2.59	0.196
1.0	--	87.20	93.34	2.37	0.164
2.5	--	87.77	93.63	2.42	0.171

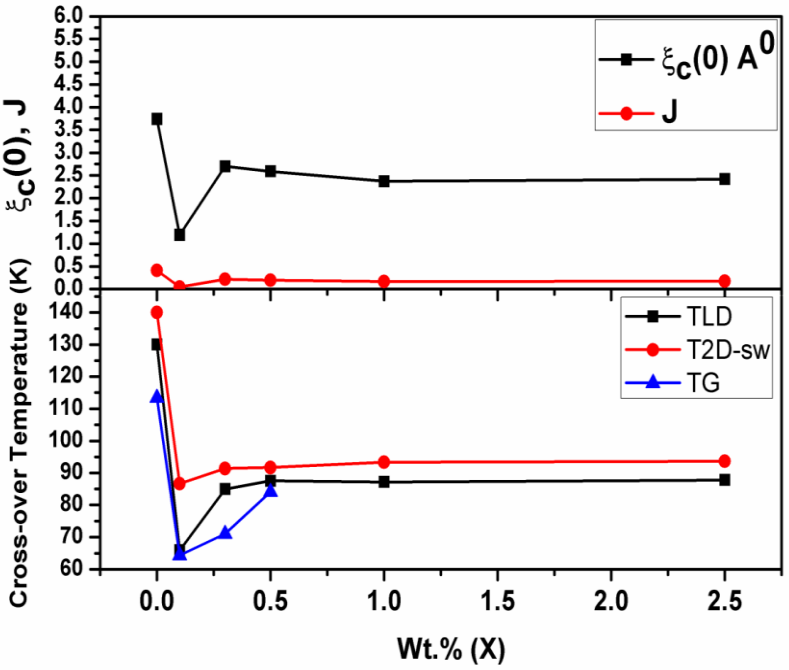

Fig. 4.1.9 Variation of cross over temperatures with BSO wt.%.

The different regions (Table 4.1.4) observed are the critical region at $T< T_c$, the mean field region at T close to T_c and the short wave fluctuations at $T >T_c$. The different crossover temperatures T_G, T_{LD}, $T_{2D\text{-}SW}$ decrease in the composite samples as compared to the pristine (shown in fig. 4.1.9) and centered at a particular low temperature for higher wt. % of BSO. Critical region is suppressed for 1.0 and 2.5 wt. % addition of BSO. The coherence length $\xi_c(0)$ and inter-layer coupling J is higher in the pristine sample as compared to the composite samples (fig. 4.1.9). This means that the added BSO decreases the CuO_2 interlayer coupling. For higher percentage addition the trend follows a plateau like behavior i.e. remains almost constant.

4.1.3 Conclusions

The effect of dielectric inhomogeneity ($BaSnO_3$) on the structural property and fluctuation conductivity is studied. XRD graphs show the unchanged orthorhombic structure and improved oxygen ordering in the composite samples. Raman studies show the additional defect-induced modes in the higher percentage addition of BSO. SEM micrographs reveal the unchanged grain size with the incorporation of BSO particles in the YBCO matrix. It is found that with the addition of BSO, T_{c0} decreases and the transition width ΔT_c increases as compared to pure YBCO which signifies the degradation of inter-grain weak links. The different crossover temperatures T_G, T_{LD}, $T_{2D\text{-}SW}$ decrease in the composite samples as compared to the pure YBCO. The experimental data fits well with theoretical predicted ones. Critical region get suppressed for higher wt. % addition of BSO. The Lawrence-Doniach temperature (T_{LD}) centered in the low temperature region for higher wt. % addition of BSO. This signifies that fluctuation of Cooper pairs in 3D is dominated in the mean field region.

4.1.4 References

[1] L. T. Romano, O. F. Schilling, C. R. M. Grovenor, Physica C 178 (1991) 41.

[2] O. F. Schilling, Applied Physics Letters 52 (1988) 1817.

[3] A. Abo-Arais, M. A. Taher Dawoud, Turk J Phys 29 (2005) 33.

[4] Y.C. Lana, X.L. Chen, Y.G. Cao, J.K. Huang, G.C. Che, G.D. Liu, Y.P. Xu, T. Xu, J.Y. Li, Physica C 336 (2000) 151.

[5] A. Ozturk, I. Duzgun, S. Celebi, J. Alloys and Compounds 495 (2010) 104.

[6] A. Kulpa, A.C.D Chaklader, N. R Osborne, G. Roemer, B. Sullivan, D. L Williams, Solid State Commun.71 (1989) 265.

[7] P. Benzi, E. Bottizzo, N. Rizzi, J. Crystal Growth 269 (2004) 625.

[8] R. Liu, C. Thomsen, W. Kress, M. Cardona, B. Gegenheimer, F.W.de Wette, J. Prade, A.D. Kulkarni, U. Schroeder, Phys. Rev. B 37 (1988) 7971.

[9] R.E. Cohen, W.E. Pickett, H. Krakauer, Phys. Rev. Lett. 64 (1990) 2575.

[10] C.O Rodriguez, A.I Lichtenstein, I.I Mazin, O. Jepsen, O.K Anderson, M. Methfessel, Phys. Rev. B 42 (1990) 2692.

[11] J. Prade, A.D Kulkarni, F.W de Wette, U. Schroeder, W. Kress, Phys. Rev. B 39 (1990) 2771.

[12] A. Yamanaka, F. Minami, K. Watanabe, K. Inoue, S. Takenaka, N. Lyi, Jpn. J. Appl. Phys. 26 (1987) L1404.

[13] I. Nedkov, Supercon. Sci. Tech. 11 (1998) 21.

[14] H. Chang, Q.Y Chen, W.K Chu, Physica C 309 (1998) 215.

[15] V.G Ivanov, M.N Iliev, C. Thomsen, Phys. Rev. B 52 (1995) 13652.

[16] Ming-Sheng Zhang, Z. Yin, G. Hu, Q. Chen, Phys. Rev. B 41 (1990) 2003.

[17] P. D. Beale et al, Solid State Commun. 65 (1988) 1145.

[18] P.V Huong, J. C Bruyere, E. Bustarret, P. Granchampb, Solid State Commun. 72 (1989) 191.

[19] M. M Silvan, L. F Cobas, R.J M-Palma, M.H Velez, J. M M-Duart, Surf. Coat Technol. 151 (2002) 118.

[20] P. Duran, D. Gutierrez, J. Tataj, M.A. Banares, C. Moure, J. Eur. Ceram. Soc. 22 (2002) 797.

[21] D.Y Zhang, G.M Wang, Y.X Wang, Z.H Wang, Y.H Zhang, Solid State Comm. 75 (1990) 629.

[22] W. Lang, G. Heine, Phys. Rev. B 51 (1995) 9180.

4.2 PART 2. STRUCTURE AND ELECTRICAL TRANSPORT STUDIES IN YBCO/Cr_2O_3 COMPOSITE SYSTEM

4.2.1. Synthesis and characterization tools

Synthesis of YBCO/ Cr_2O_3 composites

The synthesis of composite material consisting of (1-x) YBCO + x Cr_2O_3 (x = 0.0, 2.3, 4.4, 6.1, 7.4 wt. %) has been described in chapter 2 (section 2.2.6). All the samples were characterized by XRD, RAMAN and SEM techniques. DC electrical resistivity measurement was done by four probe setup connected by a Nano-voltmeter (Keithley-2182A) and constant current source (Keithley-6221). Low temperature was achieved by closed cycle Helium refrigerator (Janis cryostat). Data acquisition was carried out by a computer controlled Lab view program.

4.2.2. Result and Discussion

4.2.2.1. Phase formation of YBCO/ Cr_2O_3 composite system

Figure 4.2.1 shows the X-ray diffraction patterns of the YBCO/x Cr_2O_3 composite samples. The diffraction pattern of the composite samples is indexed using Chekcell software. The samples are found to be in orthorhombic phase with space group P_{mmm} and some Cr_2O_3 peaks. The peak intensity is suppressed in the higher percentage addition of Cr_2O_3.

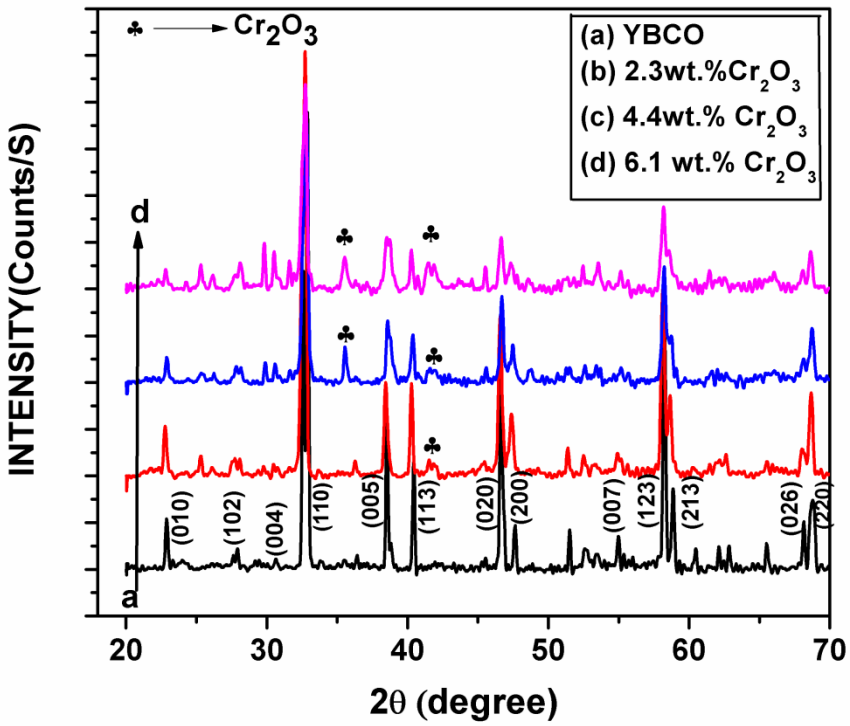

Fig. 4.2.1 XRD Patterns of YBCO+ x Cr_2O_3 Samples (x = 0.0, 2.3, 4.4, 6.1 wt. %).

The lattice parameters and unit cell volumes of these samples are presented in Table 4.2.1.

Table 4.2.1 Lattice parameters calculated from XRD graphs

Cr_2O_3(wt.%)	a (Å)	b (Å)	c (Å)	V(Å^3)	δ= b-a / b+a
0.0	3.815(1)	3.882(1)	11.683(2)	173.023	0.008
2.3	3.826(1)	3.889(1)	11.700(4)	174.087	0.008
4.4	3.821(1)	3.889(1)	11.697(5)	173.815	0.008
6.1	3.810(2)	3.891(2)	11.689(4)	173.286	0.010

From the above data it is clear that there is no significant change in 'b' parameter up to 4.4 wt. % of Cr_2O_3, but it increases for 6.1 wt. %. The length of 'a' parameter is greater in the composite samples as compared to that of pure sample and it is the lowest for 6.1 wt.%. The 'c' lattice parameter and crystallite volume is high in composite samples as compared to the pristine and highest for low percentage addition of Cr_2O_3. This elongation is expected due to the strain effect i.e. the non-uniform elastic distortions of the crystal lattice at the atomic level imposed by the magnetic inhomogeneity on YBCO matrix. The orthorhombic distortion (δ) remains almost constant up to 4.4 wt. % and increases for the 6.1 wt. % composite. This higher value of δ signifies that oxygen ordering is higher. Since superconductivity of YBCO is associated not only with the oxygen content but also with the ordering of the oxygen atoms and oxygen vacancies in the Cu-O basal plane, the complete ordering is reflected in rows of empty O(5) and filled oxygen sites O(1). This asymmetric distribution of oxygen leads to an orthorhombic distortion (b-a/b+a), that is a measure of ordering. The big difference between b and a, corresponds to the higher ordering degree [1]. It can also be seen that the lattice parameter c is smaller for the sample with higher ordering. The smaller 'c' value could be responsible for a better interlayer exchange and consequently, could give better superconducting properties [2]. The oxygen stoichiometry value is calculated from the relation 7-y =75.250-5.856c, where c is the length of the c-axis lattice parameter (presented in Table 4.2.2) [3]. From the calculated values it is clear that there is no significant change in the oxygen value in the composite samples. We know that if the substitution takes place on Cu (2) site, there is no observed structural O-T transition i.e. the structure remains orthorhombic even for higher dopant concentrations and oxygen order in the CuO chains remains intact. As 'Cr' is a divalent cation it possibly substitutes at the Cu plane site. From the values of δ and O_{7-y} it is also clear that the structure remains orthorhombic and an improved oxygen ordering.

4.2.2.2. Raman analysis of YBCO/ Cr_2O_3 composite samples

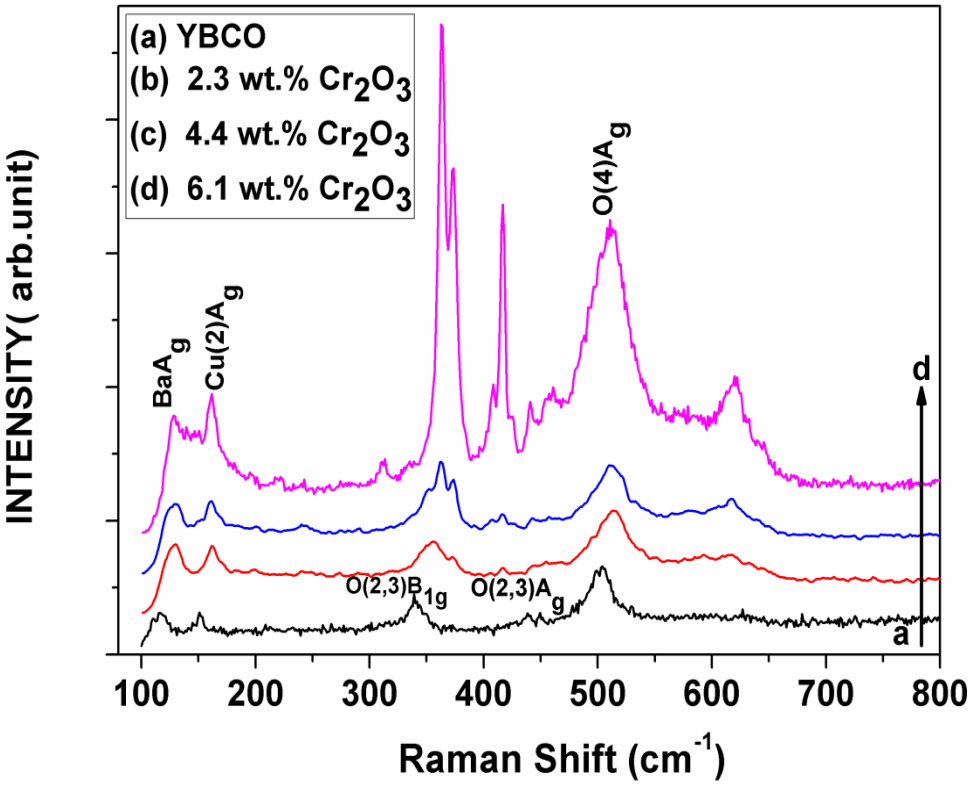

Fig. 4.2.2 Micro Raman spectra of YBCO+ x Cr_2O_3 samples (x = 0.0, 2.3, 4.4, 6.1 wt.%).

Fig 4.2.2 shows the Raman spectra of (1-x) YBCO+xCr_2O_3 (x= 0.0, 2.3, 4.4, 6.1 wt. %) composite samples. All the vibrational modes are present in the pristine as well as composite samples. The O (2, 3) B1g mode shifts to the higher frequency side and peak splitting occurs with increase in Cr_2O_3 concentration. The peak seen at 310 cm^{-1} for 6.1wt.% added Cr_2O_3 and at 620 cm^{-1} for all the composite samples is due to CuO [4] and $BaCuO_2$ [5] respectively. Another defect induced mode at 416 cm^{-1} arises in the Cr_2O_3 added samples whose intensity is high in the highest wt. %. This is assigned to the stretching vibrations of the oxygen atoms. The strongest band at 504 cm^{-1} of orthorhombic YBCO was assigned to Cu (1)-O (2) Ag stretching mode and this mode is the most sensitive to the oxygen content [6,7]. All the vibrational modes gets harden in the highest wt. % added composite sample. Table 4.2.2 shows the oxygen content (y) evaluated using frequency of Raman mode and the c axis of XRD. The high oxygen stoichiometry value in the composites signifies that the added Cr_2O_3 does not affect the oxygen content.

Table 4.2.2 Oxygen content calculated using XRD and Raman spectra. 'c' is the lattice parameter along Z direction, y is oxygen loss, ν is the frequency of apical oxygen.

Cr_2O_3 (wt. %)	c (Å)	O_{7-y} (from XRD)	ν(cm^{-1})	O_{7-y} (from Raman)
0.0	11.683(2)	6.80	504	7.00
2.3	11.700(4)	6.70	514	7.20
4.4	11.697(5)	6.70	510	7.10
6.1	11.689(4)	6.80	510	7.10

4.2.2.3. Microstructural analysis of YBCO/ Cr_2O_3 composite samples

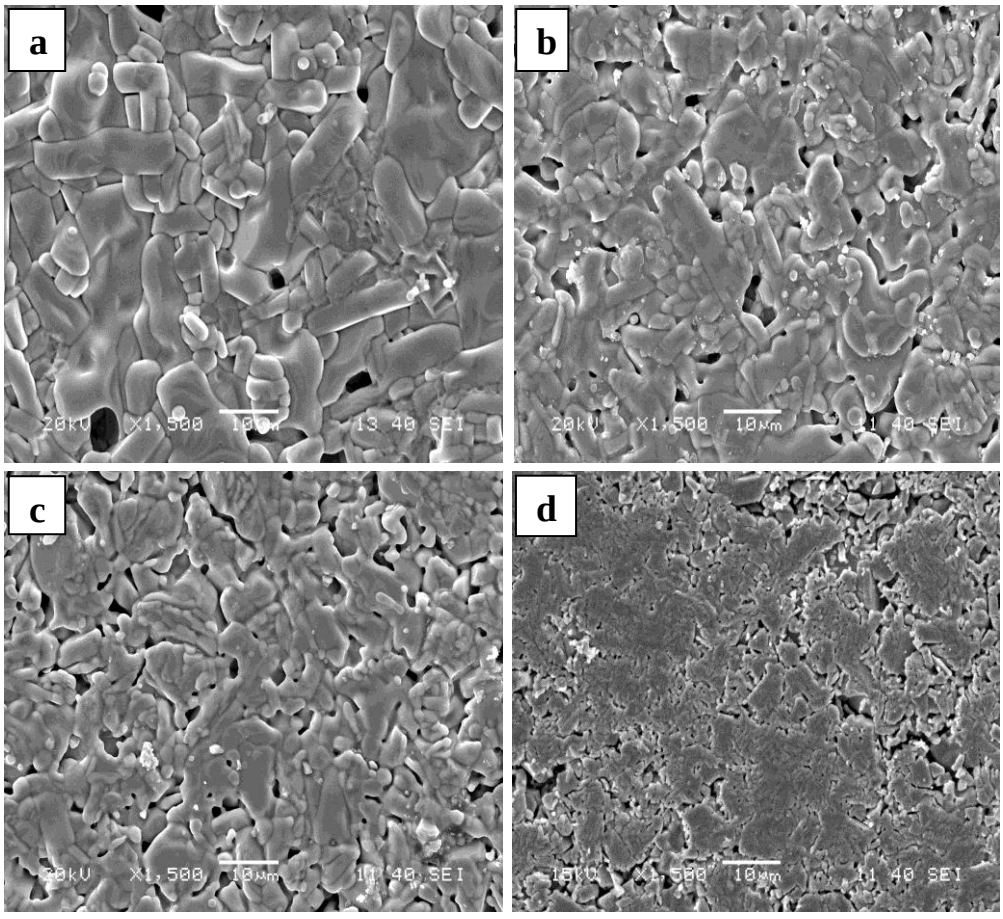

Fig. 4.2.3 SEM micrographs of YBCO + x Cr_2O_3 (x = 0.0, 2.3, 4.4, 6.1 wt. %) samples marked as a, b, c, d, respectively.

The grain size distribution of the pristine and composite samples is shown in figure 4.2.3. It shows that pristine YBCO exhibits large and elongated grains randomly oriented in all directions. The grain size is gradually reduced with the addition of Cr_2O_3. The grain size for 6.1 wt. % added sample (fig. 4.2.3 d) is ten times smaller than that of pure sample. Decrease

in grain size indicates that the strength and hardness of the samples increases in Cr_2O_3 added samples. From SEM micrographs, it is clear that Cr_2O_3 not only decreases the grain size but also increases porosity in the samples.

4.2.2.4. Temperature dependence of resistivity

Measurements of the resistivity dependence with temperature for different samples with various amounts of Cr_2O_3 are shown in figure 4.2.4. The normal state resistivity of the composite samples is higher than that of pure sample which is tabulated in Table 4.2.3. At the temperature value T_{c0} the electrical resistivity vanishes and the phase of the order parameter acquired long range order between the grains of the system. This critical temperature signifies the coherence transition. A finite tailing is observed in the superconducting transition for all the YBCO + x Cr_2O_3 composites before the resistance attains zero value. It indicates that the superconducting grains get progressively coupled to each other by Josephson tunneling across the grain boundary weak links. The onset of global superconductivity decreases with addition of Cr_2O_3 indicating that it adheres to grain boundary forming weak links. For 7.4 wt. % addition a purely semiconductor type behavior was observed without superconducting transition.

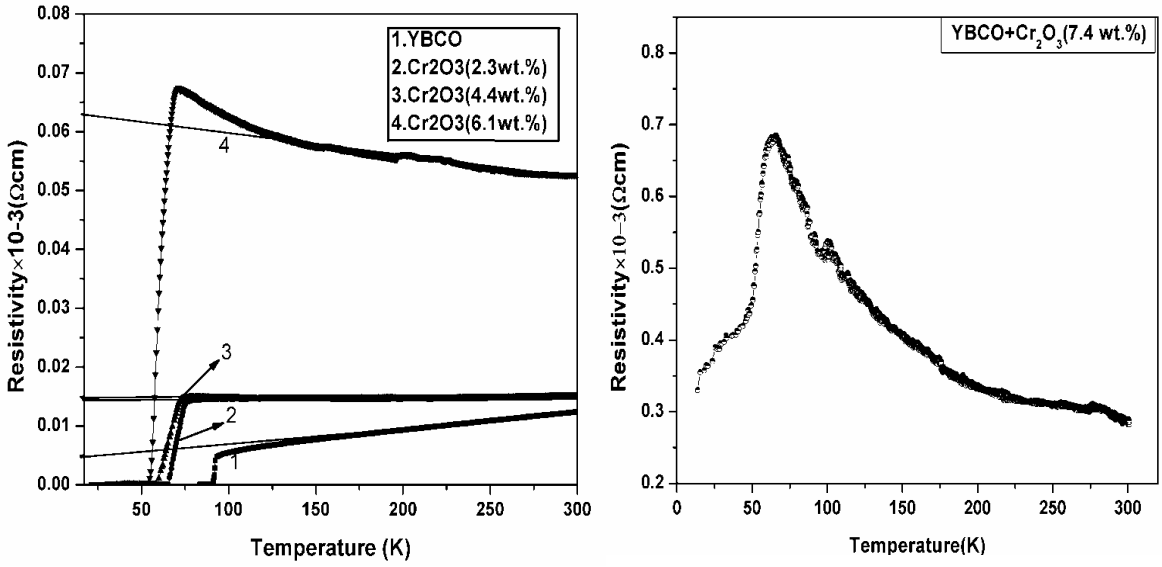

Fig. 4.2.4 Resistivity dependences on the temperature for YBCO + x Cr_2O_3 (x=0.0, 2.3, 4.4, 6.1, 7.4 wt. %) composites.

The superconducting transition temperature (T_c) is severely damaged by the addition of magnetic element Cr_2O_3 as observed from fig 4.2.4. From the temperature derivative of resistivity graphs (fig 4.2.5) firstly, we observe a sharp peak at T_c, which is related to intra-granular fluctuation. These characteristic fluctuations define the so called pairing transition

[8]. The temperature value corresponding to this maximum peak is close to the bulk critical temperature value T_c followed by hump or secondary peak which broadens for composite samples.

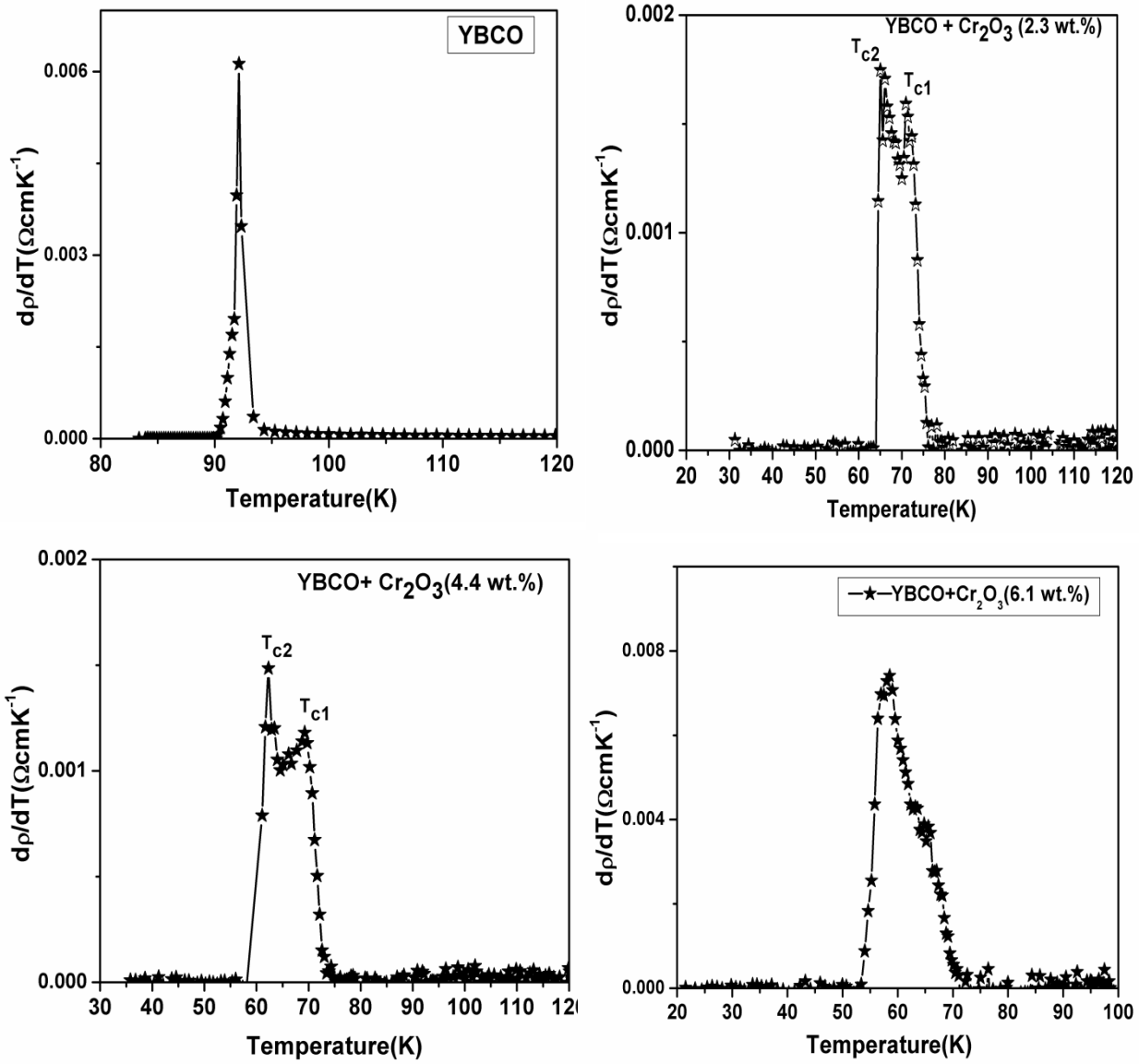

Fig. 4.2.5 Temperature derivative of resistivity for YBCO+xCr_2O_3 composites (x = 0.0, 2.3, 4.4, 6.1 wt. %).

One more point noticed for 2.3 and 4.4 wt. % added samples is that the superconducting transition temperature splits in two (revealed as double peaks in the dρ/dT plot) T_{c1} and T_{c2} along with a broadening of overall superconducting transition temperature. Such behavior is attributed to the weak-link nature of granular superconductors as the latter is composed of superconducting grains embedded in a non-superconducting host. Out of the two superconducting transition temperatures, the higher one (T_{c1}) marks the superconductivity in grains whereas the grain boundary still remains normal and the lower one (T_{c2}) when the grain

boundary also becomes superconducting. Transition at T_{c1} manifests significant amount of strongly coupled grains and the zero resistance state is achieved when the Josephson tunneling between the grains forms a connected superconducting path across the entire sample at T_{c2} as the temperature is lowered. The appearance of additional transition temperature T_{c2} and its broadening clearly reflects that the Cr_2O_3 added, goes to the grain boundary region, and becomes superconducting only due to proximity effect at lower temperatures. The transition width (ΔT_c) defined as full width half maxima increases with doping concentration. This may be due to the gradual occurrence of non-superconducting additional phases and the effect of microscopic inhomogeneity.

The percolation factor 'α_n' (shown in Table 4.2.3) arising due to current frustration caused by misalignment of anisotropic grains and sample defects such as voids and cracks are estimated from the temperature coefficient of resistivity dρ/dT. This factor contributes to percolative conduction in granular copper oxides. For polycrystalline Y-based HTSC percolative conduction factor, α_n is in the range of 0.05-0.2. Our experimental value also lies within this range. In the paracoherent state where all the grains become superconducting, nothing hinders conduction in this state. Only the structural quality factor (α_{str}) and the intergrain resistivity (ρ_{wl}) enter the paracoherent resistivity ρ_p. The relation $\rho n\,(0) > \rho_p > \rho_{wl}$ should be satisfied [9].

Table 4.2.3 Variation of normal state and superconducting parameters in the composites with different Cr_2O_3 wt. %.

Cr_2O_3 (wt. %)	T_{c0}(K)	T_c (K)	α_n	$\rho_n(0)$ (μΩ.cm)	ρ_{wl} (μΩ.cm)	ρ_P(μΩ.cm)	α_{str}
0.0	90.32	92.13	0.016	4861	77	1620	0.047
2.3	63.39	65.13	0.164	14381	2358	4793	0.491
4.4	55.93	59.60	0.179	14991	2683	4997	0.536
6.1	54.38	58.77	0.184	62950	11582	20983	0.551

The increasing value of ρ_0 and the decreasing trend in the value of zero-resistance critical temperature (T_{c0}) indicates that the connectivity between grains decreases gradually with the addition of composite. The transition temperatures decreases exponentially (Fig. 4.2.6) with increase in Cr_2O_3 percentage. All these effects are due to increased in-homogeneities in the inter-granular regions. Point defects and chemical dopants occupy various positions in a

crystal in the form of substituent or interstitial impurities. Grain boundary is a structurally distorted region in crystals, due to which an extra energy form in the boundary region. As a result of the existence of grain boundary energy as well as the Coulomb interaction between the boundaries and the impurity atoms, they tend to attract impurity atoms in order to decrease the grain boundary energy. Therefore, the chemical dopant has a higher probability to stay in the grain boundary region than to stay inside the crystal.

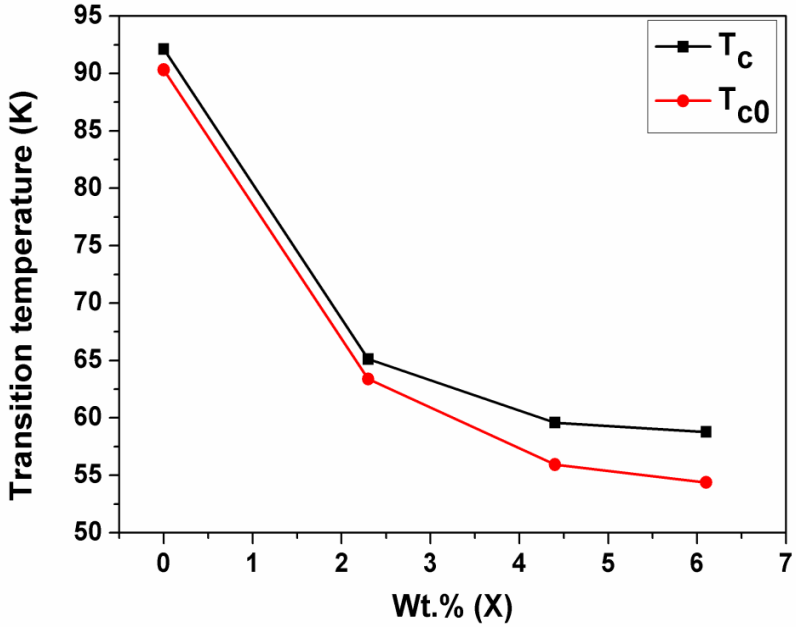

Fig. 4.2.6 Variation of transition temperatures with Cr_2O_3 wt. %.

4.2.2.5. Dimensionality fluctuations of excess conductivity

The excess conductivity has been analyzed in the light of Aslamazov-Larkin (AL) model and the dimensionality of fluctuation is found out. The excess conductivity plots are shown in Fig. 4.2.7. In order to explain the experimental data with theoretical predicted ones, the different regions of the plot were linearly fitted and the exponent values were determined from the slopes. The plot reveals three distinct regimes i.e. mean-field or the Gaussian fluctuations, critical fluctuations and short wave fluctuation region.

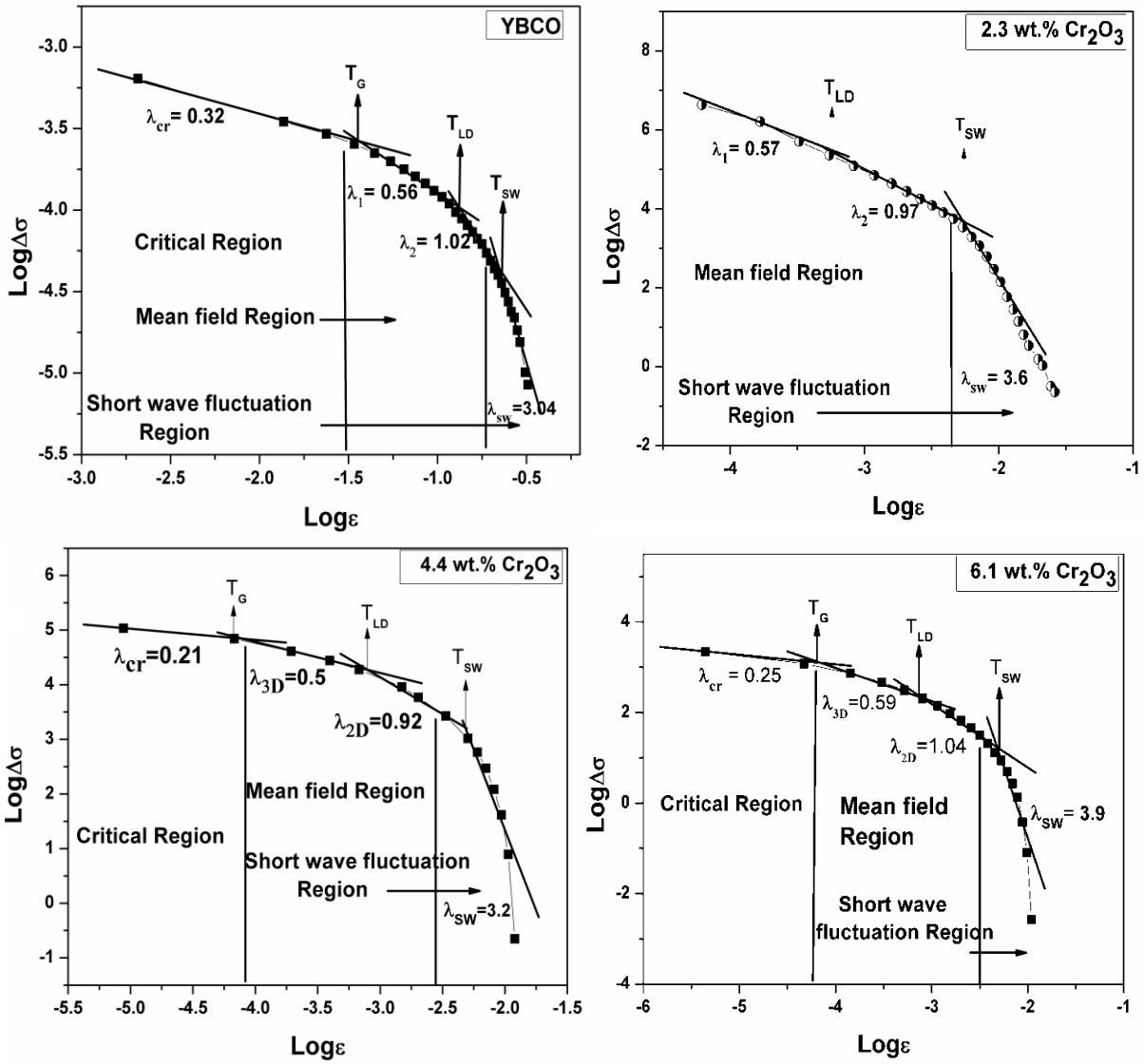

Fig. 4.2.7 Log–Log plot of excess conductivity $1/\rho - 1/\rho_R$ as a function of reduced Temperature $\epsilon = (T-T_c)/T_c$ in YBCO+ x Cr_2O_3 composite.

Table 4.2.4 The parameters extracted from excess conductivity analysis in YBCO/Cr_2O_3 composite.

Cr_2O_3(wt.%)	λ_{cr}	λ_1	λ_2	λ_{swf}	T_G(K)	T_{LD}(K)	$T_{2D\text{-}SW}$(K)
0.0	0.32	0.56	1.02	3.04	113.43	129.99	140.02
2.3	---	0.57	0.97	3.6	---	67.62	71.87
4.4	0.21	0.5	0.92	3.2	63.45	65.11	68.77
6.1	0.25	0.59	1.04	3.9	59.54	61.42	64.39

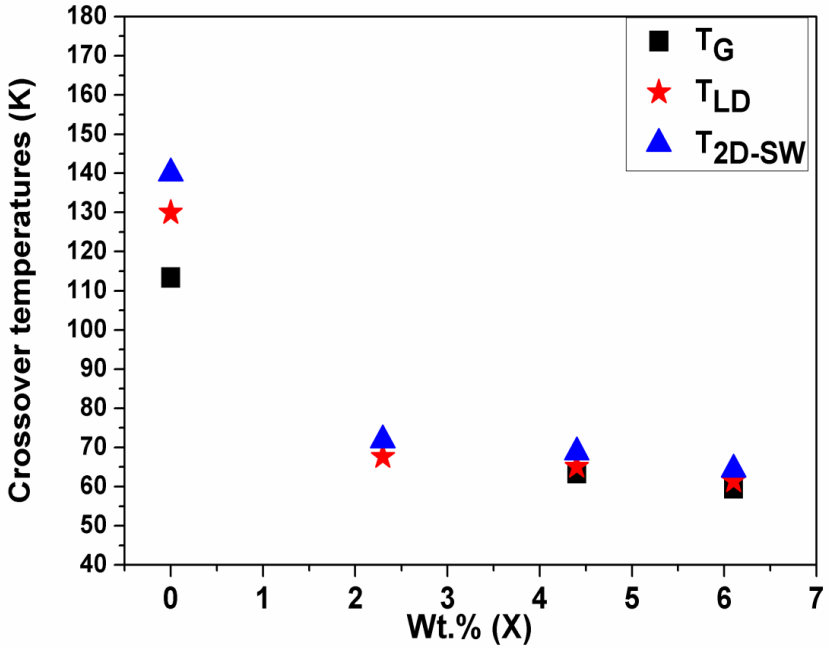

Fig. 4.2.8 Variation of different cross over temperatures with Cr_2O_3 wt.%.

In the log-log plot of the excess conductivity vs. the reduced temperature, different λ values or the exponents for different fluctuation regions above and below the crossover temperature has been observed. The regime that is close to T_c in the mean field region has 3D type of fluctuations but at temperature T_{LD} there is a crossover from 3D to 2D region of fluctuations. As we move to higher temperature side the superconducting fluctuations follow $1/\varepsilon^3$ behavior, such fluctuation region where the Ginzburg-Landau theory breaks down is known as the Short wavelength fluctuations (SWF). Different crossover temperatures decreases exponentially (fig. 4.2.8) with increase in Cr_2O_3 concentration. Critical region is suppressed for low percentage addition of Cr_2O_3. The width of transition between the cross over temperatures decreases in the composites as compared to the pristine sample.

4.2.3 Conclusion

This section presents reports on the experimental findings by embedding magnetic in-homogeneity Cr_2O_3 to YBCO matrix. XRD and RAMAN analysis confirms the unchanged orthorhombic structure with improved oxygen ordering in higher wt. % addition of Cr_2O_3. RAMAN graphs shows that the oxygen content remains high in all the pure as well as composite samples with some defect induced modes occurs due to stretching vibrations of oxygen atoms. SEM micrographs reveal the reduced grain size with the incorporation of magnetic Cr_2O_3 particles in the YBCO matrix. The different regions observed are the critical region at $T < T_c$, the mean field region at T close to T_c and the short wave fluctuations at $T > T_c$. No critical region was found for low percentage addition of Cr_2O_3. Addition of Cr_2O_3

accounts for rise of normal state as well as residual resistivity and weak-link resistivity with exponential decrease of T_c towards lower temperature zones. The splitting of transition temperature marked by double peak in the derivative curve could be correlated with Cr_2O_3 residing in the grain boundary which forms weak links or Josephson junction that results in progressive decoupling of grains. Decrease in the value of T_{c0} and increase in the value of transition width ΔT_c signifies the degradation of inter-grain weak links. The excess conductivity data revealed a dimensional crossover from 2D to 3D fluctuation as the temperature is lowered.

4.2.4 References

[1] A. Kulpa, A.C.D. Chaklader, N.R. Osborne, G. Roemer, B. Sullivan, D. L. Williams, Solid State Commun.71 (1989) 265.

[2] S. Kurihara: Interacting hole-spin model for oxide superconductors (1988).

[3] P. Benzi, E. Bottizzo, N. Rizzi, Crystal Growth 269 (2004) 625.

[4] I. Nedkov, Supercon. Sci. Tech. 11 (1998) 21.

[5] H. Chang, Q.Y. Chen, W.K. Chu, Physica C 309 (1998) 215.

[6] M. Stavola, D. M. Krol, W. Weber, S. A. Sunshine, A. Jayaraman, G. A. Kourouklis, R.J. Cava and E. A. Rietman, Phys. Rev. B36 (1987) 850.

[7] A. Yamanaka, F. Minami, K. Watanabe, K. Inoue, S. Takekawa and N. lyi, Jpn. J. Appl. Phys. 26 (1987) L1404.

[8] J. Roa-Rojas, R.M. Costa, P. Pureur, P. Prieto, Phys. Rev. B 61 (2000) 12457.

[9] A. Diaz, J. Maza, F. Vidal, Physical review B 55 (1997) 1209.

4.3 PART 3. STUDY OF STRUCTURE AND ELECTRICAL TRANSPORT PROPERTY IN YBCO / BTO-CFO COMPOSITE SYSTEM

4.3.1. Synthesis and characterization tools

Synthesis of YBCO/BTO-CFO composites

The synthesis of composite material consisting of (1-x) YBCO + x BTO-CFO (x = 0.0, 0.2, 0.4, 0.6 wt. %) has been described in chapter 2 (section 2.2.3, 2.2.4, 2.2.5). All the samples were characterized by XRD, RAMAN and SEM technique. DC electrical resistivity measurement was done by four probe setup connected by a Nano-voltmeter (Keithley-2182A) and constant current source (Keithley-6221). Details of measurement have been discussed in previous sections.

4.3.2. Result and Discussion

4.3.2.1. Phase formation of YBCO/ BTO-CFO composite system

Figure 4.3.1(a) shows the X-ray diffraction patterns of the $BaTiO_3$ and $CoFe_2O_4$. Figure 4.3.1 (b) represents the XRD pattern of $BaTiO_3$-$CoFe_2O_4$ system and Fig 4.3.1(c) shows the XRD patterns of $YBa_2Cu_3O_{7-y}$ /x $BaTiO_3$-$CoFe_2O_4$ composite samples. The diffraction pattern of the YBCO/ BTO-CFO composite samples is indexed using Chek-Cell software and the results are found to be in orthorhombic phase with a space group P_{mmm}.

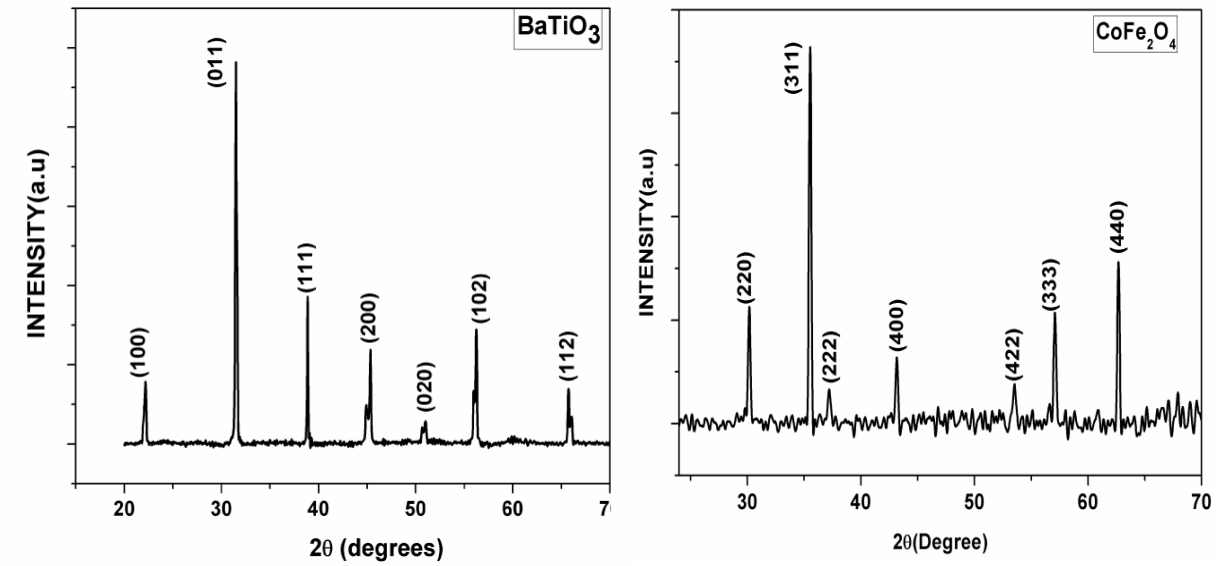

Fig. 4.3.1 (a) XRD graphs of $BaTiO_3$ and $CoFe_2O_4$.

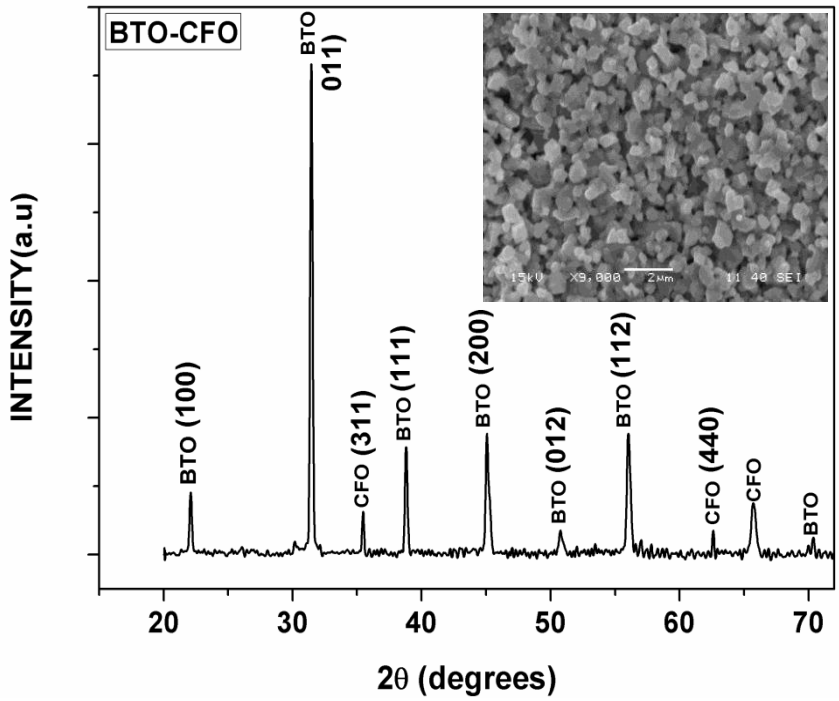

Fig. 4.3.1 (b) XRD graph of $BaTiO_3$-$CoFe_2O_4$ composite.

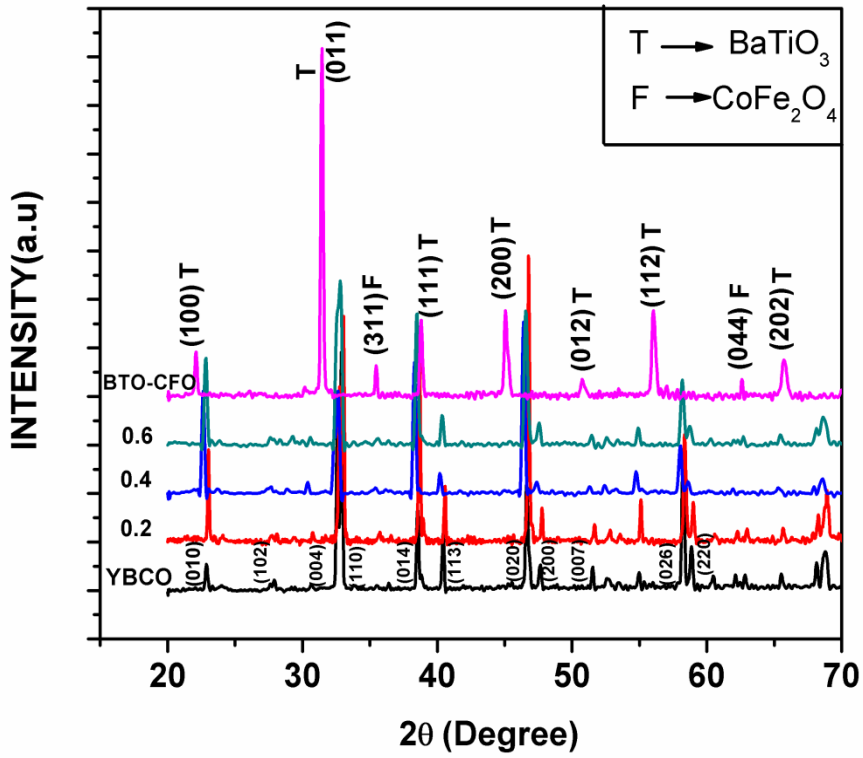

Fig. 4.3.1 (c) XRD graphs of (1-x) YBCO+ x $BaTiO_3$-$CoFe_2O_4$ (x= 0.0, 0.2, 0.4, 0.6) composites.

The inset microstructure graph of BTO-CFO in Fig 4.3.1(b) shows grains with size less than 1μm. The peaks of BTO and CFO are identified as 'T' and 'F' respectively. The major peak (011) of BTO and (311) of CFO have been identified in the composite sample BTO-CFO (Fig

1b). The intensity variation of the sample peaks depends on the phase formation in the composite. The lattice parameters and unit cell volumes of the composite samples are presented in Table 4.3.1.

Table 4.3.1 Lattice parameter of YBCO with different BTO-CFO wt.%

BTO-CFO(wt.%)	a (Å)	b (Å)	c (Å)	V (Å^3)	δ= b-a /b+a
0.0	3.815(1)	3.882(1)	11.683(2)	173.023	0.008
0.2	3.811(2)	3.881(2)	11.665(5)	172.531	0.009
0.4	3.834(1)	3.888(1)	11.719(3)	174.690	0.006
0.6	3.822(1)	3.885(1)	11.690(3)	173.578	0.008

From the tabulated data it is observed that 'b' parameter is not affected by the addition of BTO-CFO. The magnitude of 'a' and 'c' lattice parameters and crystallite volume are greater in the composites as compared to the pristine YBCO, but decreases slightly for low wt.% addition of BTO-CFO. But the orthorhombic distortion (δ) is high in this case which indicates better oxygen ordering. It can also be seen that the lattice parameter c is small for the sample with higher ordering. The smaller c value could be responsible for a better interlayer exchange and consequently, could give better superconducting properties [1].

4.3.2.2. RAMAN analysis of YBCO/ BTO-CFO composite system

Figure 4.3.2 shows Raman spectra of YBCO+ x BTO-CFO (x = 0.0, 0.2, 0.4, 0.6 wt. %) composite samples. It shows the characteristic Raman bands of oxygen. The strong peak of 500 cm^{-1} for y = 7 sifts to the lower frequency side as the oxygen content decreases [2]. All the Raman active vibrational modes are found in our pristine sample. The peak seen at 600 cm^{-1} for all the doped samples is attributed to be of $Ba_2Cu_3O_{5.9}$ [3]. The high frequency, temperature dependent mode (600 cm^{-1}) is expected to be due to a new atomic configuration. The mode appears to be associated with oxygen vibrations.

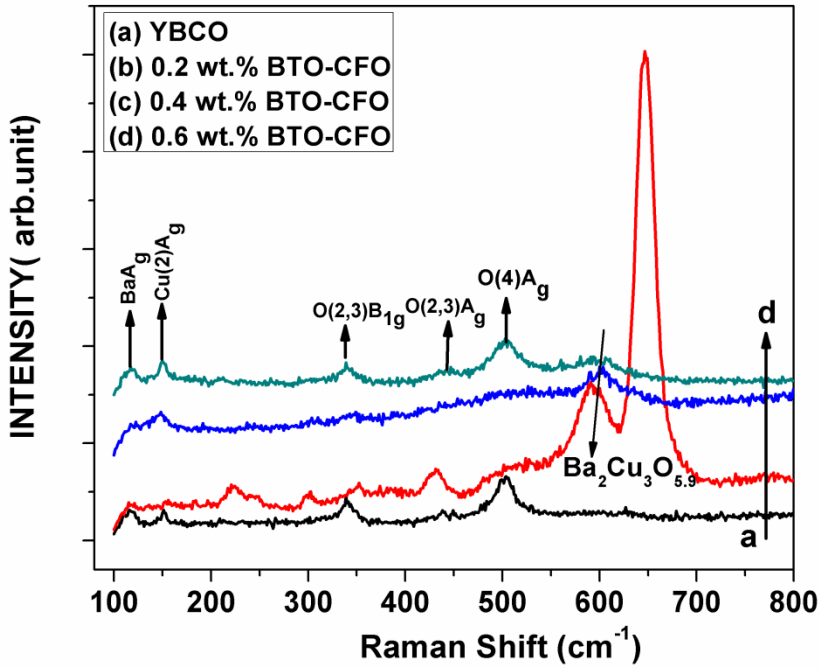

Fig. 4.3.2 Micro-Raman spectra of YBCO + x BTO-CFO Samples (x = 0.0, 0.2, 0.4, 0.6 wt. %) samples.

In YBCO there is a new oxygen occupied site located near the Cu_c-O_c plane. This new position apparently involves a short bond length, possibly O-O, which leads to the high frequency 600 cm^{-1} Raman mode [4]. The peak seen at 300 cm^{-1} for 0.2 wt. % added BTO-CFO sample is due to CuO [5]. The mode at 223 cm^{-1} is due to oxygen depletion and attributed to the vibrations of Cu (1) and O (1) atoms [6]. One prominent peak at 646 cm^{-1} was also seen whose intensity depends on oxygen content and assigned to be normally forbidden vibrations of the Cu (1)-O(1) chains [7]. The 115, 151 and 500 cm^{-1} peaks softens in 0.2 and 0.4 wt. % BTO-CFO added samples.

Table 4.3.2 Oxygen content calculated using XRD and Raman spectra. 'c' is lattice parameter along Z direction, δ is oxygen loss, ν is frequency of apical oxygen.

BTO-CFO (wt. %)	c (A^0)	$O_{7-\delta}$ (from XRD)	ν(cm^{-1})	$O_{7-\delta}$(from Raman)
0.0	11.683(2)	6.85	504	7.02
0.2	11.665(5)	6.90	496	6.81
0.4	11.719(3)	6.60	497	6.84
0.6	11.690(3)	6.70	504	7.02

From the oxygen stoichiometry values of Raman data it is observed that the oxygen content is high in pristine as well as composite samples. It also confirms the orthorhombic nature of the samples.

4.3.2.3. P-E hysteresis loop of $BaTiO_3$-$CoFe_2O_4$ composite

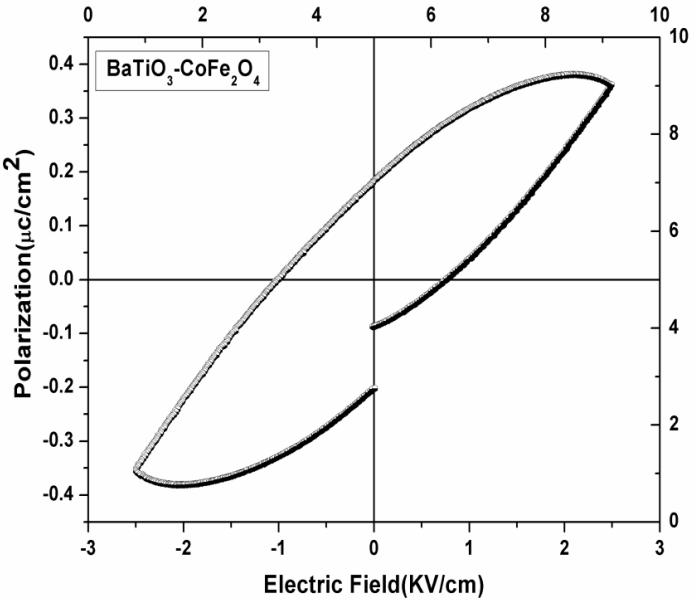

Fig. 4.3.3 P-E hysteresis loop of $BaTiO_3$-$CoFe_2O_4$ composite.

Figure 4.3.3 shows a well-developed and fairly symmetric ferroelectric hysteresis loop for the BTO-CFO composite. The measurement of P-E loop is discussed in the experimental section (2.4.7). It shows the ferroelectric nature of the BTO-CFO composite. From the polarization loop the remnant polarization (P_r) and the coercive field (E_c) are calculated to be 0.18 μCcm^{-2} and 1.03 $kVcm^{-1}$respectively.

4.3.2.4. Microstructural analysis

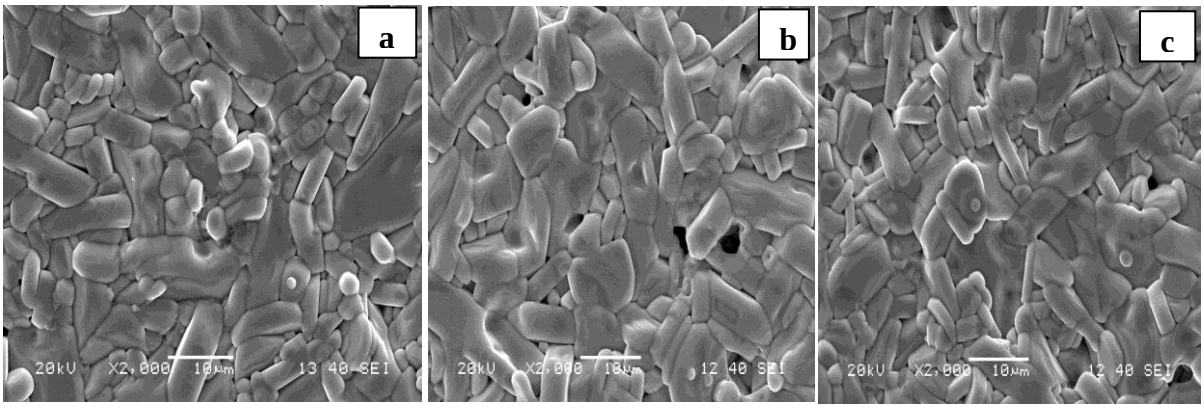

Fig. 4.3.4 SEM micrographs of (1-x) YBCO + x BTO-CFO (x=0.0, 0.2, 0.6 wt. %) samples marked as a, b, c respectively.

The grain size distribution of the pristine and composite samples is shown in figure 4.3.4. It shows that pristine YBCO exhibits closely packed large and elongated grains randomly oriented in all directions. Microstructural view clearly indicates that there is no significant change in the grain size due to the addition of BTO-CFO.

4.3.2.5. Temperature dependence of resistivity

Measurements of the resistivity dependence of temperature for different samples with various amounts of BTO-CFO are shown in figure 4.3.5.

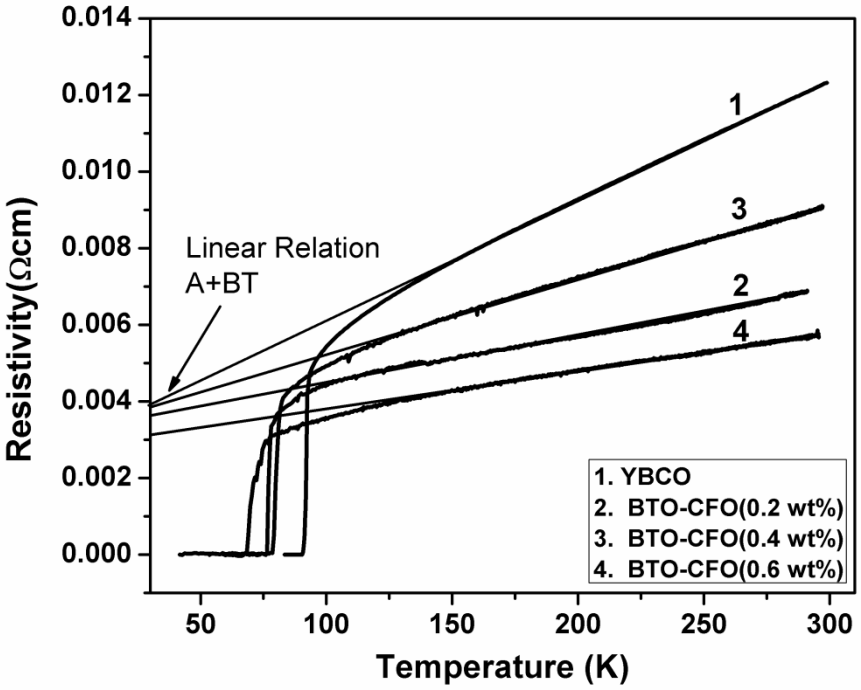

Fig. 4.3.5 Resistivity dependences on the temperature for YBCO+ x BTO-CFO(x= 0.0, 0.2, 0.4, 0.6 wt. %) composites.

The nonlinear region develops due to the increasing contribution of Cooper pair fluctuation to the conductivity above T_c. At T_{c0} the electrical resistivity vanishes and the phase of the order parameter has acquired long range order between the grains of the system. A finite tailing is observed in the superconducting transition for all the composites before the resistance attains zero value. It indicates that the superconducting grains get progressively coupled to each other by Josephson tunneling across the grain boundary weak links. The zero-resistance at the temperature T_{c0}, characterizes the onset of global superconductivity in the samples where the long range superconducting order is achieved. The onset of global superconductivity decreases (fig. 4.3.6) with the addition of BTO-CFO indicating that BTO-CFO adheres to grain boundary forming weak links. Thus, it is suggested that the added inhomogeneity probably

acts as a weak link, which causes the global resistivity transition temperature to decrease. The added BTO-CFO reduces the normal state resistivity (Table 4.3.3).

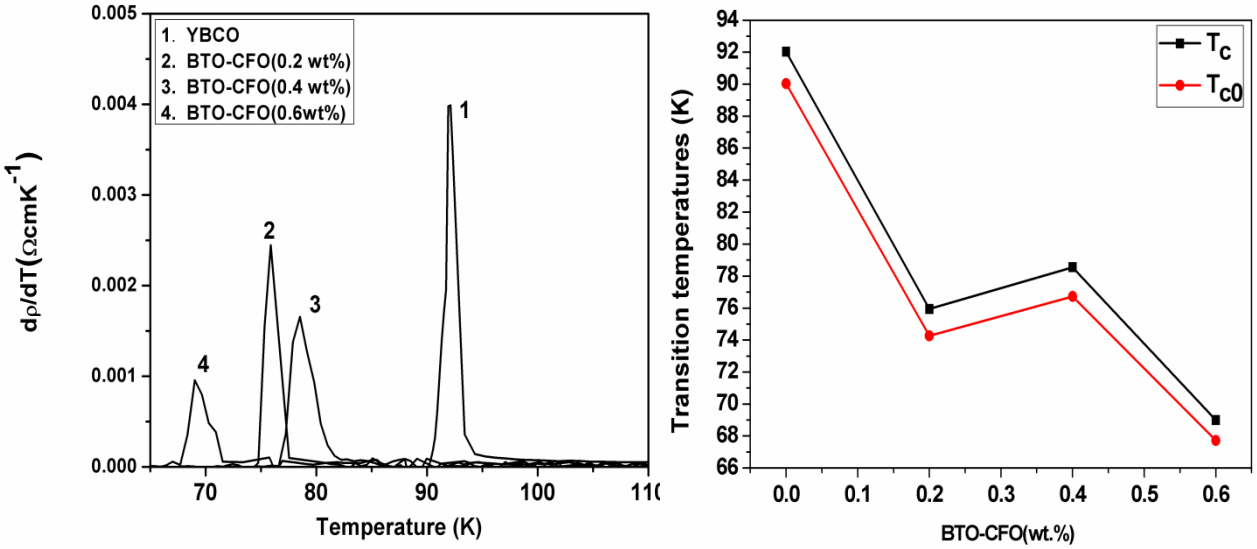

Fig. 4.3.6 Temperature derivative of resistivity for (1-x) YBCO + x BTO-CFO composites (x = 0.0, 0.2, 0.4, 0.6 wt. %).

The sharp peak in the temperature derivative of resistivity plots (fig 4.3.6) denotes the superconducting transition temperature T_c, which is related to intra-granular fluctuation [8]. With increase in inhomogeneity content peak broadening occurs, affecting the inter-granular percolation of Cooper pairs in YBCO matrix. The transition width (ΔT_c) defined as full width half maxima increases with doping concentration.

Table 4.3.3 Variation of normal state and superconducting parameters in the composites with different BTO-CFO wt. %.

BTO-CFO(wt.%)	T_{c0}(K)	T_c(K)	ΔT_c(K)	ρ_{290K}(μΩ.cm)	ρ_{wl}(μΩ.cm)	α_n	$\rho_n(0)$(μΩ.cm)
0.0	90.51	92.02	1.5	12060	49.00	0.016	3120
0.2	74.27	75.94	1.7	6000	120.90	0.039	3100
0.4	76.73	78.55	2.3	8000	89.44	0.026	3440
0.6	67.71	68.99	1.8	5000	144.84	0.051	2840

The increasing value of ρ_{wl} and the decreasing trend in the value of zero-resistance critical temperature (T_{c0}) indicates that the connectivity between grains decreases gradually with the addition of magneto-electric (ME) in-homogeneity, BTO-CFO. The increasing value of ΔT_c

signifies the degradation of sample quality in the composites. All these effects are due to increased in-homogeneities in the inter-granular regions.

4.3.2.6. Dimensionality fluctuations of excess conductivity

The excess conductivity has been analyzed in the light of Aslamazov-Larkin (AL) model and the dimensionality of fluctuation has been found out. The excess conductivity plots are shown in Fig.4.3.7. In order to explain the experimental data with theoretical predicted ones, the different regions of the plot were linearly fitted and the exponent values were determined from the slopes. The plot reveals three distinct regimes i.e. mean-field or the Gaussian fluctuations, critical fluctuations and short wave fluctuation region.

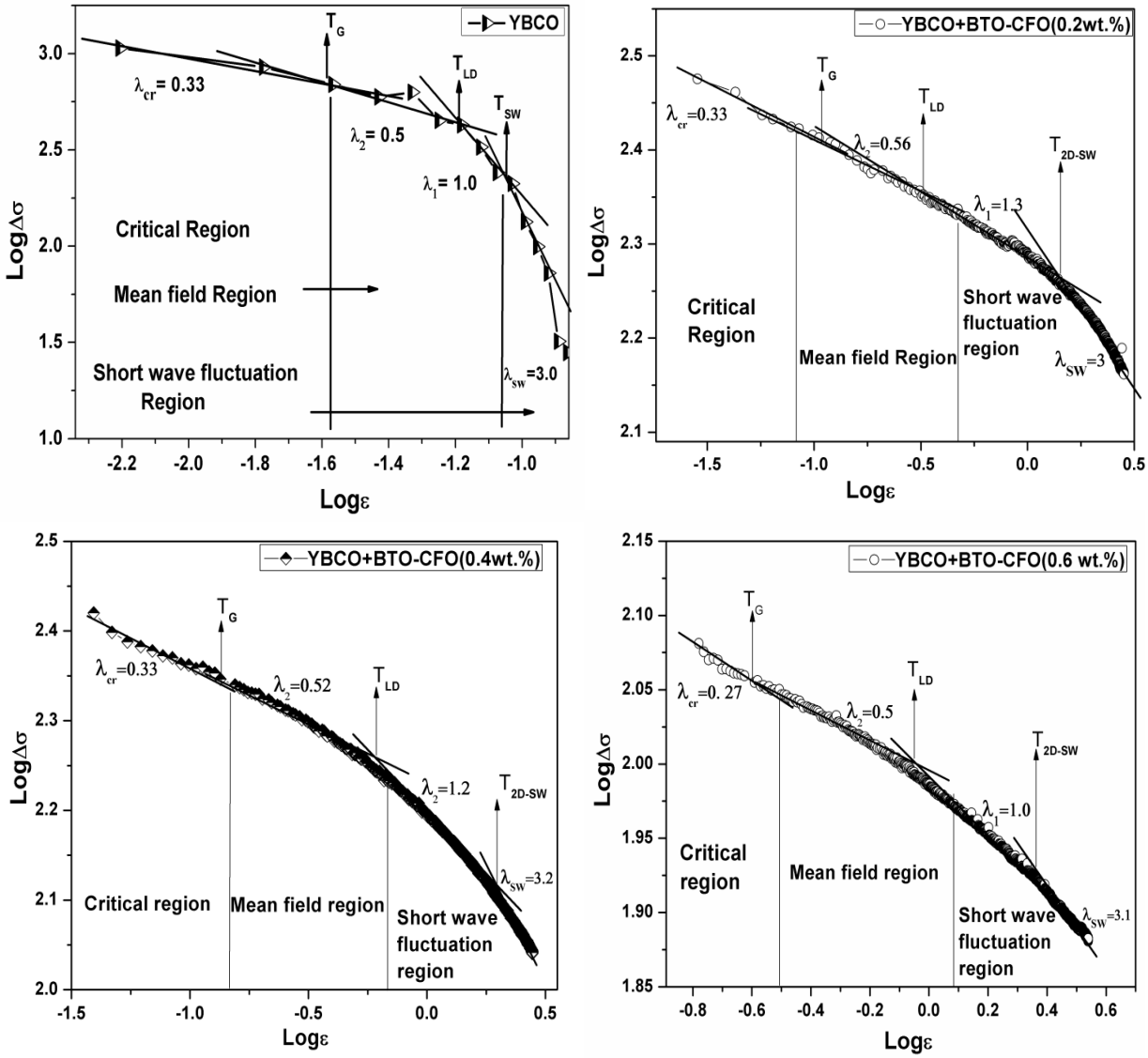

Fig. 4.3.7 Log-Log plot of excess conductivity $\Delta\sigma = 1/\rho - 1/\rho_R$ as a function of reduced temperature $\epsilon = (T-T_c)/T_c$ in (1-x) YBCO+ x BTO-CFO composite.

Table 4.3.4 The parameters extracted from excess conductivity analysis in YBCO/ BTO-CFO composite.

BTO-CFO (wt. %)	λ_{cr}	λ_1	λ_2	λ_{swf}	T_G (K)	T_{LD} (K)	$T_{2D\text{-}SW}$ (K)
0.0	0.33	1.0	0.50	3.0	112.52	130.68	140.80
0.2	0.33	1.3	0.56	3.0	105.60	123.21	164.16
0.4	0.33	1.2	0.52	3.2	110.91	130.84	173.18
0.6	0.27	1.0	0.50	3.1	104.26	122.07	163.91

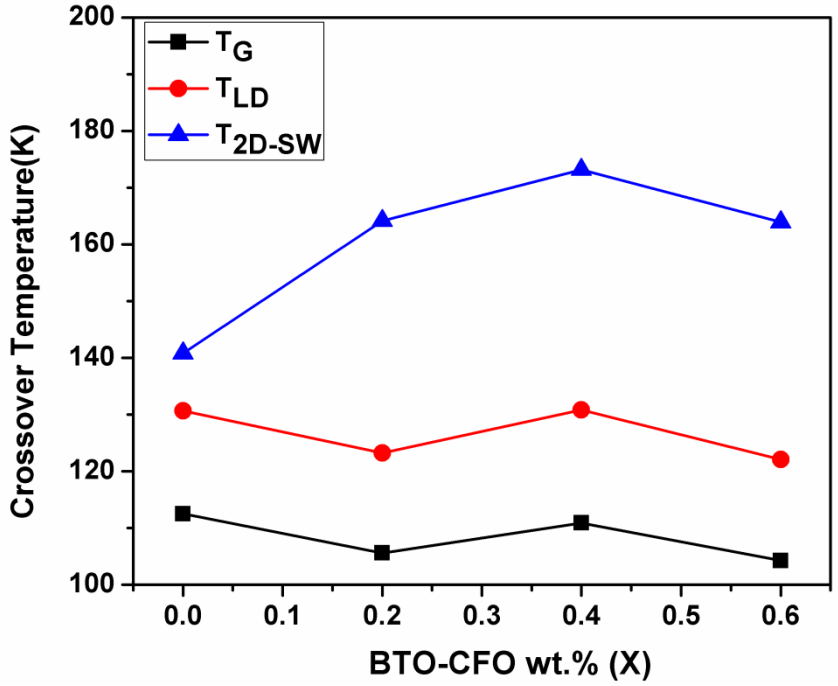

Fig. 4.3.8 Variation of cross-over temperatures with BTO-CFO wt. %.

In the log-log plot of the excess conductivity vs. the reduced temperature, different λ values or the exponents for different fluctuation regions above and below the crossover temperature has been observed (Table 4.3.4). The regime that is close to T_c in the mean field region has 3D type of fluctuations but at temperature T_{LD} there is a cross over from 3D to 2D region of fluctuations. As we move to higher temperature side the superconducting fluctuations follow $1/\varepsilon^3$ behavior, such fluctuation region where the Ginzburg-Landau theory breaks down is known as the Short wavelength fluctuations (SWF). It is found that different crossover temperatures decrease with increase in BTO-CFO concentration except for the $T_{2D\text{-}SW}$ which increases in composite samples (fig. 4.3.8). The width of transition between T_{LD}, $T_{2D\text{-}SW}$ increases in composite samples.

4.3.3 Conclusion

This section presents the experimental findings by embedding magneto-electric in-homogeneity BTO-CFO to YBCO. XRD and RAMAN analysis confirms the unchanged orthorhombic structure with the oxygen content remains high in all the pure as well as composite samples. RAMAN graphs show the defect induced modes due to vibrations in Cu (1)-O (1) chains. SEM micrographs reveal the unchanged grain size with the incorporation of ME in-homogeneity in the YBCO matrix. Addition of BTO-CFO accounts for reduction of normal state resistivity and rise of weak-link resistivity with shifting of T_c towards lower temperature zones. The different regions in the excess conductivity plot are the critical region at $T < T_c$, the mean field region at T close to T_c and the short wave fluctuations at $T > T_c$. The excess conductivity data revealed a dimensional crossover from 2D to 3D fluctuation as the temperature is lowered.

4.3.4 References

[1] S. Kurihara, Phys. Rev. B 39 (1989) 6600.

[2] A. Yamanaka, F. Minami, K. Watanabe, K. Inoue, S. Takenaka and N. lyi, Jpn. J. Appl. Phys. 26 (1987) L1404.

[3] H. Chang, Y.T. Ren, Y.Y. Sun, Y.Q. Wang, Y.Y. Xue, C.W. Chu, Physica C 252 (1995) 333.

[4] G. Burns, F. H. Dacol, C. Feild, and F. Holtzberg, Solid state Communications 75 (1990) 893.

[5] I. Nedkov, Supercond. Sci. Tech. 11 (1998) 21.

[6] V.G. Ivanov, M.N. Iliev, C. Thomsen, Phys. Rev. B 52 (1995) 13652.

[7] S. Blumenroder, E. Zirngiebl, H. Schmidt, G. Guntherodt, H. Brenten, Solid state commu 64 (1987) 1229.

[8] J. Roa-Rojas et al., Phys. Rev. B 61 (2000) 12457.

Chapter 5

Study of Structure and Electrical Transport property in Ti doped $YBa_2Cu_3O_{7-\delta}$ system

5. STUDY OF STRUCTURE AND ELECTRICAL TRANSPORT PROPERTY IN Ti DOPED $YBa_2Cu_3O_{7-\delta}$ SYSTEM

5.1 INTRODUCTION

In the present chapter we analyze the mechanism of charge transfer in YBCO when its charge reservoir layer is perturbed due to doping. Fluctuations in the superconducting order parameter develop due to the short coherence length, high transition temperature and anisotropy of the system. Presence of structural and stoichiometric in-homogeneities produced in the system due to doping of foreign material effects the amplitude of the thermal fluctuation and hence the mean field region is got suppressed. Doping at the Cu site of YBCO has significantly influence the structure and the excess conductivity region as well as the tailing region, as Cu-O networks play a major role for the occurrence of superconductivity in these materials. Here we discuss some of our recent results on modification of structure, microstructure and superconducting properties due to microscopic and mesoscopic in-homogeneities in $YBa_2(Cu_{1-x}Ti_x)_3O_{7-y}$ (x= 0.01,0.02,0.04,0.05) doped superconductor.

5.2 ROLE OF Ti IN $YBa_2Cu_3O_{7-\delta}$ SUPERCONDUCTORS

The superconducting phase in all the cuprates has common features of type-II superconducting behavior. The layered structure of HTSC with complex crystal chemistry and the inherent granularity lead to strong structural disorder at the microscopic and the mesoscopic levels [1]. The critical temperature increases with the doping up to some point known as the optimal doping point. Increasing the doping concentration beyond the optimal value, results in reduction of T_c. The doping regimes below and above the optimal doping are known as the under-doped and over doped-regimes respectively.

The valence state of Ti^{4+} is higher than that of Cu^{2+} and substitution of Ti for Cu may increase the mobile carrier concentration due to hole filling effect of Ti [2]. Therefore, it is of interest to investigate the effect of semiconducting and 3d transition element Ti substitution for Cu in YBCO as they have similar electronic configuration and ionic sizes as Cu [2]. It has been reported that for 1 to 5 % doping of Ti caused a decrease of transition temperature where as 7 to 10 % doping caused a slight increase of transition temperature in YBCO [3]. Also small amount of titanium doping decreases the ‘a’ and ‘b’ lattice parameters, whereas ‘c’ does not depend on titanium doping. Excess titanium addition increases a, b and c lattice parameters [4]. Reported results also showed that Ti doping did not improve the weak-link

behavior of the superconducting grains and the critical temperature T_c. But the normal state resistivity is low in comparison to the pristine sample in low percentage addition of TiO_2 with grain size reduced [5].

5.3 EXPERIMENTAL DETAILS AND INTERPRETATION OF RESULTS

5.3.1 Synthesis and characterization of $YBa_2 (Cu_{1-x}Ti_x)_3 O_{7-y}$

A series of polycrystalline samples of $YBa_2 (Cu_{1-x}Ti_x)_3 O_{7-y}$ (x = 0.01,0.02,0.04,0.05) and pristine YBCO has been prepared by the standard solid-state reaction route as described in chapter 2 (section 2.2.7). All the samples were characterized by XRD, RAMAN and SEM techniques. DC electrical resistivity measurement was done by four probe setup connected by a Nanovoltmeter (Keithley-2182A) and constant current source (Keithley-6221). Low temperature was achieved by closed cycle helium refrigerator. Data acquisition was carried out by a computer controlled automated program.

5.3.2 Phase formation of $YBa_2(Cu_{1-x}Ti_x)_3O_{7-y}$ system

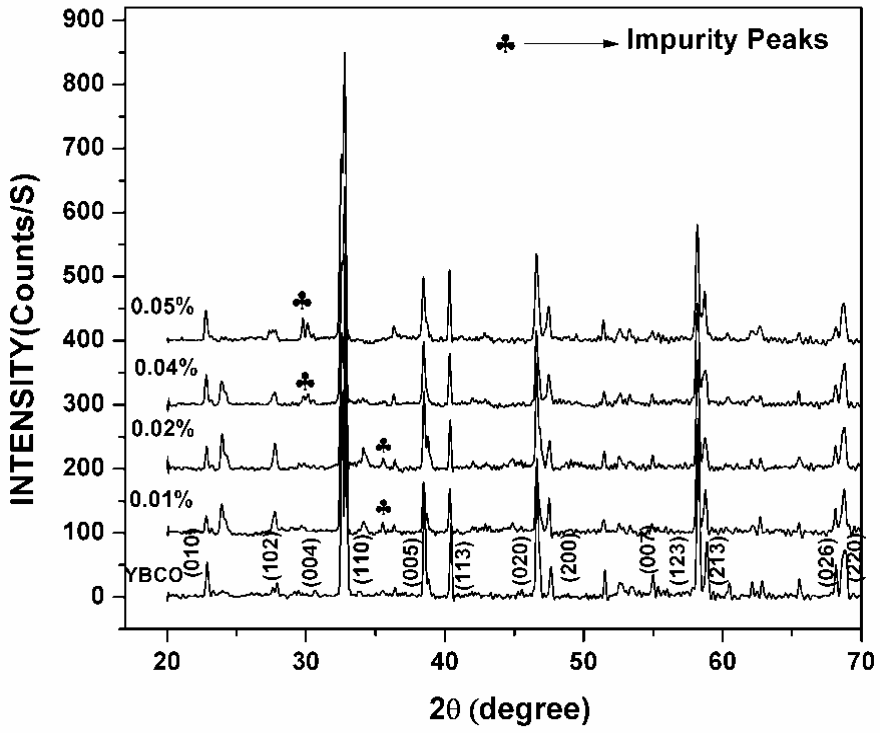

Fig. 5.1 XRD Patterns of YBCO and $YBa_2(Cu_{1-x}Ti_x)_3O_{7-\delta}$ (x = 0.01,0.02,0.04,0.05) samples.

Figure 5.1 shows the X-ray diffraction patterns of the pristine and doped samples. The diffraction pattern is indexed using Chekcell software and the results are found to be in

orthorhombic phase with space group P_{mmm} and some impurity peaks. The lattice parameters and unit cell volumes of these samples are tabulated in Table 5.1.

Table 5.1 Lattice Parameters calculated from XRD graphs

TiO_2%	a(Å)	b(Å)	c(Å)	V($Å^3$)	δ= b-a /b+a
0.00	3.815(1)	3.882(1)	11.683(2)	173.023	0.008
0.01	3.823(1)	3.880(1)	11.693(3)	173.445	0.007
0.02	3.824(1)	3.888(1)	11.683(3)	173.699	0.008
0.04	3.822(1)	3.884(1)	11.687(4)	173.489	0.008
0.05	3.826(1)	3.879(1)	11.691(4)	173.506	0.006

Tabulated data clearly shows that 'b' parameter remains unchanged due to doping but for highest percentage doping it decreases slightly. The length of 'a' parameter lengthens little bit with doping but it almost remains constant for all the doped samples. The 'c' parameter increases in low and high percentage doping level. Crystallite volume is large in the doped samples as compared to the pristine. This variation is expected due to the non-uniform elastic distortions of the crystal lattice at the atomic level imposed by Ti on YBCO matrix. As the ionic radius of Ti (0.605Å) is smaller than Cu (0.73Å) it may fully substituted for the Cu site. The orthorhombic distortion remains almost constant except 0.01 wt. % and 0.05 wt. % doped sample. Greater value of δ signifies improved oxygen ordering. Superconducting nature of YBCO is associated not only with the oxygen content but also depends upon their ordering and oxygen vacancies in the Cu-O basal plane. The complete ordering is reflected in rows of empty O (5) and filled O (1) sites. This asymmetric distribution of oxygen leads to an orthorhombic distortion (b-a / b+a), which is a measure of ordering [6]. Lattice parameter 'c' is smaller for the sample with higher ordering. The smaller c value could be responsible for a better interlayer exchange and consequently, could give better superconducting properties [7]. The oxygen stoichiometry value is calculated from the relation 7-y =75.250-5.856c (shown in Table 5.2) where c is the c-axis lattice parameter [8]. From the data it is clear oxygen value is not affected by doping. As we know that if the substitution takes place on Cu (2) site, there is no observed structural O-T transition i.e. the structure remains orthorhombic even for higher dopant concentrations and oxygen order in the CuO chains remains intact. As 'Ti' has similar electronic configuration as that of Cu, it substitutes preferentially at the Cu (2) site. From the

values of δ and O_{7-y} it is also clear that the structure remains orthorhombic and there is an improved oxygen ordering.

5.3.3 Raman spectroscopy of $YBa_2(Cu_{1-x}Ti_x)_3O_{7-y}$ system

Raman spectroscopy is a characterization method that measures the frequencies of the long-wavelength lattice vibrations (phonons). Figure 5.2 shows the Raman spectra of YBCO and $YBa_2(Cu_{1-x}Ti_x)_3O_{7-\delta}$ (x = 0.01,0.02,0.04,0.05) samples. Generally a perovskite YBCO unit cell has five different oxygen sites which get activated under the influence of photons. They are O(1) in CuO chains, O(2,3) in CuO_2 planes, O(4) in the apical chains and O(5) lies in between the oxygen chains which is empty in orthorhombic structure. The active vibration along the c axis is shown at peak position 500 cm^{-1}, 432 cm^{-1}, 339 cm^{-1}.

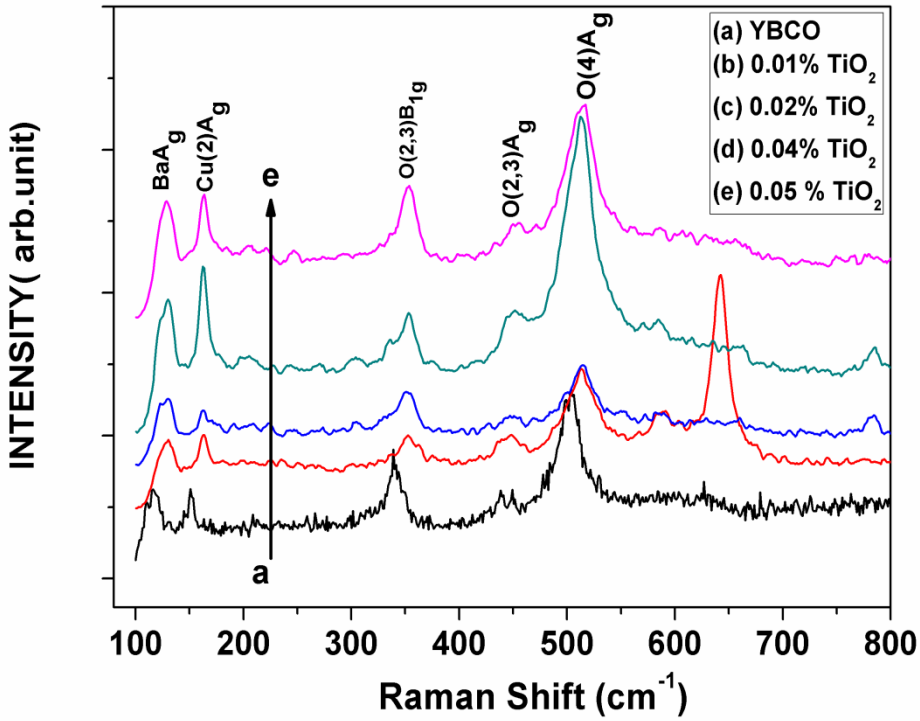

Fig. 5.2 Micro-Raman spectra of YBCO and $YBa_2(Cu_{1-x}Ti_x)_3O_{7-\delta}$ (x = 0.01,0.02,0.04,0.05) samples.

The 500 cm^{-1} represents the stretching of apical oxygen or the bridging oxygen O(4) denoted as $O(4)A_g$. 432 cm^{-1} represents the in phase vibration of O(2)-O(3) oxygen atom in CuO_2 plane marked as $O(2,3)A_g$ and 339 cm^{-1} represents out-of-phase c-axis vibration of O(2)-O(3) oxygen atom in CuO_2 plane labeled as $O(2,3)\ B_{1g}$ [9-12]. The other two Raman active modes are vertical along the c-axis given by Cu (2) atoms. 151 cm^{-1} denoted as Cu (2) A_g i.e. plane Cu in phase and 115 cm^{-1} denotes the Ba vibration marked by BaA_g. The strong peak of 500 cm^{-1} shifts to the lower frequency side as the oxygen content decreases. In addition, the 115 cm^{-1} peak disappears for 7-y= 6.2 [13, 14].

All the standard vibrational modes are found in our experimental pristine as well as doped samples. The peak seen at 588, 643, 785 cm^{-1} in the doped samples belong to additional defect-induced modes caused by oxygen disorder in the O(1) or O(4) sites [15,16]. The sifting and broadening of the peaks $O(4)A_g$, $O(2,3)A_g$ and $O(2,3)B_{1g}$ clearly demarcates the structural changes occurred due to incorporation of doped Ti into YBCO matrix. All the vibrational modes gradually harden with increase in dopant concentration. Generally the O(4) phonon mode is associated with the oxygen content (y). Huong et al. proposed the following relationship between oxygen content and the peak frequency of the O(4) mode [17],

$$y = 13.58 - 0.027\nu$$

Where ν is the peak frequency of the O(4) mode.

Table 5.2 shows the oxygen content (y) evaluated using frequency of Raman mode and the c axis from XRD. It clearly indicates that oxygen value remains high in all the pure as well as doped samples.

Table 5.2 Oxygen content calculated using XRD and Raman spectra. 'c' is the lattice parameter along Z direction, y is oxygen loss, ν is the frequency of apical oxygen.

TiO_2 %	c (Å)	O_{7-y} (from XRD)	ν(cm^{-1})	O_{7-y} (from Raman)
0.0	11.683(2)	6.8	504	7.0
0.01	11.693(3)	6.7	514	7.2
0.02	11.683(3)	6.8	514	7.2
0.04	11.687(4)	6.8	513	7.2
0.05	11.691(4)	6.7	516	7.3

5.3.4 Morphological outlook of $YBa_2(Cu_{1-x}Ti_x)_3O_{7-y}$ system

The grain size distribution of the pristine and doped samples is shown in figure 5.3. It shows that pristine YBCO exhibits large and elongated grains randomly oriented in all directions. With increase in TiO_2 concentration the grain size decreases slightly up to 0.04 wt.%. For 0.05 % TiO_2 addition the grain size decreases significantly as compared to the pristine sample.

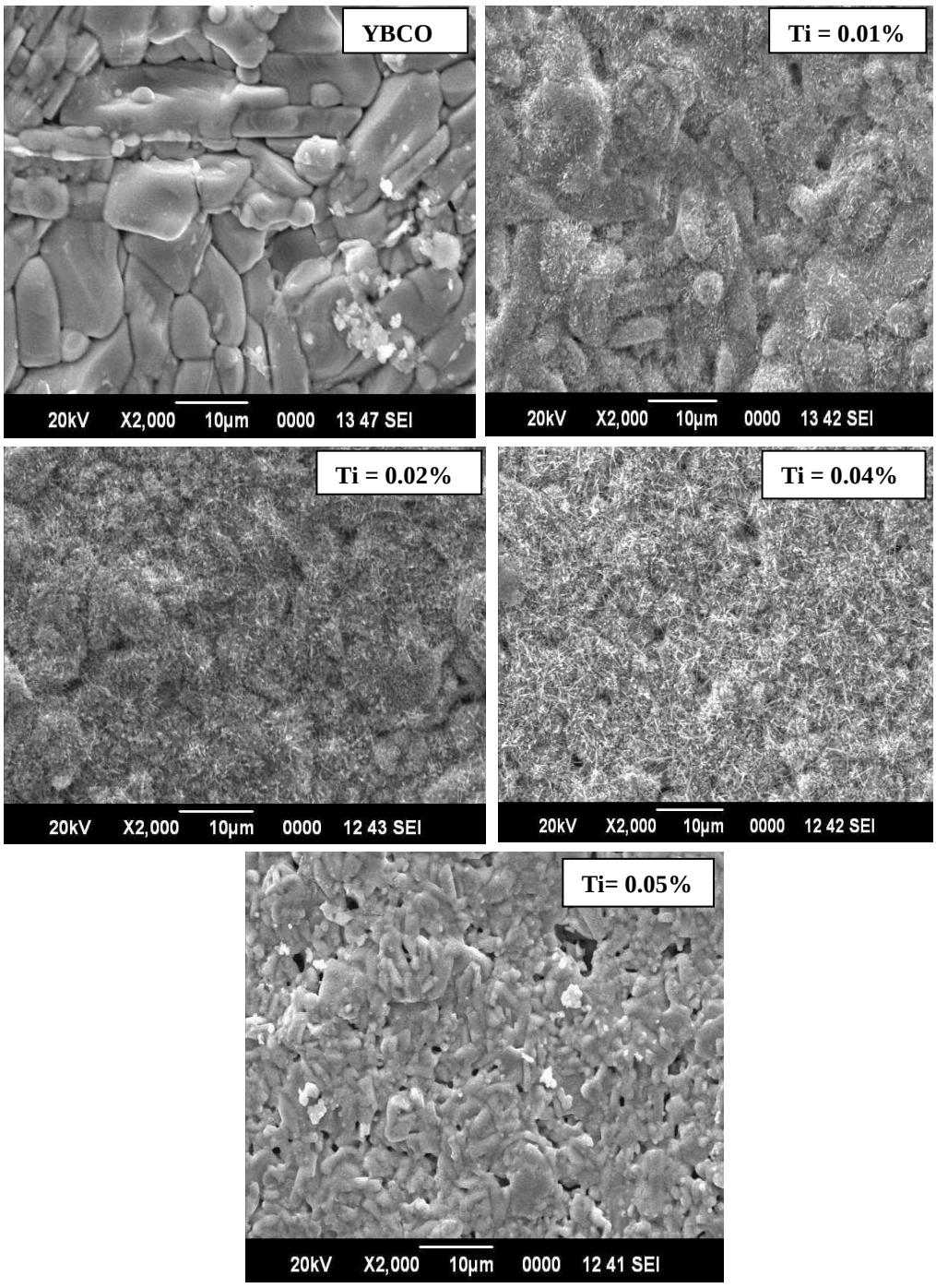

Fig. 5.3 SEM micrographs of YBCO and $YBa_2(Cu_{1-x}Ti_x)_3O_{7-\delta}$ (x = 0.01,0.02,0.04, 0.05) samples.

Decrease in grain size indicates that the strength and hardness increases in Ti doped samples. This behaviour can be attributed to a reduction in the amount of liquid phase in samples during the growth process [3]. Generally the ceramic samples are crystalline in nature and contain grain boundaries. When the sample is processed the atoms within each growing grain are lined up in a specific pattern, depending on the crystal structure of the sample. During the growth process, each grain will impact others and form an interface where the atomic orientations differ. The strength and hardness of ceramic samples vary as the inverse square

root of grain size [18]. From the microstructural analysis, it is clear that TiO_2 not only decrease the grain size but also degrade the grain connectivity and increase the cracks and voids between grains. The net like structures covering the surface of YBCO grains are expected as the TiO_2 nanowires. These nanowires are absent in the highest Ti doped sample i.e. 0.05 %. They might have gone inside the grains and brought changes in the structural property. The EDX graph in figure 5.4 shows that all the compositional elements are present in the pristine and doped samples.

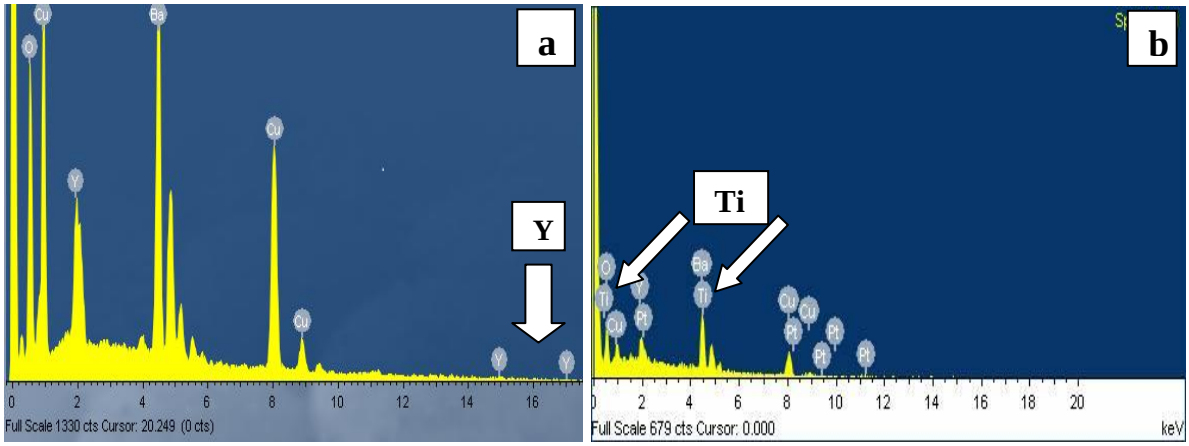

Fig. 5.4 EDX graphs of YBCO and 0.01% Ti doped samples marked as a and b respectively.

5.3.5 Temperature dependence of resistivity of $YBa_2(Cu_{1-x}Ti_x)_3O_{7-y}$ system

Figure 5.5 shows the temperature dependence of resistivity measurements with various amounts of TiO_2. The first region of the resistive transition is characterized by the normal state which shows a metallic behavior (above $2T_c$). The normal state resistivity obeys Anderson and Zou relation $\rho_n(T) = A+BT$. The $\rho_n(T)$ value is calculated by using the values of A and B parameters, which are obtained from the linear fitting of resistivity in the temperature range $2T_c$ to 300 K and extrapolated to 0 K gives resistivity slope ($d\rho/dT$) and residual resistivity ρ_0 respectively. In the second region ρ (T) is deviated from linearity behavior due to the contribution of Cooper pairs to the conductivity below T_c. This is mainly due to the increasing rate of Cooper pair formation on decreasing the temperature. Therefore, the fluctuation induced conductivity in this region follows the AL model to obtain the dimensional exponents of fluctuation conductivity. At the temperature value T_{c0} the electrical resistivity vanishes and the phase of the order parameter acquire long range order between the grains of the system. This critical temperature signifies the coherence transition.

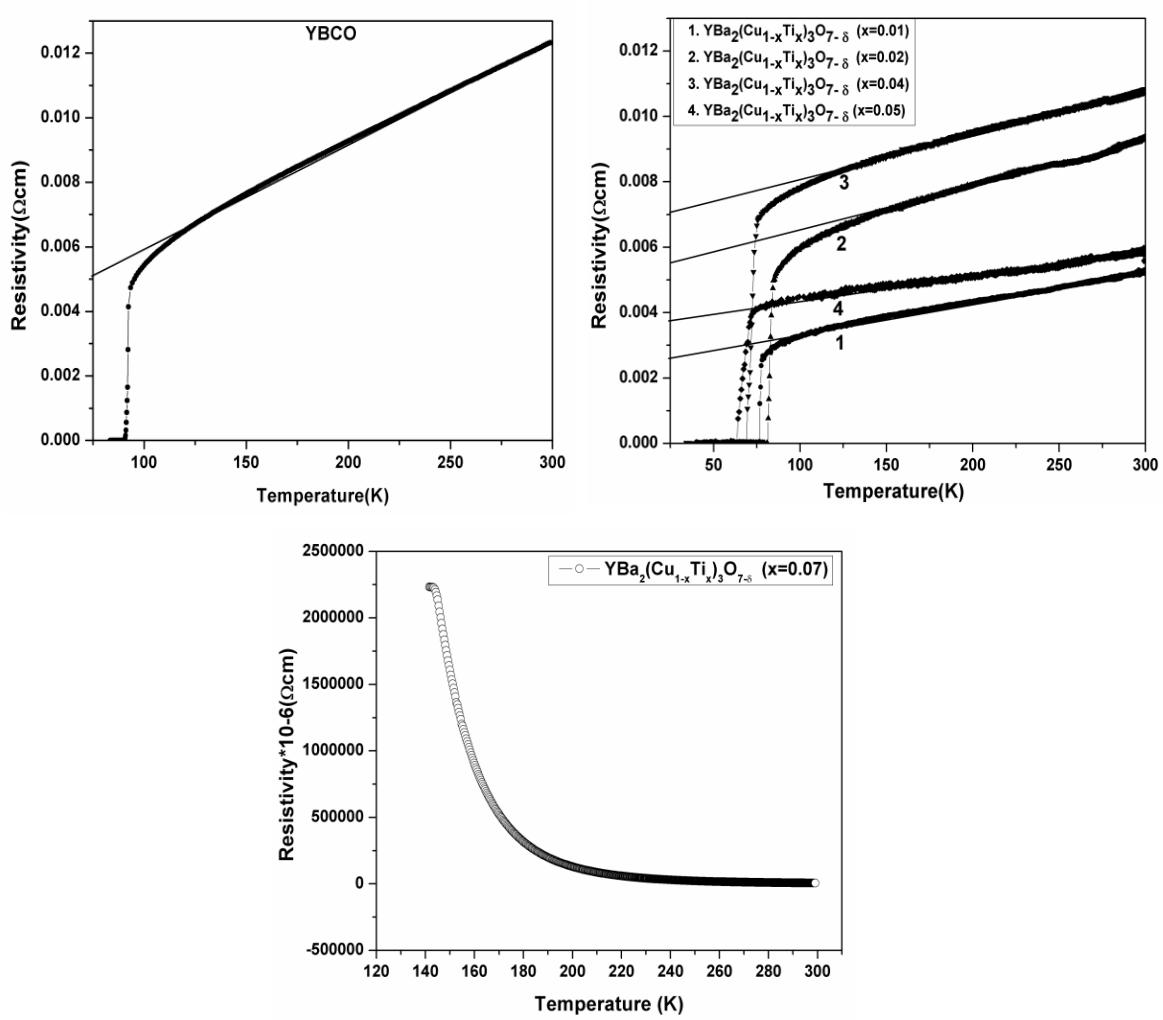

Fig. 5.5 Temperature dependent resistivity of YBCO and $YBa_2(Cu_{1-x}Ti_{-x})_3O_{7-\delta}$(x= 0.01, 0.02, 0.04, 0.05, 0.07) samples.

Before the resistance attains zero value, a tail like region is observed for all the samples in the superconducting transition. It indicates that the superconducting grains get progressively coupled to each other by Josephson tunneling across the grain boundary weak links. The zero-resistance at the temperature T_{c0}, characterizes the onset of global superconductivity (where all the grains becomes superconducting i.e. intra-grain as well as grain boundaries becomes superconducting) in the samples where the long range superconducting order is achieved. The onset of global superconductivity decreases with addition of TiO_2 indicating that it adheres to grain boundary forming weak links. At 0.07 % addition of TiO_2 a purely semiconductor type behavior was observed.

Temperature derivative of resistivity graphs (Fig 5.6) shows a sharp peak at T_c, which is related to intra-granular fluctuation [19]. The temperature value corresponding to this maximum peak is close to the bulk critical temperature value T_c followed by hump or secondary peak which broadens for composite samples. The transition width (ΔT_c) defined as full width half maxima increases with doping concentration. This may be due to the gradual occurrence of non-superconducting additional phases and the effect of microscopic in-homogeneity. The observed lowering of T_c with increasing Ti provides convincing evidence that the hole concentration decreases as the samples are doped with higher concentrations of Ti^{4+} for Cu^{2+}. The additional electrons contributed by Ti ions are expected to fill mobile holes in the CuO_2 planes, thereby reducing conduction and suppresses superconductivity [2].

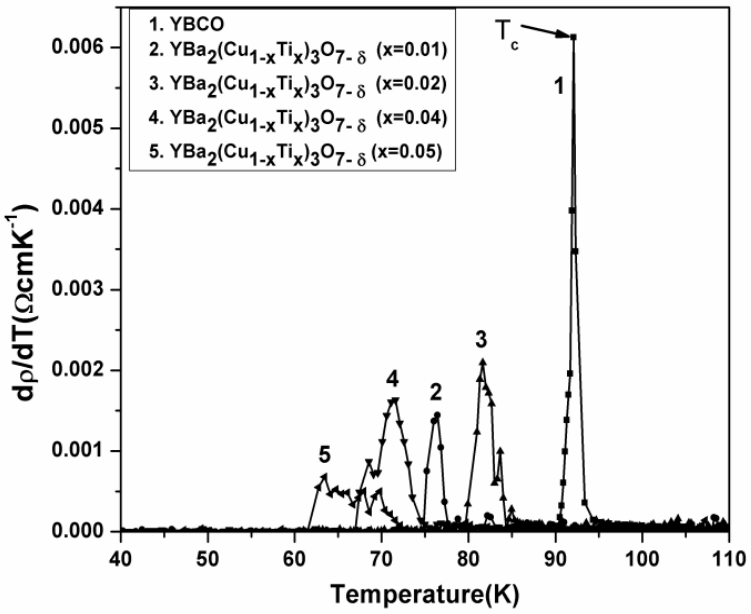

Fig. 5.6 Temperature derivative of resistivity of YBCO and $YBa_2(Cu_{1-x}Ti_x)_3O_{7-\delta}$ (x = 0.01, 0.02, 0.04, 0.05) samples.

Table 5.3 Variation of normal state and superconducting parameters in the doped samples

TiO_2 %	T_{c0}(K)	T_c(K)	ΔT_c(K)	α_n	$\rho_n(0)$ (μΩ.cm)	ρ_{wl} (μΩ.cm)	ρ_P(μΩ.cm)	α_{str}
YBCO	90.24	92.04	1.80	0.016	3100	49.6	1033	0.04
0.01	74.70	76.33	1.63	0.0544	2490	135.456	830	0.16
0.02	79.59	81.73	2.14	0.0350	5000	175.000	1666	0.10
0.04	68.64	71.70	3.06	0.0385	6890	265.265	2296	0.11
0.05	61.29	63.44	2.15	0.0671	3630	243.573	1210	0.20

The percolation factor 'α_n' (shown in Table 5.3) arising due to current frustration caused by misalignment of anisotropic grains and sample defects such as voids and cracks are estimated from the temperature coefficient of resistivity dρ/dT. This factor contributes to percolative conduction in granular copper oxides. Various normal state and superconducting parameters are calculated by using the formula as discussed in chapter 3.

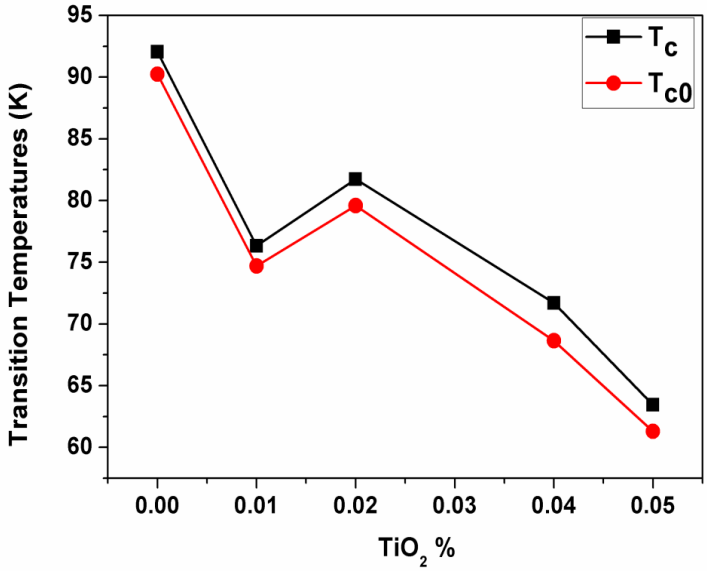

Fig. 5.7 Variation of transition temperatures with various TiO_2 percentage.

A decreasing trend was seen in the value of T_{c0} and T_c with increase in titanium percentage (fig 5.7). The normal state resistivity is less in comparison to the pure sample in low percentage addition of TiO_2. All the granular parameters like α_n, ρ_{wl}, ρ_p, α_{str} were found to lie in their ideal range.

5.3.6 Dimensionality of fluctuations in $YBa_2(Cu_{1-x}Ti_x)_3O_{7-y}$ system

Figure 5.8 displays the logarithmic plot of excess conductivity as a function of reduced temperature (ε). Different regions of the plot are linearly fitted and the exponent values are determined from the slopes. The thermal fluctuations in HTSC give a finite probability of the formation of Cooper pairs which results excess conductivity during the transport of carriers [20, 21]. While approaching from higher temperature side, the fluctuations have the characteristic of a quasi-1D and quasi-2D geometries, but close to T_c, a crossover occurs to homogeneous 3D Gaussian fluctuations. The short coherence lengths of the high T_c cuprate superconductors produce a significant rounding of the transition curve, which provides for the possibility to study fluctuating superconducting pairs over an extended temperature region above the transition temperature T_c. Such studies are of interest and give estimates of

microscopic parameters such as the coherence lengths, phase breaking time and dimensionality of the order parameter [22].

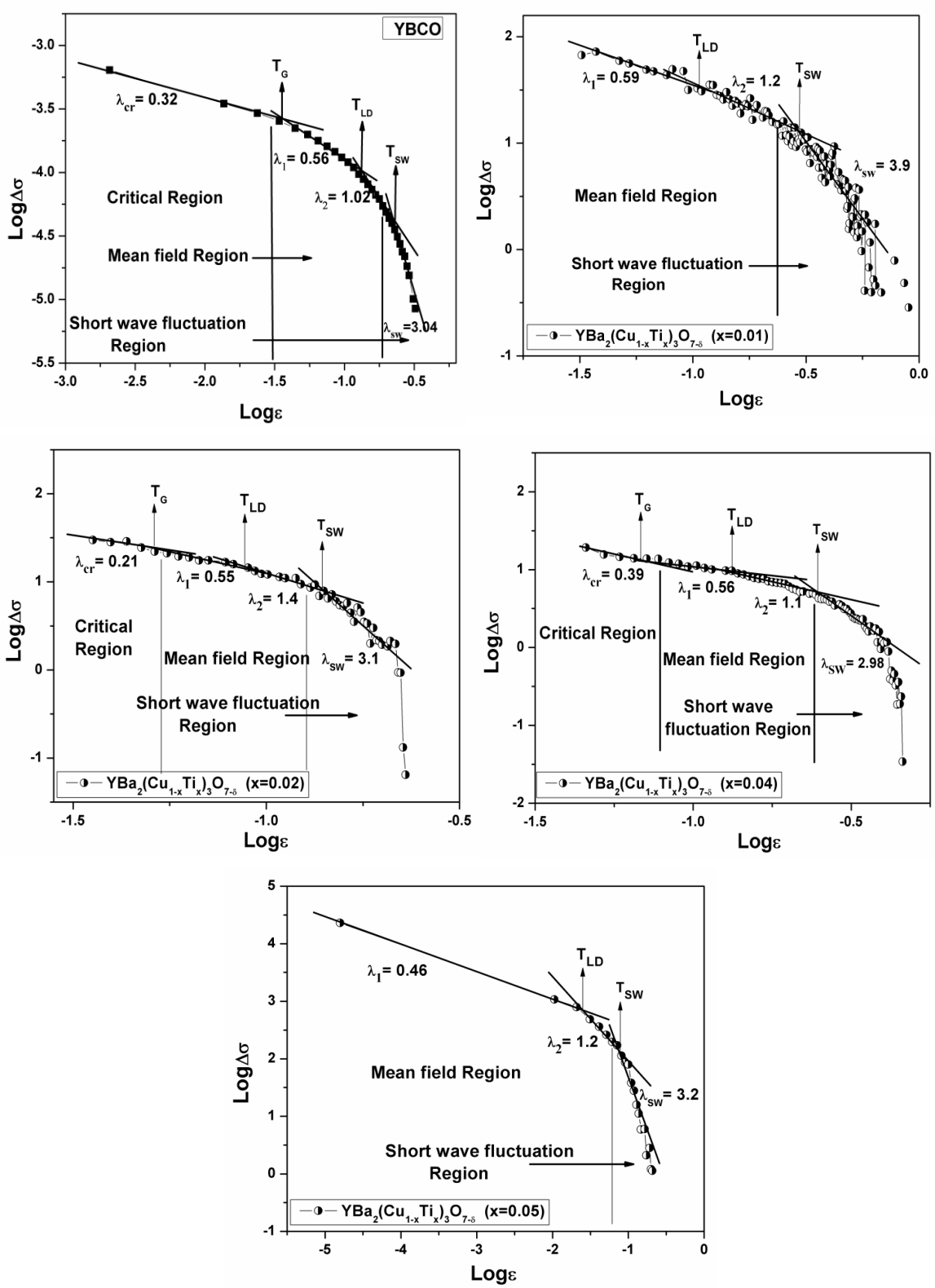

Fig. 5.8 Log-Log plot of excess conductivity $1/\rho - 1/\rho_R$ as a function of reduced Temperature $\epsilon = (T-T_c)/T_c$ in YBCO and $YBa_2(Cu_{1-x}Ti_x)_3O_{7-\delta}$ (x = 0.01,0.02,0.04,0.05) samples.

Enhancement in conductivity is explained on the basis of Aslamazov and Larkin theory as described in chapter 3. Attempts have been made to ascertain the dimensionality of the fluctuations and probe the dimensionality cross over when the system approaches the 3D superconducting state. The intra-grain modification either due to crystallographic or morphologic changes is characterized by various crossover temperatures in the SCOPF region.

Table 5.4 TiO_2 content dependence of different cross over temperatures (Ginzburg-Landau, Lawrence–Doniach and Shortwave fluctuation)

TiO_2 %	λ_{cr}	λ_1	λ_2	λ_{swf}	T_G(K)	T_{LD}(K)	T_{SW}(K)
YBCO	0.32	0.56	1.02	3.0	113.43	129.99	140.02
0.01	--	0.59	1.2	3.9	---	105.18	121.13
0.02	0.21	0.55	1.4	3.1	104.28	109.59	116.22
0.04	0.39	0.56	1.1	2.9	94.78	101.31	110.77
0.05	--	0.46	1.2	3.2	---	75.87	84.12

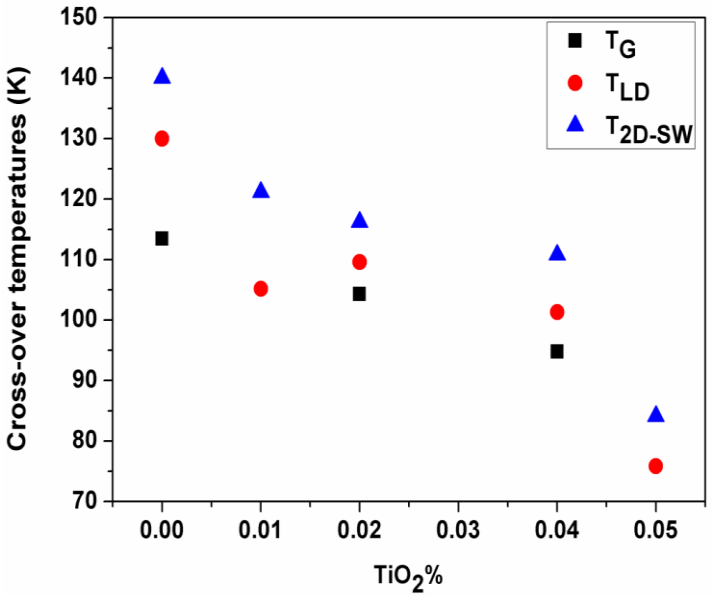

Fig. 5.9 Variation of different crossover temperatures with titanium percentage.

In the log-log plot of the excess conductivity vs reduced temperature, different λ values or the exponents for different fluctuation regions above and below the crossover temperature has been observed. Figure 5.9 shows a decreasing trend in the various crossover temperatures with increase in Ti percentage. Critical region is suppressed in low and high percentage

doping of Ti. The width between various crossover temperatures decreases with titanium percentage. The regime that is close to T_c in the mean field region has 3D type of fluctuations but at temperature T_{LD} there is a crossover from 3D to 2D region of fluctuations. As we move to higher temperature side the superconducting fluctuations follow $1/\varepsilon^3$ behavior, such fluctuation region where the Ginzburg-Landau theory breaks down is known as the Short wavelength fluctuations (SWF).

5.4 Conclusion

The effect of titanium addition on the fluctuation conductivity is studied for the YBCO system. It was observed that Ti doping did not improve the weak-link behavior of the superconducting grains and the critical temperature T_c . But the normal state resistivity is low in comparison to the pure sample in low percentage addition of TiO_2. All the granular parameters like α_n, ρ_{wl}, ρ_p, α_{str} were found to lie in their ideal range. The different regions observed are the critical region at $T < T_c$, the mean field region at T close to T_c and the short wave fluctuations at $T > T_c$. The experimental data fit with theoretical predicted ones. The different crossover temperatures T_G, T_{LD}, $T_{2D\text{-}SW}$ decrease with increase in doping percentage. Critical region is suppressed for low and high percentage addition Ti. XRD graphs show the unchanged orthorhombic structure. Structural changes marked with the sifting and broadening of RAMAN modes with dopant concentration. SEM micrographs reveal the reduced grain size, expecting the net like structures covering the surface of YBCO grains for higher Ti doping as TiO_2 nanowires.

5.5 References

[1] D. K. Avasthi, G. K. Mehta, Swift Heavy Ions for Materials Engineering and Nanostructuring, Springer Series in Materials Science 145 (2011)142.

[2] K. M. Jadhav, R. L. Raibagkar, G. K. Bichile, D. G. Kuberkar, and R. G. Kulkarni, J Superconductivity 8 (1995) 373.

[3] E. Yanmaz, S. Balci, T. Kucukomeroglub, Materials Letters 54 (2002) 191.

[4] Y. Nishi, S. Moriya, S. Tokunaga, J of Materials science letters 7 (1988) 359.

[5] M. Sahoo, D. Behera, J Supercond. Nov. Magn. 27 (2014) 83.

[6] A. Kulpa, A.C.D. Chaklader, N. R. Osborne, G. Roemer, B. Sullivan, D.L. Williams, Solid State Commun.71(1989) 265.

[7] S. Kurihara, "Interacting hole-spin model for oxide superconductors" (1988).

[8] P. Benzi, E. Bottizzo, N.J. Rizzi, Crystal Growth 269 (2004) 625.

[9] R. Liu, C. Thomsen, W. Kress, M. Cardona, B. Gegenheimer, F.W.de Wette, J. Prade, A.D. Kulkarni, U. Schroeder, Phys. Rev. B 37 (1988) 7971.

[10] R.E. Cohen, W.E. Pickett, H. Krakauer, Phys. Rev. Lett. 64 (1990) 2575.

[11] C.O. Rodriguez, A.I. Lichtenstein, I.I. Mazin, O. Jepsen, O.K. Anderson, M. Methfessel, Phys. Rev. B 42 (1990) 2692.

[12] J. Prade, A.D. Kulkarni, F.W. de Wette, U. Schroeder, W. Kress, Phys. Rev. B 39 (1990) 2771.

[13] A. Yamanaka, F. Minami, K. Watanabe, K. Inoue, S. Takenaka and N. lyi, Jpn. J. Appl. Phys. 26 (1987) L1404.

[14] Y. Morioka, A. Tokiwa, M. Kikuchi, Y. Syono, K. Nagase, Solid State Commun. 70 (1989) 1127.

[15] Ming-Sheng Zhang, Z. Yin, G. Hu and Q. Chen, Phys. Rev. B 41 (1990) 2003.

[16] P. D. Beale et al, Solid state Commun. 65 (1988) 1145.

[17] P. V. Huong, J. C. Bruyere, E. Bustarret, and P. Granchampb, Solid State Commun. 72 (1989) 191.

[18] M. Trunec, Ceramics-Silikáty 52(3) (2008) 165.

[19] J. Roa-Rojas, R.M. Costa, P. Pureur, P. Prieto, Phys. Rev. B 61 (2000) 12457.

[20] D.S. Fisher, M.P.A. Fisher, D.A. Huse, Phys. Rev. B 43 (1991) 130.

[21] P.C. Hohenberg, B.I. Halperin, Rev. of Mod. Phys. 49 (1977) 435.

[22] M. Irfan, S. Khan, N. Hassan, N. Ali Khan, J Supercon. & Novel Magnetism 22 (2009) 769.

Chapter 6

Study of Structural Modification and Electrical Transport Property in Low Energy Ion Irradiated YBCO/BSO Composite Thin Film

STUDY OF STRUCTURAL MODIFICATION AND ELECTRICAL TRANSPORT PROPERTY IN LOW ENERGY ION IRRADIATED YBCO/ BSO COMPOSITE THIN FILM

6.1 INTRODUCTION

Cuprate superconductors possess inherent defects, such as lattice mismatch, co-ordination incompatibility and charge state instability [1]. These defects are expected to trap the irradiation induced vacancies and interstitials and make favorable conditions for dissipative structure formation. Therefore, study of the dynamics of defects induced by ion irradiation is expected to reveal the nature and type of these inherent defects already present in the system. Ions having bonds of varying strength, nature and with electronic excitations strongly coupled to the lattice phonons, the response of these systems under irradiation is a complex function of ion energy, mass, fluence and shows significant variation with samples prepared under different conditions [2]. High temperature superconductors (HTSCs) in the form of thin films are of interest for a wide range of device applications i.e. superconducting quantum interference devices, interconnects, and infrared detectors which depend on modification and control of the critical current density (J_c) and width of the superconducting transition. Investigations of ion irradiation effects on superconducting properties are important for developing ion implantation technology to make devices from HTSCs (i.e. ion beam patterning or tailoring of J_c). It yields insight into intrinsic defect properties and irradiation induced modification of properties which are of interest to device applications. These materials have potential applications in electronics and radiation environments [3]. Studies of ion irradiation effects in HTSC such as $YBa_2Cu_3O_{7-\delta}$ (YBCO) have demonstrated unusual changes in both the normal state and superconducting properties [4]. Several studies [5, 6] on ion beam irradiation of thin films of YBCO showed that T_c can be controllably reduced. White et al. [7] have suggested that the T_c onset behavior as a function of fluence indicates a loss of phase coherence as superconducting islands become decoupled. If the accumulation of high fluence irradiation damage initiates a structural change at grain boundaries, then decoupling of superconducting grains at low fluence might also result from the accumulation of irradiation damage at grain boundaries. Ion beams have been used to destroy superconductivity locally in YBCO films in order to pattern SQUIDs [8] and also to reduce J_c in order to make Josephson junction devices [9]. The growth of an amorphous phase at the grain boundaries explains the effect of irradiation on the low temperature electrical properties of the films which are initially to depress the critical temperature of the superconducting

resistive transition. This change coincides with the appearance of amorphous zones in the grain boundaries. Therefore, we can ascribe the effect of low doses of irradiation on superconductivity to the formation at the grain boundaries of a very thin normal layer which inhibits the Josephson coupling of the wave functions of the electron pairs in the neighboring grains [10]. The physical properties of the high T_c oxide superconductors are very sensitive to deviation of oxygen from stoichiometry, which induces a phase change. For film devices of the high T_c superconductors, the control of phases and oxygen content at local regions is important. Ion implantation may lead to a technique of mixing of the component elements on an atomic scale, controlling oxygen contents or adding other elements [11-14]. Ion implantation offers a means of localized, controllable alteration of the superconducting properties of the high T_c superconductors [35]. The progressive loss of superconductivity was attributed to the formation of an amorphous, non-superconducting phase at the grain boundaries leading to the progressive decoupling of the superconductor wave function between the grains **[**10, 35]. Other reports suggest that atomic scale disorder by ion irradiation, especially in the oxygen sub-lattice can result in the reduction of the amplitude of the pair wave function [15]. The ion energy and species are chosen in such a way that they impart a large amount of energy to the atoms at the interface of thin film and the substrate by the process of elastic collisions. The electronic energy deposition beyond a certain threshold can cause the movements of atoms, which can lead to the mixing at the interface.

This chapter presents the experimental findings of the effect of low energy ion irradiation on the structural property and superconductivity of YBCO/1wt.% BSO composite thin films. We have focused on the combined effect of BSO inclusions and defects introduced due to ion irradiation on YBCO thin film prepared by PLD technique. Here, we have studied systematically the influence of 100 keV Ar^{+1}, O^{+1} and Kr^{+1} ion irradiation on structural, microstructural, resistivity and fluctuation conductivity of YBCO+1 wt.% $BaSnO_3$ composite thin film. We choose oxygen ions for irradiation in order to avoid chemical contamination of the YBCO thin film. In order to create more defects which will act as pinning centre, Ar and Kr ions have been selected. Excess conductivity is not analyzed due to damage of samples by irradiation of higher fluence.

6.2 EXPERIMENTAL DETAILS

The preparation technique of YBCO/BSO film with details of growth condition has been discussed in chapter 2 (chapter 2.2.8). The optimized laser deposition time of 10 min yielded

a film of thickness nearly ~150 nm on $LaAlO_3$ (LAO) substrate. Films are prepared at IOP, Bhubaneswar. LAO substrate has been used for lattice compatibility with YBCO [16]. The films were irradiated with 100 keV O^{+1}, Ar^{+1} and Kr^{+1} ions using the pelletron accelerators at IUAC, New Delhi. The ion beam was magnetically scanned over an area of 1×1 cm^2 covering the entire sample. The irradiation fluence (Φ) used were 1×10^{15}, 5×10^{15}, 1×10^{16}, 5×10^{16} ions/cm^2. Phase analysis was done using CuK_α radiation by X-ray powder diffraction (by Rigaku Ultima IV). Raman study was done to confirm the vibrational modes (by Renishaw invia, Laser (514nm & 785nm) with Leica microscopy DM-2500M). Microstructural analysis was done by FESEM (Nova Nano SEM-450). Temperature dependent resistivity ρ(T) was measured using the standard DC four-probe technique with a Nanovoltmeter (Keithley-2182A) and constant current source (Keithley-6221), with the voltage resolution of 10^{-8} V of the Nanovoltmeter, a constant current source of 1 mA flowing through the samples. A closed cycle helium refrigerator (JANIS) and a temperature controller (Lakeshore-332) having a temperature resolution of ± 0.1 K were used for temperature variation. Computer controlled data acquisition system was used with a Lab view program.

6.3. RESULT AND DISCUSSION

6.3.1. X- Ray Diffraction analysis

Figure 6.1 shows the XRD pattern of YBCO/ BSO unirradiated and irradiated films with O, Ar and Kr ions of various fluences. Indexing of the pattern reveals that the films are orthorhombic in structure with space group P_{mmm} (JCPDS Reference code 78-1732). Peaks in the graph shown have preferred orientation (00l) of YBCO. The substrate contribution is marked as LAO. Small peaks of BSO at 2θ = 21.06, 43.06 are identified. The peak intensity of YBCO at (003) and (006) reduces to a greater extent in the O and Ar irradiated samples. The peaks shifting to lower angle value indicates an increase in d spacing caused by the strain of the incoming ions in the film. The increase of the d-spacing implies that the distance between ab-planes was expanded by the knocked on atoms derived from cascade damages which behave as interstitial atoms.

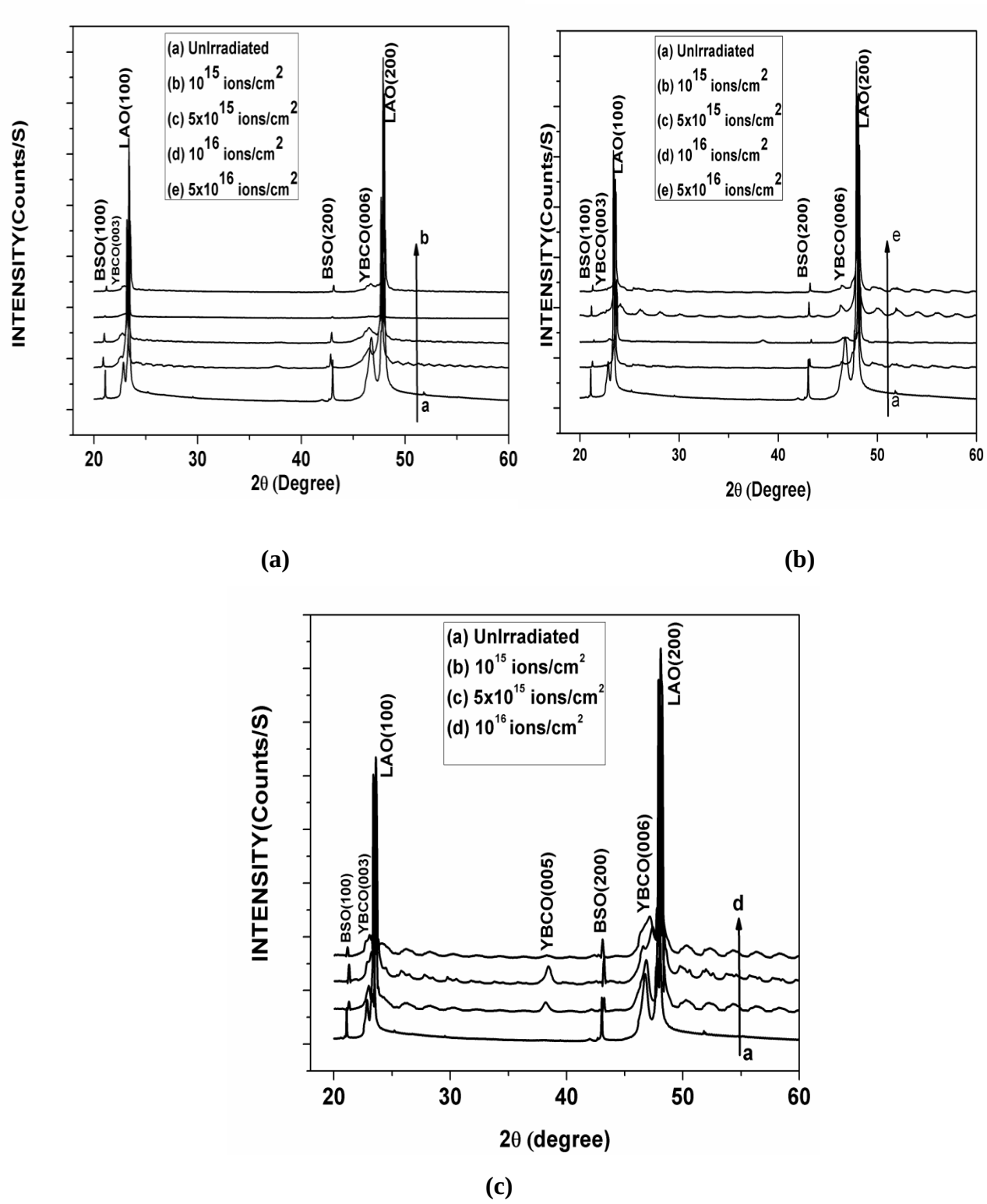

Fig. 6.1 XRD pattern of YBCO / BSO irradiated thin films with 100 keV (a) O^{+1} (b) Ar^{+1} (c) Kr^{+1} ions with varying dose.

The lattice parameters and unit cell volumes of these samples are calculated by using Checkcell Software and presented below.

Table 6.1 Lattice parameters calculated from XRD graphs for O^{+1} irradiation

Sample(YBCO/BSO Thin film)	a(Å)	b(Å)	c (Å)	V ($Å^3$)
Un-irradiated	3.814(1)	3.887(1)	11.679(6)	173.141
10^{15} ions/cm^2	3.824(1)	3.883(1)	11.711(4)	173.891
$5x10^{15}$ ions/cm^2	3.819(1)	3.889(1)	11.714(4)	173.977
10^{16} ions/cm^2	3.818(1)	3.890(2)	11.678(6)	173.441
$5x10^{16}$ ions/cm^2	3.830(1)	3.891(1)	11.681(5)	174.076

From the above data it is clear that there is no significant change in the 'b' lattice parameter for low fluence irradiated samples. But it increases little bit for the higher fluence. The length of 'a' parameter is higher in the irradiated samples as compared to the unirradiated one and highest for the higher dose of 5 x 10^{16} ions /cm^2. Oxygen irradiation affects c-axis more than the other ions. The c-axis length significantly increases in the irradiated samples with lower fluence as compared to the unirradiated sample. The length decreases for higher doses. The volume of the crystallites also gradually increases with increasing fluence. The c-axis length is highest for the sample having lowest oxygen content. This signifies the damaging nature of ions on poor quality films i.e. significant damage is observed for pre-existing defect samples.

Table 6.2 Lattice parameters calculated from XRD graphs for Ar^{+1} irradiation

Sample(YBCO/BSO Thin film)	a (Å)	b(Å)	c (Å)	V ($Å^3$)
Un-irradiated	3.814(1)	3.887(1)	11.679(6)	173.141
10^{15} ions/cm^2	3.822(1)	3.883(1)	11.701(5)	173.652
$5x10^{15}$ ions/cm^2	3.819(1)	3.889(1)	11.693(5)	173.665
10^{16} ions/cm^2	3.816(1)	3.884(1)	11.713(4)	173.602
$5x10^{16}$ ions/cm^2	3.817(1)	3.887(1)	11.683(4)	173.336

From the above data, it is clear that b parameter is not affected by Ar irradiation. The length of 'a' parameter also shows no variation except the lowest fluence. The Ar irradiation affects much on the c-axis length. The c-axis length significantly increases in the irradiated samples with varying fluence as compared to the unirradiated sample. The volume of the crystallites also gradually increases with increasing fluence but decreases slightly for the highest dose.

Table 6.3 Lattice parameters calculated from XRD graphs for Kr^{+1} irradiation

Sample (YBCO/BSO Thin film)	a (Å)	b(Å)	c (Å)	V ($Å^3$)
Un-irradiated	3.814(1)	3.887(1)	11.679(6)	173.141
10^{15}	3.819 (1)	3.890(2)	11.686(6)	173.606
$5x10^{15}$	3.818(1)	3.880(1)	11.704(3)	173.381
10^{16}	3.829(1)	3.880(1)	11.679(5)	173.509
$5x10^{16}$	3.816(1)	3.884(1)	11.695(5)	173.335

From the above tabulated data it is clear that a and b parameter are not affected significantly by krypton ions. The c-axis significantly increases in the irradiated samples with varying fluence as compared to the un-irradiated sample. The volume of the crystallites also gradually increases with increasing fluence but decreases slightly for the highest dose. In the higher fluence peak splitting occurs in the c-axis oriented (003) and (006) peaks.

6.3.2. Raman analysis

Raman spectroscopy is a characterization method that measures the frequencies of the long-wavelength lattice vibrations (phonons). The orthorhombic phase of $YBa_2Cu_3O_{7-\delta}$ has five phonons with Ag symmetry that can be Raman active. The characteristic Raman frequencies of these phonons are 115 cm^{-1} (Ba vibration), 151 cm^{-1} (plane Cu in phase), 339 cm^{-1} (oxygen in CuO_2 planes out of phase), 432 cm^{-1}(oxygen in CuO_2 planes in phase) and 500 cm^{-1} (bridging oxygen out of phase).

In our oxygen irradiated experimental samples (fig 6.2) the 432 cm^{-1} and 339 cm^{-1} mode gets suppressed with oxygen irradiation. A blue frequency shift of the O (4)-Ag Raman mode in un-irradiated sample denotes an increase in the distance between the CuO_2 planes. This increase in distance hinders the charge coupling and weakens electron-phonon coupling yielding poor superconducting properties. As oxygen is depleted from the orthorhombic film the O (4) mode broadens and shifts towards low frequency side. The main change induced by the oxygen depletion is a strong enhancement of the lines at 586 cm^{-1} in the irradiated samples [17]. It has been believed to originate from vibrations of Cu (1) and O (1) atoms in fragment chains [18, 19]. This Raman forbidden phonon mode often seen in various types of YBCO. It is generally accepted that the appearance of this mode is due to activation of the mode resulting from a local change of Cu (1)-O (1) chain environments [20-22].

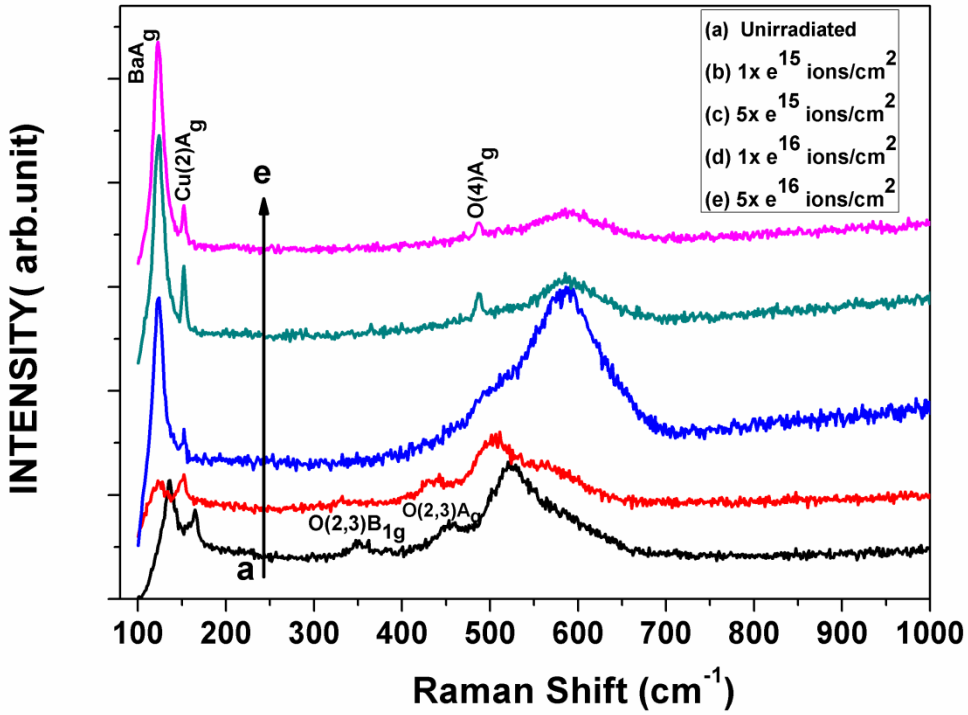

Fig 6.2 Micro-Raman spectra of unirradiated YBCO/BSO composite film and irradiated YBCO/BSO films with 100 keV of O^{+1} ions with varying dose.

As oxygen chains are disturbed due to the ion implantation, disorder of oxygen in the chain-basal plane causes this mode to occur [17, 23-25]. The 115 cm^{-1} and 151 cm^{-1} peaks gets harder with increase in irradiation fluence.

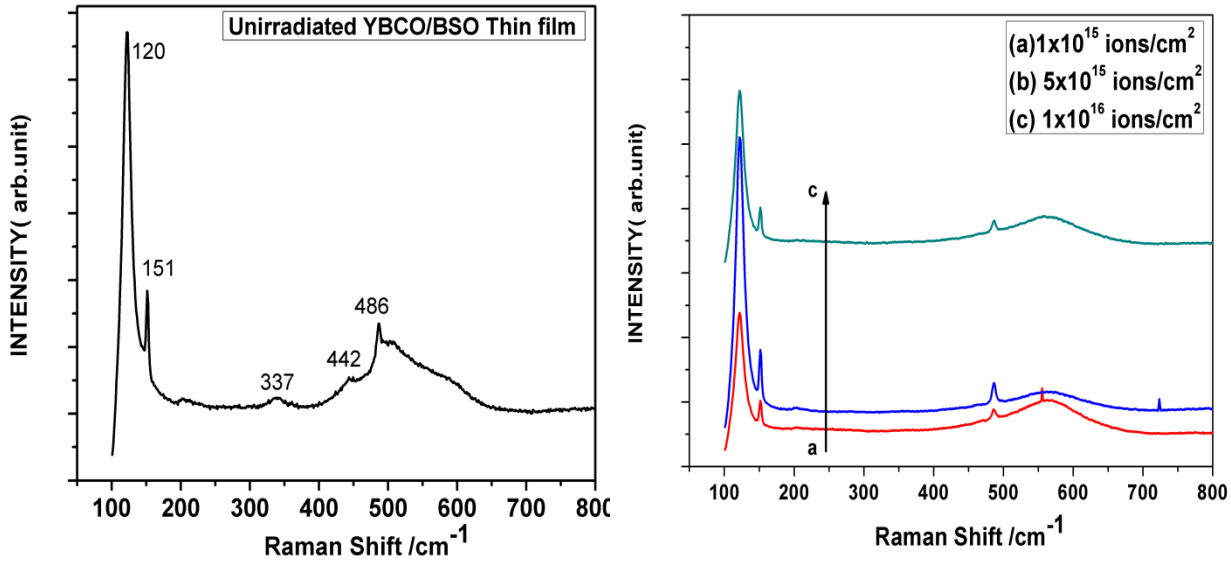

Fig 6.3 Micro-Raman spectra of unirradiated YBCO/BSO composite film and irradiated YBCO/BSO films with 100 keV of Ar^{+1} ion with varying dose.

In our Argon irradiated samples the vibrational mode at 151 cm^{-1} of Cu (2) Ag and Ba vibration at 120 cm^{-1} are not affected by heavy irradiation dose of Ar irradiation. The out-of-

phase vibration of the O(2,3) B_{1g} and in-phase O(2,3) A_g mode for oxygen atoms that are observed in un-irradiated sample has been suppressed due to irradiation as no peak appeared in the CuO_2 planes at 337 cm^{-1} and 442 cm^{-1} in irradiated samples. In the un-irradiated composite sample the O(4) mode appears at 486 cm^{-1}. This is caused due to the oxygen deficiency in the sample. Generally the O (4) phonon mode, is associated with the oxygen content (δ). Huong et al [26] proposed the following relationship between the oxygen content and the peak frequency of the O (4) mode as, $\delta = 13.58\text{-}0.027\nu$ where ν is the peak frequency of the O(4) mode. The value of oxygen content was found to be remaining same in un-irradiated as well as in all the Ar irradiated samples. Hence, it is clear that Ar irradiation does not bring any change in the oxygen stoichiometry of the samples. A strong Raman mode at 555 cm^{-1} and at 723 cm^{-1} arises for irradiated samples. These additional peaks were not observed in the un-irradiated sample. These modes belong to additional defect induced modes caused by oxygen disorder in the O (1) or O (4) sites [27, 28].

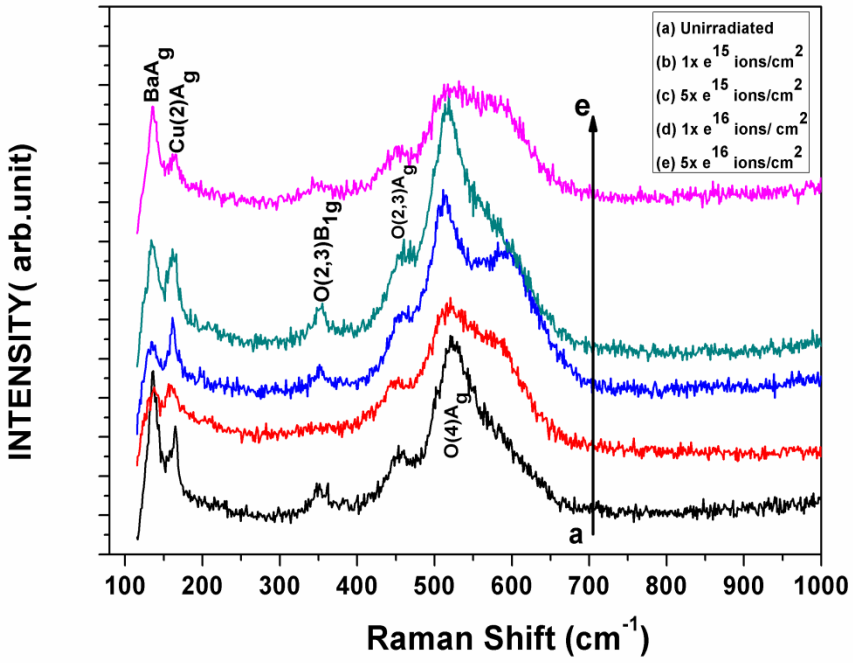

Fig 6.4 Micro-Raman spectra of un-irradiated film and irradiated YBCO/BSO films with 100 keV of Kr^{+1} ions with varying dose.

A strong Raman mode at 600 cm^{-1} arises for the Kr ion irradiated spectrum, to which few research groups associated this mode of vibration to $Ba_2Cu_3O_{5.9}$ phase [29]. Accordingly this defect arises from $BaCuO_2$ due to decomposition of YBCO. Another research group reported that 600 cm^{-1} peak appears in low oxygen content samples replacing O(4) mode in the spectrum [30]. A total of 600 cm^{-1} mode is typically present in oxygen deficit YBCO single crystals and polycrystals [31]. Though the origin of 600 cm^{-1} vibration mode is still elusive,

but it is widely accepted as an influence of defects, oxygen vacancies in the CuO chains that break the crystal inversion symmetry and make some infrared modes Raman active. Some other changes observed with decreasing oxygen stoichiometry are that the BaA_g mode softens in low fluence and hardens in higher fluence irradiated samples. The $Cu(2)A_g$ mode softens in higher dose. Peak broadening occurs in highest dose.

6.3.3. FESEM analysis

The FESEM micrograph of unirradiated YBCO/1 wt. % BSO thin film (Fig. 6.5) shows nano-grains scattered over the substrate. The grain size is measured to be lie within 80 nm range.

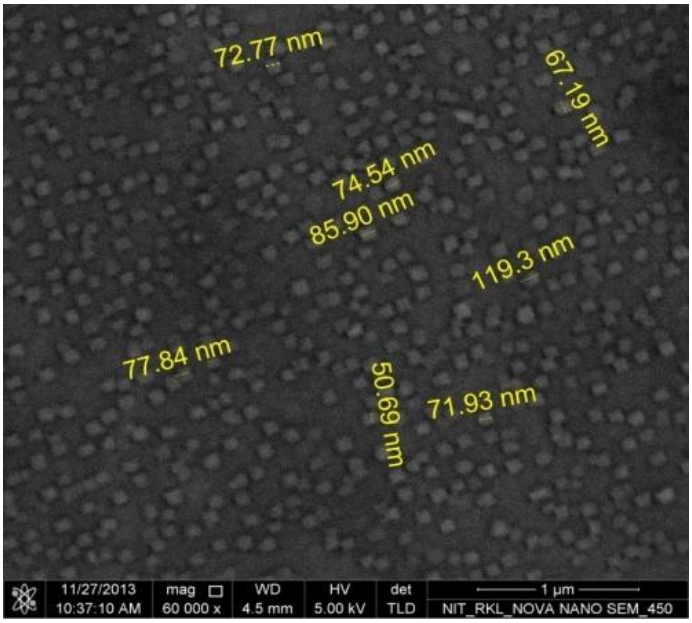

Fig 6.5. FESEM micrographs of $YBa_2Cu_3O_{7-\delta}$ / 1 wt. % BSO unirradiated thin film with 60,000 magnification.

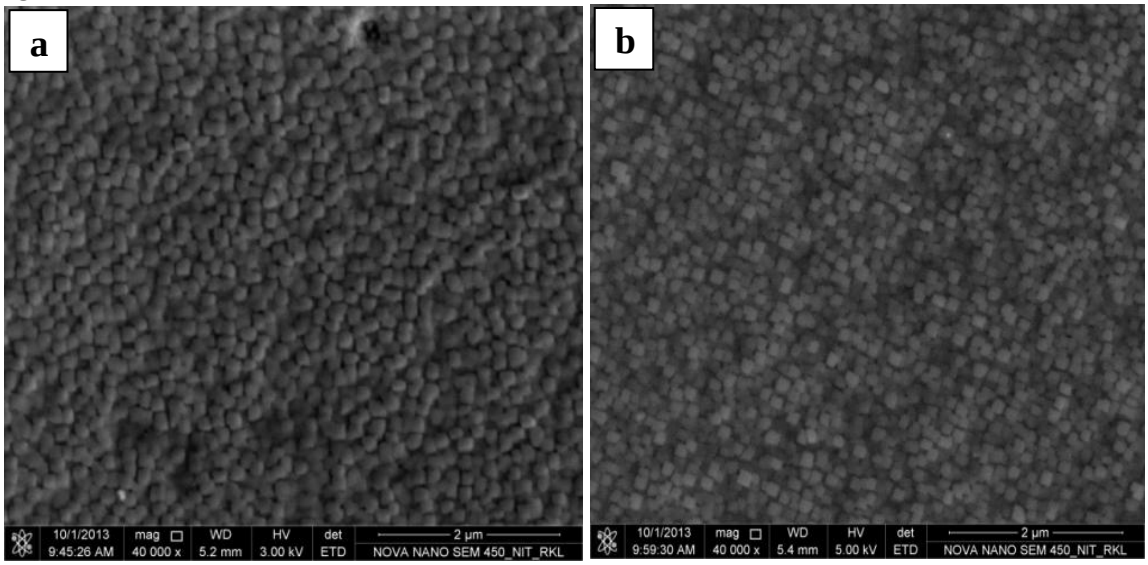

Fig 6.6. FESEM micrographs of (a) O^{+1} irradiated sample with fluence $5x10^{15}$ ions/cm^2 (b) fluence of $5x10^{16}$ ions/cm^2 with 40,000 magnification.

With increasing O^+ irradiation fluence from $5x10^{15}$ to $5x10^{16}$ ion/cm^2 the density is increased. For the lower fluence irradiated samples the grains are rounded in structure. This shape became squared in the higher fluence.

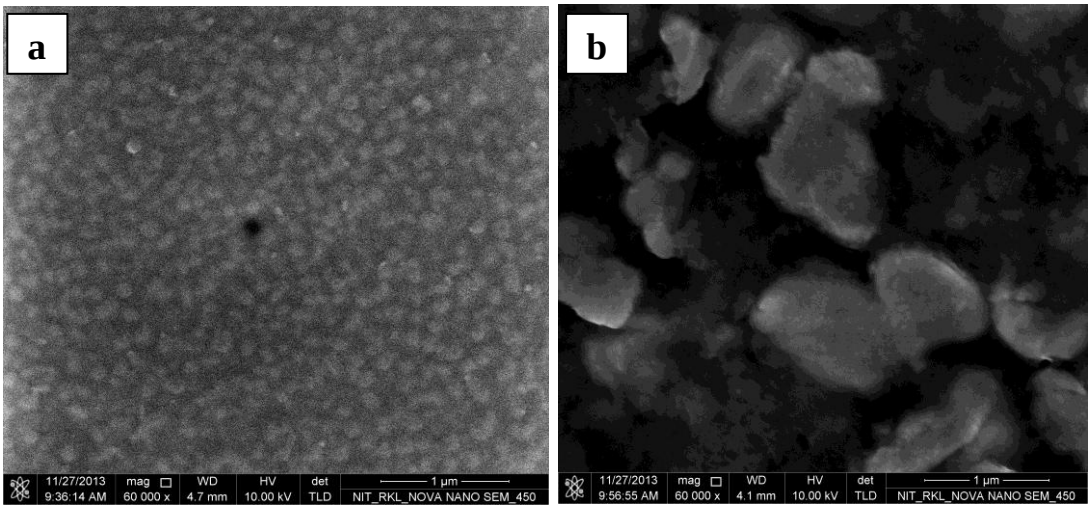

Fig 6.7. FESEM micrographs of Ar^{+1} irradiated samples with fluence (a) $5x10^{15}$ ions/cm^2 (b) $5x10^{16}$ ions/cm^2.

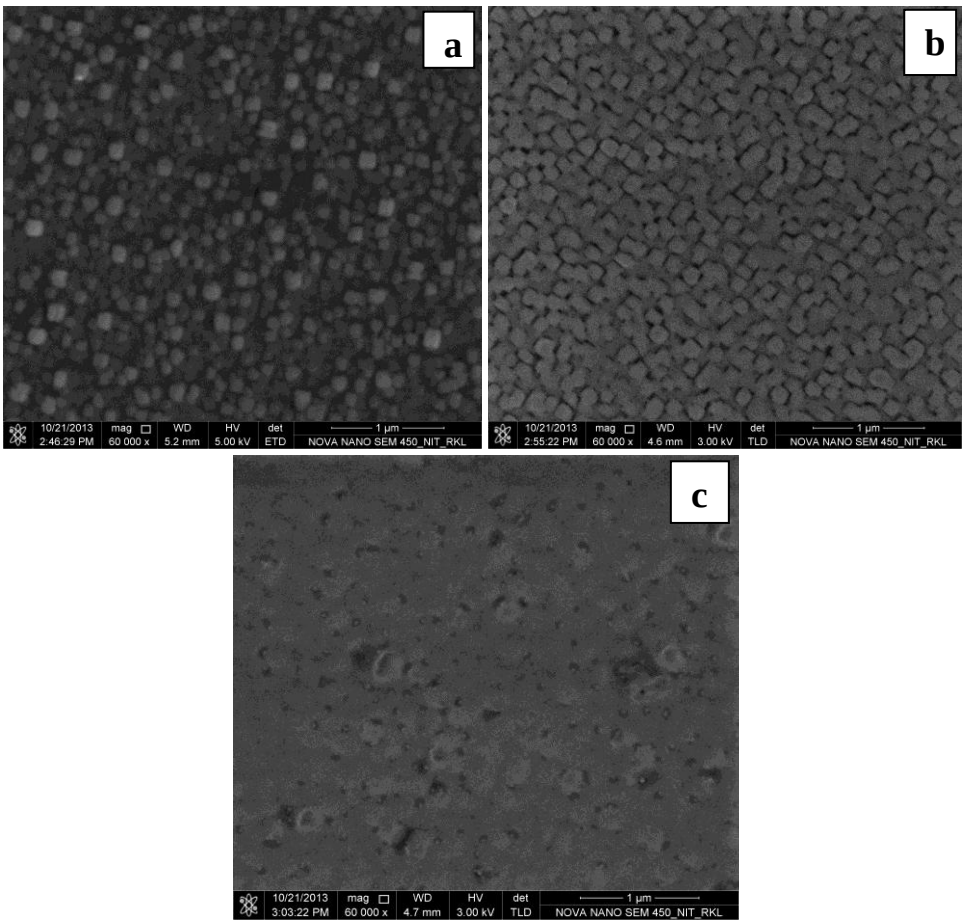

Fig 6.8. FESEM micrographs of Kr^{+1} irradiated samples with fluence (a) $5x10^{15}$ ions/cm^2 (b) 10^{16} ions/cm^2 (c) $5x10^{16}$ ions/cm^2.

In the highest fluence of Ar irradiation (Fig 6.7) the surface of the film gets damaged and BSO particles were found to be agglomerated. For Kr irradiation (Fig 6.8) the particle size increases little bit with increase in irradiation fluence. For highest fluence studied in the present context, complete amorphization occurs in the sample. The rapid crystalline to amorphous transformation takes place when a critical density of point defects is exceeded [32, 33]. In bulk material, this criterion is equivalent to the statement that the transition occurs when the energy deposited into elastic collisions among target atoms reaches a critical density. The value of the critical energy density for $YBa_2Cu_3O_{7-\delta}$ is relatively low. Hence, the atoms in YBCO are easily displaced by irradiation because of the presence of vacancies on the oxygen sublattice, or chemical disorder can increase the free energy of the crystalline phase.

6.3.4. Temperature dependent resistivity measurement

Figure 6.9 shows the temperature dependent resistivity for pristine and YBCO/BSO composite samples. The plot exhibits two different regimes. One is corresponding to the normal state that shows a metallic behavior (above $2T_c$). The normal state resistivity is found to be linear from room temperature to a certain temperature, and in this region it follows Anderson and Zou relation ρ_n (T) =A+ BT [34]. Second is the region characterized by the contribution of Cooper pairs fluctuation to the conductivity below T_c, where ρ(T) is deviating from linearity. This is mainly due to the increasing rate of Cooper pair formation on decreasing the temperature. Therefore, the fluctuation induced conductivity in this region follows the AL model to yield the dimensional exponent appropriately to fluctuation-induced conductivity.

It is observed that the transition temperature in addition of BSO to YBCO decreases from 92 K to 74.79 K. The onset of global superconductivity or zero resistivity temperature (T_{c0}) decreases from 90.17 K for virgin to 70.78 K for composite. The decrease in T_{c0} with BSO content can be explained as arising due to BSO induced modification of grain boundary resulting in progressive decoupling of the superconducting grains. The finite tailing is observed indicating that the superconducting grains get progressively coupled to each other by Josephson tunneling across the grain boundary weak links. For the lower fluence i.e $1x10^{15}$ ions/cm^2 the samples loses their superconducting property for all the three types of ion irradiation and shows semiconductor behavior.

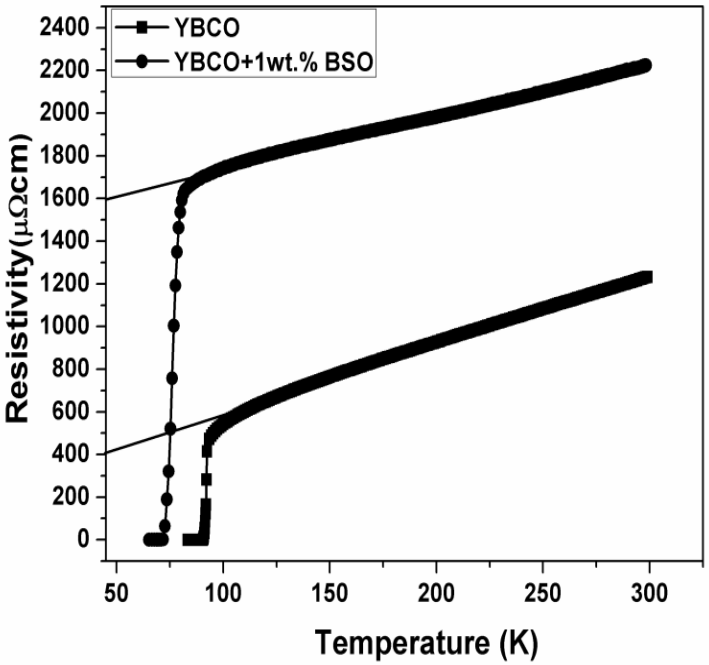

Fig 6.9 Resistivity dependences on the temperature for YBCO+ x $BaSnO_3$ (x = 0.0, 1.0 wt. %) samples.

Gergis et al. was also reported the disappearance of superconductivity in YBCO film for a dose of $6x10^{13}$ O^+ ions/cm^2 at 300 keV [35]. Barbour et al. reported such type of bahavior in $Tl_2Ca_2Ba_2Cu_3O_{10}$ superconductor for a fluence of $2x10^{14}$ O^+ ions/cm^2 at 740 keV [36]. Semiconductor type of behavior was also observed by LI Yijie et al. in YBCO thin film for Ar ion fluence of $7.2x10^{13}$ ions/cm^2 at 180 keV energy [37]. From the SRIM calculation, the penetration depth for O and Ar ions with 100 keV energy for 150 nm film thickness of YBCO was found to be 118, 54 nm respectively. So instead of full penetration, the projectile ions get implanted in the film. Ion implantation easily generates defects along the boundaries between the grains. It decouples the phase coherence of the superconducting wave functions, destroys the links between superconducting regions of the film and results in the degradation of the zero resistance temperature (T_c). Another reason for the reduction of superconductivity is may be due to oxygen sublattice disorder, especially the destruction of the long range order of the Cu-O chains or the generation of oxygen vacancies in the Cu-O square lattice planes. Such atomic scale damage can destroy superconductivity even though the material might still retain a high degree of crystallinity [35]. In YBCO system, oxygen is the lightest atom. Thus in process of ion implantation, its displacement easily takes place from normal crystalline position. It has been reported that the displacement energy (E_d) per ion for plane and chain oxygen was evaluated to be 8.4 and 2.8 eV respectively [38]. Molecular dynamics simulation of Cui et al. [39] has calculated E_d as low as 1.5 eV for oxygen displacements from O(1) to O(5) sites. It is still much higher than the calculated E_d of 0.7 eV corresponding to the

maximum energy (5 keV) of the secondary electrons to account for defect production through an elastic knock-on process. Basing on this observation it is therefore speculated that an inelastic process for low energy electron-lattice interaction, which leads to defect formation in the oxygen sub-lattice and T_c suppression in the system [40]. Hence, the experimental samples lose their superconducting property due to the increase in double defect density both by the process of ion irradiation as well as by the added BSO particles.

6.4 CONCLUSION

Here we report the synergetic effects of BSO addition and 100 keV O^{+1}, Ar^{+1}, Kr^{+1} irradiation on YBCO PLD film. Defects introduced due to ion irradiation decrease the XRD peak intensity. All the three irradiations affects the c-parameter much more as compared to a and b parameter. Broadening and sifting of the bridging oxygen mode in the RAMAN data indicates the depletion of oxygen from the orthorhombic film that weakens electron-phonon coupling which yields poor superconducting properties. The appearance of defect induced Raman modes in the irradiated spectra also indicate the oxygen deficit in the samples. Morphological outlook shows the damaging of the film surface with agglomeration of BSO particles in Ar irradiation and amorphization occurs in the highest fluence for Kr irradiation. The destruction of the long range order of the Cu-O chains or the generation of oxygen vacancies in the Cu-O square lattice planes is the cause of destruction of superconductivity in the samples. As the density of defects increases beyond their critical value, one due to ion implantation and other due to BSO addition, the samples loses their superconductivity property.

6.5 References

[1] Y. Katoh, A. Kohyama, Nucl. Inst. and Meth. B 102 (1995) 12.

[2] H.P. Mohapatra, D. Behera, S. Misra, N.C. Mishra, and K. Patnaik, J. Superconductivity 6 (1993) 359.

[3] D.M. Parkin, Metallurgical Transactions A 21 (1990) 1015.

[4] M. A. Kirk, M. C. Frischherz, J. Z. Liu, L. L. Funk, L. J. Thompson, E.A. Ryan, S.T. Ockers, Physica C 162-164 (1989) 532.

[5] G.J. Clark, A. D. Marwick, R. H. Koch, and R. B. Laibowitz, AppL Phys. Lett. 51 (1987) 139.

[6] G. C. Xiong. H. C. Li, G. Linker, and O. Meyer, Phys. Rev. B 38 (1988) 240.

[7] A. E. White, K. T. Short, D. C. Jacobson, J. M. Poate, R. C. Dynes, P. M. Mankiewich, W. J. Skocpol, R. E. Howard, M. Anzlowar, K. W. Baldwin, A. F. J. Levi, J. R. Kwo, T. Hsieh, and M. Hong, Phys, Rev. B 31 (1988) 3755.

[8] R. H Koch, G. P Umbach, G.l. Clark, P. Chaudari and R.B Laibowitz, Appl. Phys. Lett. 51 (1987) 200.

[9] A. E. White, K. T. Short, R. C. Dynes, A. F. J. Levi, M. Anzolwas, K. W. Baldwin, P. A. l'olakos, T. A. Fulton and L. N. Dunkleberger, Appl. Phys. Lett. 53 (1988) 1010.

[10] G.J. Clark, F.K. Le Goues, A.D. Marwick, R.S. Laibowitz and R. Koch, Applied Physics Letters 51 (1987) 1462.

[11] E.Takayama-Muromachi, Y. Uchida, M. Ishii, T. Tanaka and K. Kato, Jpn. J. Appl. Phys. 26 (1987) L 1156.

[12] J.M. Tarascom, L.H. Green, B.G. Bagley, P. Barboux and G.W. Hull, Proc. International workshop on Novel Mechanism of superconductivity, Berkeley (1987).

[13] H. Sawada, T. Iwazumi, Y. Saito, Y. Abe, H. Ikeda and R. Yoshizaki, Jpn. J Appl. Phys. 26 (1987) L1054.

[14] K. Masuda, A. Osawa, K. Gamo, M. Takai, S. Namba and A. Mizobuchi, Jpn. J. Appl. Phys. 14 (1975) 184.

[15] B. Egner, J. Geerk, H. C Li, G. Linker, O. Meyer and B. Strehlau, Jpn. J. Appl. Phys. 26-3 (1987) 2141.

[16] S. Geller, V.B. Bala, Acta Crystallogr. 9 (1956) 1019.

[17] S. Hong, H. Cheong, G. Park, Physica C 470 (2010) 383.

[18] V. G. Ivanov, M.N. Iliev, C. Thomsen, Phys. Rev. B 52 (1995) 13652.

[19] M. Osada, M. Kakihana, M. Käll, J. Bäckström, L. Börjesson, N.H. Anderson, Physica C 364-365 (2001) 545.

[20] D. R. Wake, F. Slakey, M.V. Klein, J. P. Rice, D. M. Ginsberg, Phys. Rev. Lett. 67 (1991) 3728.

[21] M. N. Iliev, H. U. Habermeier, M. Cardona, V. G. Hadjiev, R. Gajic, Physica C 279 (1997) 63.

[22] C. Thomsen, M. Cardona, B. Gegenheimer, R. Liu, A. Simon, Phys. Rev. B 37 (1988) R9860.

[23] E. Faulques, P. Mahot, M. Spiesser, T. P. Nguyen, G. Garz, C. Gonzalez, P. Molinie, Phys. Rev. B 50 (1994) 1209.

[24] A. Richter, G. Irmer, G. Keßler, G.M. Panzner, K. Herzog, J. Alloys Compd. 187 (1992) 59.

[25] E. Liarokapis, J. Physica C 341-348 (2000) 2185.

[26] P.V. Huong, J.C. Bruyere, E. Bustarret, P. Granchampb, Solid State Commun. 72 (1989) 191.

[27] M. Zhang, Z. Yin, G. Hu, Q. Chen, Phys. Rev. B 41 (1990) 2003.

[28] P. D. Beale, J. F. Scott, M . S. Zhang, Z. Chen, G. Hu, X. Jin, H. Shao, G. Wang, J. Zhao, J Solid State Communications 65 (1988) 1145.

[29] H. Chang, Y.T. Ren, Y.Y. Sun, Y.Q. Wang, Y.Y. Xue, C.W. Chu, J. Physica C 252 (1995) 333.

[30] G. Burns, F. H. Dacol, C. Field, F. Holtzberg, Physica C 181 (1991) 37.

[31] E. Liarokapis, J. Supercond. (Inc. Novel Magn.) 13 (2000) 889.

[32] F. L. Vook and H.J. Stein, Radiation Effects 2 (1969) 23.

[33] M. L. Swanson, J. R. Parsons, and C. W. Hoelke, Radiation Effects 9 (1971) 249, R. W. Cahn, Nature 273 (1978) 491.

[34] W. Anderson, Z. Zou, J. Phys. Rev. Lett. 60 (1988) 132.

[35] I. S. Gergis, P. H. Kobrin, J. F. Denatale and R. M. Housley, SPIE Processing of films for High T_c superconducting electronics 1187 (1989) 275.

[36] J. C. Barbour, J. F. Kwak, D. S. Ginley, P. S. Peercy, Appl. Phys. Lett. 55 (1989) 507.

[37] L. Yijie, R. Congxin, C. Guoliang, L. Zixin, Z. Shichang, J. Chinese Phy. Lett. 8 (1991) 157.

[38] S. K. Tolpygo, J.Y. Lin, M. Gurvitch, S.Y. Hou, J. M. Phillips, J. Phys. Rev. B 53 (1996) 12462.

[39] F. Z. Cui, J. Xie, H.D. Li, J. Phys. Rev B Condensed Matter 46 (1992) 11182.

[40] D. Behera, T. Mohanty, S.K. Dash, T. Banerjee, D. Kanjilal, N.C. Mishra, Radiation Measurements 36 (2003) 125.

Chapter 7

Conclusions and Future work

7. 1 CONCLUSIONS

The work carried out in this thesis is concerned with the structural modifications and analysis of fluctuation conductivity in composites of BSO, Cr_2O_3, BTO-CFO and doping of Ti with YBCO. The modification induced by low energy ion beams in YBCO/BSO PLD thin films is another interesting aspect studied in this thesis. This chapter discusses the major conclusions drawn from the work and ends with a brief note on the future scope of work.

7.2 CONCLUSIONS DRAWN FROM THE WORK

In this thesis superconducting bulk samples have been prepared by solid state reaction route and thin film by pulsed laser deposition technique. All the samples investigated, constitutes of YBCO the well-studied system of HTSC. The defects that make the very existence of superconductivity in cuprates, drive these systems away from equilibrium by way of lattice mismatch and coordination incompatibility at the cation site and composites. Considering the importance of the various types of chemical and structural disorder influencing the superconductivity in the cuprates, a large number of studies concerns with the evolution of superconductivity with defects and disorder introduced artificially into the cuprate structure. The fluctuations due to finite Cooper pair formation induce excess conductivity or paraconductivity in the normal phase close to T_c. Hence, provides scope to study superconducting order parameter fluctuations. The prime objective was to study the structural modifications occurred due to the addition of inhomogeneities and how the oxygen stoichiometry varied with the inclusions and SCOPF analysis with several models and experiments. The current work emphasizes the fluctuation conductivity in the SCOPF region in doped and composite systems of YBCO. Also attempts have been taken to analyze the low energy ion irradiation effects on the structure and superconducting property in PLD thin films of YBCO composite.

7.3 IMPORTANT FINDINGS

- The presence of small stoichiometric and structural inhomogeneities deeply affect the $\rho(T)$ behavior around T_c. Studies on the temperature dependence of resistivity in polycrystalline sintered samples of Ti doped $YBa_2(Cu_{1-x}Ti_x)_3O_{7-y}$ were significantly modified with dopant. Low percentage doping of Ti reduces the normal state resistivity of the pristine sample. Ti does not affect the oxygen stochiometry even if in higher dopant concentration. Critical fluctuation

region is suppressed by doping. The different crossover temperatures T_G, T_{LD}, $T_{2D\text{-}SW}$ decrease with increase in doping percentage. With increase in Ti %, 3D fluctuation region in the mean field is dominated. Grain size reduced too much for higher concentration with the incorporation of Titanium into YBCO matrix which signifies that the strength and hardness of the samples increases.

- The dielectric material BSO was added to YBCO with varying concentration forming composites of (1-x)YBCO+ x BSO (x = 0.0,0.1,0.3,0.5,1.0, 2.5 wt. %). XRD confirmed the formation of orthorhombic phase of YBCO with a space group P_{mmm} and with improved oxygen ordering. Raman studies show the additional defect-induced modes in the higher wt.% BSO added sample due to the disorder in the O(1) or O(4) sites of oxygen. It gives an insight of oxygen suppression occurring on the apical site and lengthening of the c axis due to BSO addition. FTIR spectrum shows the presence of various metal oxygen bonds in the composite sample. Microstructural analysis clearly indicates that the added BSO does not affect the grain size but increases the porosity in the samples. Studies on excess conductivity of the granular samples reveal that the different crossover temperatures T_G, T_{LD}, $T_{2D\text{-}SW}$ decreases in the composites as compared to the pure YBCO. The Lawrence-Doniach temperature (T_{LD}) centered in the low temperature region for higher wt.% addition of BSO. This signifies that fluctuation of Cooper pairs in 3D is dominating in the mean field region.

- Another composite (1-x) YBCO+ xCr_2O_3 (x = 0.0, 2.3, 4.4, 6.1 wt.%) has been investigated for temperature dependence of electrical transport properties prepared through solid state route. Addition of Cr_2O_3 accounts for rise of normal state as well as residual resistivity and weak-link resistivity with shifting of T_c towards lower temperature zone. The splitting of transition temperature marked by double peak in the derivative curve could be correlated with Cr_2O_3 residing in the grain boundary which forms weak links or Josephson junction that results in progressive decoupling of grains. Decrease in the value of T_{c0} and increase in the value of transition width ΔT_c signifies the degradation of inter-grain weak links. The excess conductivity data revealed a dimensional crossover from 2D to 3D fluctuation as the temperature is lowered. No critical region was found for low percentage addition of Cr_2O_3. XRD and RAMAN analysis confirms the unchanged orthorhombic structure with the oxygen

content remains high in all the pure as well as composite samples. RAMAN plots show the defect induced modes due to stretching vibrations of oxygen atoms. SEM micrographs reveal the reduced grain size with the incorporation of magnetic Cr_2O_3 particles in the YBCO matrix.

- In YBCO+x BTO-CFO composites, studies on excess conductivity of granular samples revealed a dimensional crossover from 2D to 3D fluctuation as the temperature is lowered. Addition of BTO-CFO accounts for rise of normal state resistivity and weak-link resistivity with shifting of T_c towards lower temperature zone. XRD and RAMAN analysis confirms the unchanged orthorhombic structure with the oxygen content remains optimal in all the pristine as well as composite samples. RAMAN graphs show the defect induced modes due to vibrations in Cu(1)-O(1) chains. SEM micrographs reveal the unchanged grain size with the incorporation of inhomogeneity in the YBCO matrix.

- Furthermore, a systematic study on PLD deposited YBCO/1wt.% BSO composite thin films (~150 nm) has been carried out in order to investigate the impact of double defects i.e defects introduced with 100 keV O, Ar and Kr ion implantation and also by BSO particles. Defects introduced due to ion irradiation decrease the XRD peak intensity. Broadening and sifting of the bridging oxygen mode indicates the depletion of oxygen from the orthorhombic film that weakens the electron-phonon coupling which yields poor superconducting properties. The appearance of defect induced Raman modes in the irradiated spectra also indicate the oxygen deficit in the samples. Morphological outlook shows the damaging of the film surface with agglomeration of BSO particles in Ar irradiation and amorphization occurs in the highest fluence for Kr irradiation. The suppression of superconductivity in the samples is accounted to be the destruction of long range order of Cu-O chains or the formation of oxygen vacancies in the Cu-O planes.

7.4 FUTURE WORK

The scope for future work of the thesis can be expanded and strengthened further to enhance in depth understating as stated below.

- In depth analysis towards atomic positions and structural arrangements could be achieved by Rietveld refinement of the XRD data at room temperature as well as low temperature at 90 K. The vibrational mode could be well analyzed with low temperature Raman spectroscopy technique in order to get more information about peak softening, broadening, oxygen content and to correlate its structural properties. X-ray photoelectron spectroscopy (XPS) technique could be used for compositional analysis, site occupancy and oxidation state to have complete structural information.

- It will be more informative to characterize all the chosen systems in magnetic field. All the samples may be characterized for critical current density measurement for application point of view. The extent of pinning due to the composite formation may be estimated through the calculation of pinning forces for all the considered composite systems.

- All the chosen systems could be subjected to ion irradiation in order to get more information on the structural modifications and the intra and inter-grain modifications. In situ irradiation experiments could be quite effective. The thin films could be bombarded with a variety of ion species considering the threshold value. Ion implantation on films could be studied as interesting feature to understand the pinning mechanism.